INFORMATION TO USERS

This manuscript has been reproduced from the microfilm master. UMI films the text directly from the original or copy submitted. Thus, some thesis and dissertation copies are in typewriter face, while others may be from any type of computer printer.

The quality of this reproduction is dependent upon the quality of the copy submitted. Broken or indistinct print, colored or poor quality illustrations and photographs, print bleedthrough, substandard margins, and improper alignment can adversely affect reproduction.

In the unlikely event that the author did not send UMI a complete manuscript and there are missing pages, these will be noted. Also, if unauthorized copyright material had to be removed, a note will indicate the deletion.

Oversize materials (e.g., maps, drawings, charts) are reproduced by sectioning the original, beginning at the upper left-hand corner and continuing from left to right in equal sections with small overlaps.

Photographs included in the original manuscript have been reproduced xerographically in this copy. Higher quality 6" x 9" black and white photographic prints are available for any photographs or illustrations appearing in this copy for an additional charge. Contact UMI directly to order.

UMI®

CHARACTERIZING EARTHQUAKE SOURCE COMPLEXITY FOR IMPROVED STRONG MOTION PREDICTION

A DISSERTATION
SUBMITTED TO THE DEPARTMENT OF GEOPHYSICS
AND THE COMMITTEE ON GRADUATE STUDIES
OF STANFORD UNIVERSITY
IN PARTIAL FULFILLMENT OF THE REQUIREMENTS
FOR THE DEGREE OF
DOCTOR OF PHILOSOPHY

Paul Martin Mai
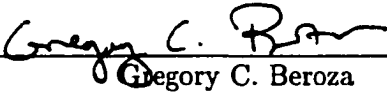January 2002

UMI Number: 3040042

UMI®

ii

I certify that I have read this dissertation and that, in my opinion, it is fully adequate in scope and quality as a dissertation for the degree of Doctor of Philosophy.
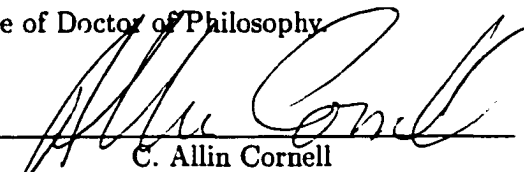
Gregory C. Beroza
(Principal Adviser)

I certify that I have read this dissertation and that, in my opinion, it is fully adequate in scope and quality as a dissertation for the degree of Doctor of Philosophy.
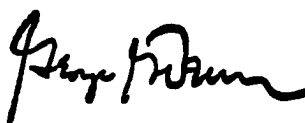
Paul Segall

I certify that I have read this dissertation and that, in my opinion, it is fully adequate in scope and quality as a dissertation for the degree of Doctor of Philosophy.

C. Allin Cornell
(Department of Civil Engineering)

Approved for the University Committee on Graduate Studies:

iii

Abstract

Earthquake hazard mitigation depends on our ability to successfully predict the severity of ground shaking expected in future earthquakes. Two alternative approaches are taken for such strong motion prediction: **(a)** use of empirical equations relating ground motion intensities, observed in past earthquakes, to the earthquake source and the observer location; **(b)** calculation of ground motions for hypothetical future earthquakes based on models for the earthquake source and the Earth's crust. This thesis aims at improving ground motion simulation procedures by developing a description of the earthquake source that comprises spatio-temporal complexity in all relevant source parameters.

Images of the slip distribution on the rupture plane reveal strong spatial variability of earthquake slip. Using such finite-source rupture models, I first investigate the scaling properties of source parameters fault length, fault width, mean slip, and seismic moment. The results indicate non-constant stress-drop scaling for large strike-slip earthquakes, and the inadequacy of currently used magnitude–area relationships. I then deploy a spatial random-field model to characterize the spatial variability of earthquake slip. From inversion of two-dimensional wave-number spectra of 44 rupture models, I infer that the *von Karman* auto-correlation function best describes the spectral decay of earthquake slip, with correlation lengths increasing with increasing seismic moment. Such an earthquake-slip characterization allows to generate versatile scenario earthquakes for strong motion simulation.

Current strong motion simulation procedures are generally limited to the low-frequency range ($f \leq 1\,\mathrm{Hz}$), yet, engineering applications may require ground motion predictions to higher frequencies. To overcome this limitation, I develop a hybrid method to calculate broadband, near-source ground motions. Using a *kinematic* source description (simulated slip, assumed rise time and rupture velocity, simple slip-velocity function), I apply this technique to rupture realizations of two *past* earthquakes. The velocity seismograms exhibit the expected large forward-directivity pulses, but at shorter periods the simulated response

iv

spectra indicate difficiencies compared to the observations.

Comparison of ground motion simulations for *kinematic* and *full-dynamic* earthquake source models demonstrates the necessity to include variability in rise time and rupture velocity into the source characterization. Calibrated against full-dynamic rupture models, I develop a *pseudo-dynamic* earthquake source model, based on a stochastic slip distribution, its corresponding stress drop, and simple models of rupture dynamics. The *pseudo-dynamic* rupture characterization captures the properties of ground motion intensity as seen in the full-dynamic simulations as well as in empirical relationships. Simulations for generic $M_w = 7.0$ strike-slip earthquakes as well as scenario earthquakes on the Hayward-Rodgers Creek fault system ($6.38 \leq M_w \leq 7.61$) demonstrate the effectiveness of the *pseudo-dynamic* earthquake source model to characterize earthquake source complexity for improved strong motion prediction. Realistic, *dynamically-consistent* ground motion simulations may potentially augment the sparse data base of near-source ground motion recordings of large earthquakes, and thus help to understand better the variability of near-source strong ground motion, particularly for large earthquakes.

v

Acknowledgements

I am deeply grateful to my advisor Greg Beroza. Greg not only has happily taken on the role as my advisor when I decided to change my research area after my initial year at Stanford, but ever since, he was an inspiring example of a student advisor: patiently answering a never ending stream of questions, encouraging when progress was slow, shaving off the worries of funding by successfully writing proposals, being approachable in every aspect of life. It has been an extraordinary experience to work with Greg, indeed, and the occasion where he showed up in the lab during *AGU*-week at 1AM in the morning to finish his presentation only underscores *how* close he is to his students ...

I want to thank my committee members Gary Mavko, Paul Segall and Mark Zoback for their encouraging interest in my work, their numerous comments and critiques they expressed in our regular meetings. Allin Cornell has been something like a "co-advisor" for me, and I am indebted to him for his stimulating enthusiasm in my research, for inspiring in me the interest in the engineering perspective of strong motion seismology, and for generating the notion in me that there is some usefullness to statistics!

Thanks to Joe Andrews, Jack Boatwright, Bill Ellsworth and Paul Spudich at the U.S. Geological Survey in Menlo Park whose interest in my research has been a great source of motiviation. Joe kindly reviewed an early version of the manuscript of the paper reproduced in Chapter 3, Jack helped to cook up the project on dynamic rupture modeling (Chapter 5), and Bill's comments helped me to understand better the source-scaling issues. I am grateful to Paul for his insightful comments on my thesis, and for putting together the DWFE- and Isochrone codes in such an understandable and useable fashion that even I was able to use them.

I am indebted to Patti Guatteri for collaboration on the work presented in Chapter 5.

Patti actually did all the dynamic rupture modeling, and her enthusiasm for the project was irresistible. I greatly benefitted from her insight and expertise in rupture physics, and her review of an early version of the source-scaling manuscript – thanks a bunch for all your help, Patti! Nico Luco has helped me greatly to see and understand the engineering perspective of strong motion seismology, and I am grateful for his collaboration on the simulations for scenario earthquakes on the Hayward-Rodgers Creek Fault System.

I am very thankful to the constant love and support of my mom who always believed in me being able to finish this Ph.D. I am thankful to my parents-in-law for their support and encouragement. Thanks to the seismo-gang: David Schaff, who has become a very special friend, Eva and Xyoli for their companionship, Jeff McGuire and Satoshi Ide for encouraging discussions. And of course, there are those friends in and (in the meantime) out of Stanford who made the time at Stanford truly a life-time experience: Ali, Adela & Luis, Balz & Lourdes, Thomas & Myraida, Anna & Maurizio, Doron & Michal, Roger & Steffi, Tanja & Radu, Jacky & Fred, and many more in and around the department which I can't possibly list here. A special thanks to the staff at the department, Agnes, Laurie and Linda, for their help through the burocratic maze.

Finally, I want to thank my wonderful wife, Tanja, who put up with me during so many weekends and evening hours. Without her continuous love, support, and encouragement I wouldn't have been able to finsh this task. Special thanks and hugs to my kids, Max and Laila, whose love and joy is a continuous blessing, and whose demands on me put things into perspective, showing me what matters most.

Lastly, I thank my Lord and Savior, Jesus Christ, for giving me strength and enabling me to do this work, for blessing me with these people in my life, for giving me directions and guiding my steps.

Contents

ix

List of Tables

xi

List of Figures

Chapter 1

Introduction

Earthquakes release the strain energy accumulated through plate motions in sudden movements of the Earth's crust. The resulting ground motions may cause major damage to buildings, infrastructures, lifelines, and society in general. Recent large earthquakes (Izmit, Turkey, 1999; Chi-Chi, Taiwan, 1999; Kobe, Japan, 1995; Northridge, California, 1994) demonstrated painfully how vulnerable we are to the destructive energy of such earthquakes. Obviously, it would be desirable to know ahead of time when and where the next big earthquake will strike, and what its magnitude is going to be.

Unfortunately, we are not able to forecast the size and location of future earthquakes, and perhaps we will never be. Even if we could predict earthquakes, seismologists and earthquake engineers alike still need to develop methods to predict the severity of shaking that we can expect for future earthquakes. Those strong ground motion predictions can then be used to define building codes for earthquake safety, to design structures to withstand a given ground motion intensity level, and to alert the public for earthquake preparedness. Estimates of expected ground motion intensities are also a key ingredient to Probabilistic Seismic Hazard Analysis (PSHA) [*Cornell*, 1968] which calculates the probability of exceedance of a certain ground motion intensity level at a given site in a given period of time.

Two alternative approaches are used for strong motion prediction. We can use measurements of ground motions of past earthquakes to develop equations that relate some ground motion intensity measure (for instance peak-ground acceleration, PGA, peak-ground velocity, PGV, or spectral acceleration, S_A for given period T and damping δ) to properties of the earthquake source (magnitude, faulting style) and the observer location (distance, site conditions). These parametric relations are referred to as "attenuation relationships", and various models have been developed over the years [*Boore and Joyner*, 1981; *Boore and*

1

Joyner, 1982; *Boore and Joyner*, 1989; *Youngs et al.*, 1995; *Boore et al.*, 1997; *Abrahamson and Silva*, 1997; *Somerville et al.*, 1997; *Spudich et al.*, 1997; *Spudich et al.*, 1999] which are updated and modified with each large earthquake that provides additional data. The reliability of these attenuation relationships depends strongly on the available data, and this is the exact difficulty seismologists are dealing with. In particular, the scarcity of strong motion recordings in close proximity to large earthquakes renders the extrapolation of such attenuation laws from far distances, where abundant recordings exists, to close distances, where there are only few data, unreliable.

Alternatively, we can use our admittedly limited knowledge of earthquake source mechanics and crustal structure to compute ground motions for hypothetical future earthquakes [*Saikia*, 1993; *Heaton et al*, 1995; *Olsen et al.*, 1995; *Olsen and Archuleta* 1996; *Saikia and Somerville*, 1997; *Graves* 1998; *Inoue and Miyatake*, 1998; *Pitarka et al.*, 2000; *Aargard et al.*, 2001]. Obviously, there are two major ingredients to acurate strong motion prediction: an adequate Earth model, and an appropriate characterization of the earthquake source. High-resolution images of the Earth, i.e. the velocity/density field, and the three-dimensional Earth structure, have become available in recent years. To take advantage of these detailed crustal models, three-dimensional wave-propagation codes are necessary, e.g. finite-difference [*Olsen et al.*, 1995; *Graves* 1998; *Pitarka et al.*, 1998] or finite-element methods [*Oglesby et al.*, 1998; *Aargard et al.*, 2001]. Such three-dimensional simulation codes not only allow to include complex Earth structure and fault geometry into ground motion simulations, but potentially could also incorporate small-scale structural heterogeneity, leading to scattering and focusing/defocusing effects of the seismic wave-field. The flexibility of these methods comes at the cost of computation time and chip memory, and their applicability is therefore limited to either small spatial domains or low-frequency wavefields. The computational costs associated with these codes also prevents their use from computing ground motions for many realizations of scenario earthquakes (needed to get some meaningful statistics on ground motion estimators), because the governing equations of motions have to be solved for each single rupture realization.

Alternative techniques to compute near-source strong motion use, for instances, empirical Green's functions which are assumed to contain all information about Earth structure between the source and the receiver [*Irikura and Kamae*, 1994; *Kamae and Irikura*, 1998; *Pitarka et al.*, 2000]. In this approach, a considerably smaller earthquake, collocated with the mainshock and having the same faulting mechanism, represents the Green's function for

each point on the rupture plane. Other techniques compute theoretical Green's functions, in most cases for a layered, one-dimensional Earth model, and therefore excluding basin effects, layer-topography or smaller-scale heterogeneity. In the course of this thesis, I deploy two of these methods which are, in their domain of applicability, very efficient. The isochrone method uses ray-theory to calculate high-frequency seismograms which are inaccurate at low frequencies, in particular in the near-source region [*Spudich and Frazer*, 1984]. The high-frequency approximation, however, allows to efficiently calculate synthetic ground motions, even for many rupture models. In contrast, the discrete-wavenumber/finite-element method (DWFE) [*Olson et al.*, 1984] includes all near-source effects by computing the full wavefield. While this method is rather inefficient in calculating theoretical Green's functions (in particular for higher frequencies and/or when low seismic velocities are present), it has the advantage that Green's functions and tractions on the fault plane are calculated only once for a given source-receiver geometry. The resulting tractions can then be used to generate strong motion synthetics for arbitrary many rupture realizations. Obtaining time series from the pre-computed tractions and rupture models is very efficient, and hence the DWFE-method is useful for simulating many scenario earthquakes for *statistical inferences* of ground motions.

Given we had a reliable small-scale Earth model, and given the computational resources, we therefore would be able to compute exact near-source ground motion up to frequencies of engineering interest – provided we had a realistic characterization of the earthquake source. Realistic strong motion simulations require an appropriate earthquake source description that captures the variability of source parameters as observed in past earthquakes. While there has been considerable progress in obtaining detailed crustal models and in developing fast and efficient algorithms to compute the seimic wave-field, seismologists are still trying to decipher the mechanics and dynamics of earthquake rupture. Each study of the recent large earthquakes reveals new, unexpected details of earthquakes behavior, and only recently have researcher begun to perform larger-scale dynamic rupture modeling with realistic Earth complexity to better understand the physics of earthquake rupture [*Mikumo and Miyatake*, 1993; *Mikumo and Miyatake*, 1995; *Beroza and Mikumo*, 1996; *Olsen et al.*, 1997; *Oglesby et al.*, 1998; *Day et al.*, 1998; *Oglesby et al.*, 2000a; *Oglesby et al.*, 2000b].

Moreover, though seismologists have gained some understanding of earthquake rupture, the source models generally used in strong motion simulations are greatly simplified. *Dynamic* rupture models show variablity in all source parameters: slip, rise time, rupture

velocity, slip-time function; *kinematic* source characterizations, on the other hand, specify some variable slip distribution, but all other source parameters are assumed *a priori*, and hence the resulting rupture models may not be physically realistic. Recent studies have begun to incorporate randomly-varying rupture velocity, based on the wavenumber spectrum of the slip distribution [*Hisada*, 2000; *Hisada*, 2001], or wavenumber-dependent variable rise time [*Herrero and Bernard*, 1994], into source models for strong motion prediction. These source characteriztions, however, are still inherently *kinematic*, and they rely on an assumption of the spectral properties of the two-dimensional slip function [*Andrews*, 1980b].

This thesis aims at improving strong motion predictions by developing a realistic characterization of earthquake source complexity. In order to achieve this goal, I use information about past earthquakes to obtain an earthquake source characterization that comprises the observed spatio-temporal variability of earthquake source parameters. The "data" on past earthquakes are images of the slip distribution on the rupture plane, as found in finite-source inversions [*Heaton*, 1982; *Hartzell and Heaton*, 1986; *Beroza*, 1991; *Wald and Heaton*, 1994; *Sekiguchi et al.*, 1996], revealing strong spatial variability of earthquake slip, and occasionally also in rupture velocity [*Beroza and Spudich*, 1988; *Archuleta*, 1984; *Bouchon et al.* 2000] or rise time [*Cotton and Campillo*, 1995; *Bouchon et al.* 2000]. For various "stages" of my earthquake source models I calculate near-source ground motions which I compare against recorded ground motions. This approach not only allows for model validation, but also an assessment of how much variability in the source parameters is needed to reproduce ground motion observations.

The approach taken in this thesis is such that I first establish how to estimate the overall source dimensions for future earthquakes (Chapter 2). Then I develop a model to characterize (and the predict) the spatial variability of earthquake slip (Chapter 3), followed by an application to strong motion prediction based on a *kinematic* source description and hybrid broadband seismograms (Chapter 4). In Chapter 5, I develop a *pseudo-dynamic* earthquake source model, calibrated against full-dynamic rupture models, that comprises spatial variability in rupture velocity, rise time and slip-velocity function. Finally, in Chapter 6, I deploy this earthquake source characterization for strong motion prediction at selected locations in the San Francisco Bay Area (California) for scenario earthquakes on the Hayward-Rodgers Creek fault system.

Chapter 2 addresses the question of how various source parameters are related to one another. In particular, I investigate the scaling of mean slip, fault length and fault width with seismic moment. The resulting scaling relations are not only important to better understand the physics governing earthquake rupture; they are also used in earthquake engineering to estimate, for instance, the magnitude of future earthquakes given the length of a fault segment. The scaling relations developed in Chapter 2 are based on images of earthquake slip obtained through inversion of seismic and/or geodetic measurements. These finite-source inversions reveal that slip on the fault plane is spatially heterogeneous at all scales. Determining the source parameters based on such slip models provide, therefore, alternative, and more accurate, measurements of source dimensions than estimating rupture length and width from surface observations and aftershock locations. The resulting scaling relations differ significantly from widely used relationships [*Wells and Coppersmith*, 1994], and suggest that strike-slip earthquakes may be governed by non-constant stress drop scaling. Moreover, we advocate a M–$\log(A)$ relationship for strike-slip earthquakes (Appendix A) that predicts significantly larger magnitude for given area than previous relations [*Wells and Coppersmith*, 1994; *Somerville et al.*, 1999], but agrees with the recent study by the *WorkingGroup99* [2000]. For faults of a given slip rate, the same relation also predicts on average more slip, and hence smaller recurrence intervals.

While Chapter 2 focuses on the overall source parameters, Chapter 3 investigates the spatial heterogeneity of earthquake slip. I adopt a spatial random-field model to characterize the spatial complexity of these slip distributions. Such a random-field model is either described by an auto-correlation function in space, or by its corresponding power spectral density in the Fourier domain. In order to probe the characteristics of spatially variable earthquake slip, I develop an inversion algorithm that operates on the two-dimensional power spectral densities of finite-source slip models. Assuming a fractal model for earthquake slip, I find that the fractal dimension is estimated as $D = 2.29(\pm0.23)$, which is inconsistent with theoretical considerations for a constant stress-drop model [*Andrews*, 1980b]. The correlation lengths for a *von Karman* auto-correlation function, on the other hand, appear to be related to earthquake size. Based on these findings, slip distributions for strong ground motion simulations can be generated using source-scaling relations to constrain the rupture dimensions, and magnitude-dependent correlation lengths to calculate spatially variable slip distributions.

Generally, strong motion calculations are limited to the low-frequencies ($f \leq 1\,\mathrm{Hz}$);

higher frequencies are either neglected, or stochastically simulated [*Saikia and Somerville,* 1997]. In Chapter 4 I present a hybrid method for calculating near-source, broadband seismograms, in which full-wavefield, low-frequency seismograms and ray-theory, high-frequency seismograms are reconciled in the frequency domain to form a composite broadband signal. I apply this technique to calculate ground motions for two scenario earthquakes (chosen to be similar to past earthquakes to allow model validation) whose source characterization are based on the scaling relations developed in Chapter 2 and the random-field model of earthquake slip in Chapter 3. For these ground motion simulations I assume that the rupture propagates at constant rupture velocity, and that the functional form and the time-dependence of slip after rupture is the same everywhere on the fault. The resulting *kinematic* earthquake source models, however, may not be physically plausible, and hence the step towards *dynamic* rupture models in strong motion simulation seems inevitable. Such dynamic rupture models may also be superior in predicting the ground motion intensity than simple kinematic source models [*Guatteri,* 2000b].

Dynamic rupture modeling is a *time-consuming* and computationally-expensive tasks, yet, it provides a natural and self-consistent earthquake source model, in which slip, rupture velocity, rise time and slip-velocity function may vary over the fault plane. It therefore would be desirable to develop rupture models that contain a simple approximation to the spatio-temporal variability of dynamic rupture models. In Chapter 5 I discuss an approach to define such *pseudo-dynamic* earthquake source models, calibrated against full-dynamic rupture models which are based on stochastic slip realizations for hypothetical M_w = 7.0 strike-slip earthquakes [*Guatteri et al.,* 2000c]. In these *pseudo-dynamic* source models, rupture velocity is based on simple dynamic considerations following *Andrews* [1976], the rise time is found based on a healing front propagating over the rupture plane at shear-wave velocity, and the slip-velocity function is assumed to follow the quasi-dynamic solution to a circular expanding shear crack [*Archuleta and Hartzell,* 1981]. The ground motions computed for these *pseudo-dynamic* source models, as well as the response-spectral values, are comparable to the full-dynamic simulation, yet, they come at much cheaper cost, and hence are likely to be useful for improved strong motion prediction. The spectral response for both the full-dynamic and the *pseudo-dynamic* simulations correspond well to empirical ground motion predictions [*Abrahamson and Silva,* 1997], though differences remain. In particular, at very short distances to the fault, I find spectral accelerations that are on average *lower* than empirically predicted, but have larger dispersion. Both the full-dynamic as well as the

pseudo-dynamic simulations show this near-source behavior, and future research will have to (dis-)prove this observation.

Finally, in Chapter 6, I apply the concepts developed in Chapters 3–5 to predict strong ground motion at selected locations in the San Francisco Bay Area (California). Computing *pseudo-dynamic* source models based on simulated slip distributions, I generate scenario earthquakes on the Hayward-Rodgers Creek fault system (California). For that purpose, I adopt the source dimensions and magnitudes given in the *WorkingGroup99*-report [2000]; randomizing over the median magnitude, I generate 30 rupture realizations for each of the six fault segments and their possible combinations. This set of 180 simulated earthquakes spans the magnitude range $6.38 \leq M \leq 7.61$, or two orders of magnitude in terms of seismic moment. Comparing the strong ground motions for the *pseudo-dynamic* simulations with the corresponding *kinematic* models indicates larger variability and larger amplitudes of ground motion intensity for the *pseudo-dynamic* scenarios. Strong directivity effects are present, and structures and buildings at the selected locations experience severe shaking. Occasionally the simulated ground amotion intensities (S_A, PGA, PGV) are far too large, exceeding the empirical predictions by up to a factor 5, indicating that further research will have to refine the *pseudo-dynamic* source description.

The challenges of performance-based engineering will increasingly require to model structures as dynamic, non-linear multi-degree-of-freedom systems. This approach requires the entire time series of strong ground motion as input, and the strong motion simulations of Chapter 5 and Chapter 6 may be useful to augment the sparse data base of strong motion recordings in the near-field of large earthquakes. In fact, *Luco et al.* [2001b] have used the *kinematic* simulations for the scenario earthquakes on the Hayward-Rodgers Creek fault system for Probabilistic Seismic Demand Analysis (PSDA) at one near-fault site, showing that the simulated ground motions are generally capable of reproducing the behavior of ground motion intensity measures inferred from observed recordings.

Chapter 2

Source Scaling Properties from Finite-Fault Rupture Models

Appendix A.2 discusses the updated scaling relations after addition of 13, more recent slip models, and compares the magnitude-area relations for recently published scaling laws.

2.1 Abstract

Finite-source images of earthquake rupture show that fault slip is spatially variable at all resolvable scales. In this study we develop scaling laws that account for this variability by measuring effective fault dimensions derived from the autocorrelation of the slip function for 31 published slip models of 18 earthquakes, 8 strike-slip events and 10 dip-slip (reverse, normal, or oblique) events. We find that dip-slip events show self-similar scaling, but that scale invariance appears to break down for large strike-slip events for which slip increases with increasing fault length despite the saturation of rupture width. Combining our data with measurements from other studies, we find evidence for a non-linear relationship between average displacement and fault length in which displacement increases with fault length at a decreasing rate for large strike-slip events. This observation is inconsistent with pure width or length scaling for simple constant stress-drop models, but suggests that the finite seismogenic width of the fault zone exerts a strong influence on the displacement for very large strike slip earthquakes.

8

2.2 Introduction

Understanding the nature of large earthquake scaling may ultimately help to reveal the underlying mechanics of the rupture process. It is also important in efforts to anticipate strong ground motion in large earthquakes. Many studies of earthquakes have found that earthquakes are scale invariant such that stress drop is independent of earthquake size [*Aki*, 1972; *Kanamori and Anderson*, 1975]. This is a remarkable observation and leads directly to scaling laws between source dimensions and average slip. Departures from this scaling include reports of larger stress drop for intraplate events [*Kanamori and Anderson*, 1975] or events with long recurrence intervals [*Kanamori and Allen.*, 1986]. There is also the question of how the source properties of very large earthquakes scale. The data presented in this paper will help to examine scale invariance and source geometry for interplate earthquakes in the transitional regime from small to large earthquakes.

For very large earthquakes, the apparent scale-invariance of earthquake stress drop has to be reconciled somehow with the finite width of the seismogenic zone. The seismogenic zone is limited in extent by the Earth's free surface and by the brittle-ductile transition at depth [*Scholz*, 1982]. Once large earthquakes reach a certain size, their continued growth is constrained in size in one dimension. Because strike-slip earthquakes occur primarily on vertical faults, and the extent of the seismogenic zone is limited in depth, this effect should be evident at lower values of seismic moment than for dip-slip events. Only very large reverse faulting earthquakes are likely to be affected by this constraint since reverse faults often traverse the seismogenic zone at shallow angles.

In this study, we investigate earthquake scaling by examining the slip distribution of earthquakes imaged by near-source strong motion, teleseismic, and geodetic data. We characterize these events by fault length, L, fault width, W, and average slip, D, and use these measurements together with the seismic moment, M_o, as the basis for earthquake scaling relations. The primary disadvantage of our approach is that the number of earthquakes for which detailed slip maps exist is relatively small. This disadvantage is offset by the fact that the properties of interest (rupture length, rupture width, and mean slip) are best resolved in finite-source slip models. Hence, the data presented in this paper provide alternative, and presumably more accurate, estimates of fault parameters than those that form the basis for earlier studies. Over the range of seismic moment for which finite-fault slip models are available (2.2×10^{17} N-m $\leq M_o \leq 1.2 \times 10^{21}$ N-m), our results suggest that dip-slip events

follow self-similar scaling. For strike-slip events in this range of seismic moment, however, seismic moment scales as the cube of fault length, but fault width saturates. Thus, average slip increases with fault length and self-similar scaling does not hold.

2.3 Earthquake Scaling

Earthquakes are often thought to follow self-similar scaling in which the source dimensions are scale-invariant, i.e. events of different sizes cannot be distinguished except by a scale factor [*Scholz*, 1990]. Using the relation between seismic moment and the source dimensions,

$$M_o = \mu L W D \tag{2.1}$$

where μ is the rigidity of crustal rock, self-similar scaling predicts $M_o \propto L^{1/3}$, $M_o \propto W^{1/3}$, and $M_o \propto D^{1/3}$. For a uniform stress drop shear crack, the static stress drop, $\Delta\sigma$, is defined as [*Aki*, 1972]

$$\Delta\sigma = C\mu\frac{D}{L_c} \tag{2.2}$$

where D is the mean slip, L_c is a characteristic length, the smallest dimension of the rupture within the fault plane, and C is a constant of order unity, that depends on rupture geometry. In a real earthquake, for which slip is spatially variable at all resolvable scales, the stress drop will vary strongly with position and will be controlled by length scales much shorter than the length or the width of the entire rupture. Nevertheless, we use the parametrization of an average stress drop (determined for the overall rupture dimensions and average slip by equation (2.2) as a means of characterizing earthquake scaling properties. This stress drop value is not necessarily representative of stress drop during the earthquake at small scale lengths.

Small earthquakes do not rupture the entire width of the seismogenic zone, and thus may be equidimensional ($L \simeq W$). For large events, however, W remains essentially constant and L exceeds W, hence $L_c = W_0$ (where W_0 is the thickness of the seismogenic crust). For such events, self-similar scaling can not persist. *Pacheco at al.* [1992] have shown a breakdown in magnitude-frequency statistics, and presumably in self-similarity as well, for strike-slip earthquakes at $M_w \approx 6.0$ and for dip-slip earthquakes at $M_w = 7.4$. These magnitudes correspond to the size threshold at which the width of the seismogenic zone begins to constrain source dimensions.

Assuming constant stress drop, equation (2.2) predicts that for large strike-slip earthquakes mean slip D increases rapidly for small fault aspect ratios ($L/W < 2$) and asymptotically approaches a constant value related to fault width W for larger aspect ratios (Scholz [1982] called these models "W-models"). Despite this expectation, Scholz [1982] presented data that suggest the empirical law that fault length L and mean slip D are linearly related for large strike-slip over a wide magnitude range. He conjectured a breakdown of conventional continuum models (stress drop correlated with length) and proposed an alternative explanation, the "L-model". Romanowicz [1992] argued that empirical scaling of large strike-slip earthquakes was inconsistent with the L-model hypothesis scaling of large strike-slip earthquakes. She observed a linear relation between L and seismic moment M_o, implying approximately constant average slip on the order of 3-5 m for the largest strike-slip earthquakes. This observation supports W-model-scaling for which D is governed by W; however, her approach differed from that of Scholz [1982] in that the fault width was allowed to vary. These interpretations, although based on measurements for the same earthquakes, strongly depend on a few data points that are not very well constrained and whose values have changed with time as the events in question are re-analyzed. More recently, Bodin and Brune [1996] and compared average slip and rupture length for 27 surface ruptures with predictions from the L-model and the W-model. They concluded that the data provide insufficient constraints to rule out either model, and instead they advance an alternative interpretation in which stress drop is spatially variable.

In this study we consider primarily finite-fault rupture models because we believe they contribute the most accurate estimates of true fault dimensions (Table 2.1). These slip models are typically derived from inversion of low-pass filtered strong motion recordings [Archuleta, 1984; Beroza and Spudich, 1988], sometimes augmented with teleseismic data [Hartzell and Heaton, 1983; Wald et al., 1991], and/or geodetic measurements [Heaton, 1982; Wald and Somerville, 1995; Yoshida et al., 1996]. Other techniques use geodetic data alone to constrain large-scale slip [Bennet et al., 1995]; empirical Green's function analysis can be used to estimate small-scale slip distribution [Dreger, 1994]. Slip in all of these models is spatially variable, and the static stress drop corresponding to these slip distributions is spatially variable as well. In this paper, however, we only report on the scaling properties of average source parameters. In a subsequent paper we will discuss models for spatially variable earthquake slip, based on finite-source rupture models [Mai and Beroza, 2001a] (Chapter 3).

Table 2.1: Source parameters of finite-source rupture models used in this study. Fault length, L, and fault width, W are in km, mean slip D is in m; moment magnitude M_w is computed from each slip model. Events marked with [t] were used this chapter (SS: strike-slip; RV: reverse-faulting; OB: oblique mechanism; N: normal faulting).

No	Location	Date	L	W	D	M_w	M_o	FM	Reference
1 [t]	Kanto	01/09/23	130	70	2.01	7.80	6.04E+20	RV	Wald & Somerville (1995)
2 [t]	San Fernando	02/09/71	19	19	1.35	6.76	1.61E+19	RV	Heaton (1982)
3 [t]	Tabas	09/16/78	95	45	0.38	7.10	5.31E+19	RV	Hartzell & Mendoza (1991)
4 [t]	Coyote Lake	08/06/79	10	10	0.23	5.87	7.56E+17	SS	Liu & Helmberger (1983)
5 [t]	Imperial Valley	10/15/79	35	13	0.39	6.46	5.83E+18	SS	Archuleta (1984)
6 [t]			42	11	0.62	6.59	9.03E+18	SS	Hartzell & Heaton (1983)
7			42	10	0.41	6.45	5.69E+18	SS	Zeng & Anderson (1983)
8 [t]	Borah Peak	10/28/83	52	26	0.39	6.78	1.79E+19	N	Mendoza & Hartzell (1988)
9 [t]	Morgan Hill	04/24/84	30	10	0.26	6.23	2.59E+18	SS	Beroza & Spudich (1988)
10 [t]			27	11	0.17	6.10	1.70E+18	SS	Hartzell & Heaton (1986)
11 [t]	Michoacan	09/19/85	180	140	1.46	8.01	1.21E+21	RV	Mendoza & Hartzell (1988)
12	Nahinni #1	10/05/85	40	17	0.56	6.68	1.26E+19	RV	Hartzell et al. (1994)
13	Nahinni #2	12/23/85	48	21	0.50	6.76	1.65E+19	RV	Hartzell et al. (1994)
14 [t]	N Palm Springs	07/08/86	22	15	0.15	6.10	1.68E+18	OB	Hartzell (1989)
15 [t]			22	15	0.13	6.06	1.45E+18	OB	Mendoza & Hartzell (1988)
16 [t]	Whittier Narrows	10/10/87	10	10	0.26	5.91	8.67E+17	OB	Hartzell & Iida (1990)
17 [t]	Elmore Ranch	11/24/87	25	10	0.28	6.19	2.30E+18	SS	Larsen et al. (1992)
18 [t]	Superstition Hills	11/24/87	24	10	1.17	6.61	9.30E+18	SS	Larsen et al. (1992)
19 [t]			20	12	0.83	6.48	6.31E+18	SS	Wald et al. (1990)
20 [t]	Loma Prieta	10/18/89	40	14	1.29	6.87	2.39E+19	OB	Beroza (1991)
21 [t]			38	17	1.06	6.85	2.26E+19	OB	Steidl et al. (1991)
22 [t]			40	20	1.14	6.94	3.01E+19	OB	Wald et al. (1991)
23			40	14	1.80	6.96	3.31E+19	OB	Zeng & Anderson (2000)
24 [t]	Sierra Madre	06/28/91	7	6	0.16	5.51	2.21E+17	RV	Wald (1992)
25 [t]	Joshua Tree	04/23/92	35	20	0.11	6.23	2.65E+18	SS	Bennet et al. (1995)
26 [t]			22	20	0.12	6.12	1.80E+18	SS	Hough & Dreger (1995)
27 [t]	Landers	06/28/92	84	18	1.39	7.18	6.95E+19	SS	Cohee & Beroza (1994)
28 [t]			80	15	2.00	7.22	7.92E+19	SS	Cotton & Campillo (1995)
29 [t]			78	15	2.47	7.27	9.53E+19	SS	Wald & Heaton (1994)
30			77	15	1.99	7.20	7.59E+19	SS	Zeng & Anderson (2000)
31 [t]	Northridge	01/17/94	17	26	0.71	6.63	1.03E+19	RV	Dreger (1995)
32 [t]			20	26	1.07	6.79	1.85E+19	RV	Hudnut et al. (1996)
33 [t]			18	21	1.00	6.68	1.24E+19	RV	Wald et al. (1996)
34			18	24	0.73	6.63	1.04E+19	RV	Zeng & Anderson (2000)
35 [t]	Kobe	01/17/95	64	20	0.35	6.73	1.49E+19	SS	Sekiguchi et al. (1996)
36 [t]			60	16	0.66	6.83	2.10E+19	SS	Yoshida et al. (1996)
37 [t]			60	20	0.82	6.96	3.23E+19	SS	Wald (1996)
38			60	20	0.71	6.91	2.80E+19	SS	Zeng & Anderson (2000)
39	Hyuga-Nada #1	10/19/96	32	32	0.57	6.81	1.92E+19	RV	Yagi & Kikuchi (1999)
40	Hyuga-Nada #2	12/02/96	29	29	0.46	6.69	1.27E+19	RV	Yagi & Kikuchi (1999)
41	Izmit (Turkey)	08/17/99	135	20	3.26	7.59	2.90E+20	SS	Bouchon et al. (2000)
42			125	22	1.52	7.38	1.38E+20	SS	Sekigucki & Iwata (2000)
43			85	22	2.36	7.39	1.45E+20	SS	Yagi & Kikuchi (2000)
44	Chi-Chi (Taiwan)	09/20/99	84	42	3.93	7.72	4.57E+20	RV	Zeng & Anderson (2000)

2.4 Source Dimensions

The definition of rupture size, i.e. fault length or fault width can be somewhat prob-
lematical. Fault length can be estimated from surface rupture length, if surface rupture
occurred [*Wyss*, 1979], or from the spatial extent of early aftershocks [*Kanamori and An-
derson*, 1975; *Darragh and Bolt*, 1987]. These two measurements can give substantially
different results [*Wells and Coppersmith*, 1994]. Determination of fault width relies on
aftershocks only, or possibly the thickness of the seismogenic layer in the case of large
strike-slip earthquakes [*Scholz*, 1994].

Slip in earthquakes as imaged by finite-fault inversion techniques is invariably found to
be heterogeneous. The overall dimensions of the rupture planes used in these studies are
chosen to be more than large enough to accommodate the entire fault rupture, and therefore
may produce slip models with significant portions of low (or even zero) slip towards their
edges. Thus, using the dimension of the finite-source model may lead to an overestimate of
the "true" rupture area, and hence to scaling laws that do not represent source behavior
accurately. This, together with the intrinsically heterogeneous nature of slip in earthquakes,
raises the question of how to characterize the spatial extent of the source.

To analyze heterogeneous slip distributions (parametrized by slip values in a two-
dimensional array of subfaults) we introduce *equivalent* (*effective*) source dimensions, based
on the definition of autocorrelation width [*Bracewell*, 1986]. For a given function, f, auto-
correlation width, W^{ACF}, is the area under the autocorrelation function of that function,
$f \star f = \int f(u) \cdot f(u-x)dx$, normalized by the zero-lag value ($x = 0$) of the autocorrelation
function (i.e. its maximum):

$$W^{ACF}_{equivalent} = \frac{\int_{-\infty}^{\infty}(f \star f)\,dx}{f \star f \mid_{x=0}}$$

(2.3)

Using this definition, we calculate the effective length L_{eff} (width W_{eff}) of the fault from
the 1D-slip function that is computed by summing the slip values in the individual subfaults
in down-dip (along-strike) direction. Figure 2-1 displays the results of this measurement
for the 1989, Loma Prieta earthquake ($M_w = 6.9$) [*Beroza*, 1991]. For consistency among
seismic moment estimates, we then scale the effective mean slip D_{eff} such that seismic
moment is preserved. *Somerville et al.* [1999] defined the effective dimensions by successive
removal of rows (columns) whose mean slip is smaller than a certain fraction of the mean
slip of the entire slip model. In this procedure, rows/columns with small mean slip are
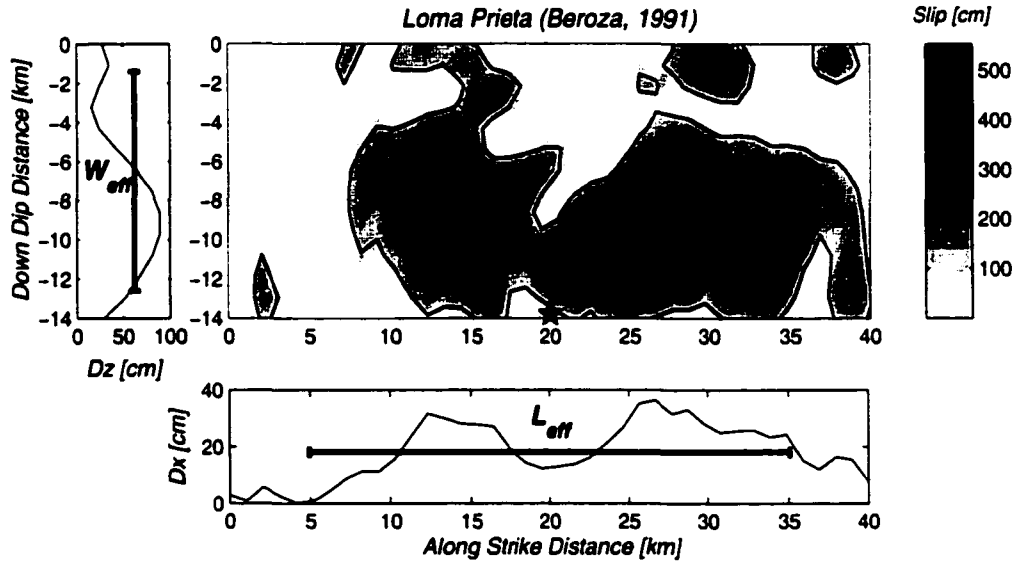
Figure 2-1: Rupture model for the 1989, Loma Prieta earthquake ($M_w = 6.9$) from strong motion data [*Beroza* 1991], showing the sum of strike-slip and reverse motion. The star marks the hypocenter, slip values in each subfault are shown in gray scale, contoured at 100 cm intervals. Side panels show effective length L_{eff} and effective width W_{eff} from the autocorrelation function of the summed slip contributions of all subfaults in down-dip (D_x) and along-strike direction (D_z), respectively. Effective average displacement, D_{eff}, is scaled to match seismic moment.

completely removed, and do not contribute to the rupture area. An advantage of our definition is that the contribution of rows/columns of low slip is reflected in the resulting effective length/width estimates.

Figure 2-2 compares the measurements based on original dimensions (used in the finite-source inversion) versus effective dimensions, indicating a median change in length ($\Delta L = L_{eff}/L$) and width ($\Delta W = W_{eff}/W$) of 0.85 and 0.77, respectively. Therefore, in order to preserve seismic moment, the effective mean slip D_{eff} has to increase (on average by a factor of about 1.5). It is interesting to note that the change in length and width for dip-slip events is about equal ($\Delta L = 0.84$, $\Delta W = 0.85$), and generally does not depend on earthquake size. For strike-slip events, however, the change in length is more pronounced than in width ($\Delta L = 0.75$, $\Delta W = 0.91$), and both seem to decrease for events smaller than $M_w = 6.5$ (i.e. the source dimensions for smaller events were overestimated more than for larger events). Images of fault rupture, however, typically have better horizontal than vertical resolution, meaning that displacement is smeared out primarily in the down-dip

Total versus Effective Area
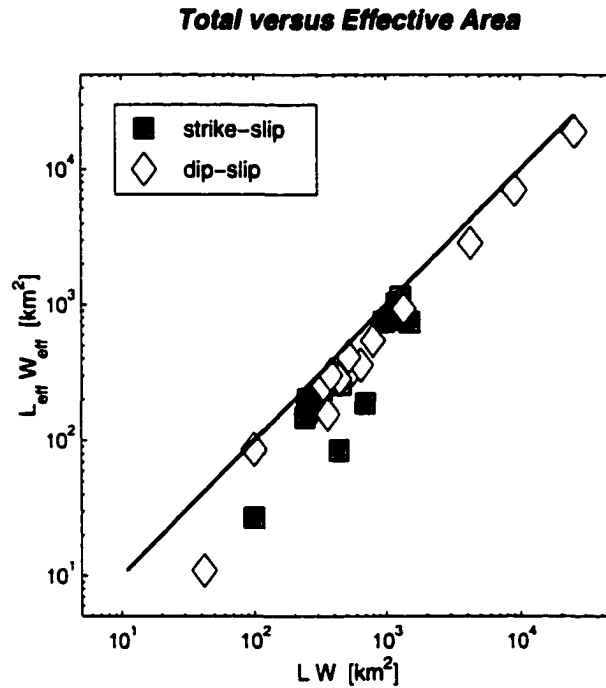
Figure 2-2: Illustration of the change in area associated with the effective dimensions. The graph shows $L_{eff}W_{eff}$ over LW, the solid line has slope 1. The data points asymptotically approach the line of slope 1 for larger areas,indicating that the source extent of smaller events was more overestimated than the extent of larger events. For strike-slip events, the change in length, ΔL, is larger than the change in width, ΔW; for dip-slip events, ΔL and ΔW are about equal.

direction. We therefore can expect a smaller change in width than in length when we use our definition of the equivalent source dimensions.

2.5 Source-Scaling Properties

In Figure 2-3, a-c we display fault length, L_{eff}, fault width, W_{eff}, and mean slip, D_{eff}, versus seismic moment, M_o, separated into three categories: 'all events', strike-slip and dip-slip events. We combine earthquakes with oblique-slip, reverse or normal focal mechanisms into the category dip-slip events because the rupture width of oblique events will likely exceed the thickness of the seismogenic layer, since the fault is typically not vertical. Hence, we anticipate that oblique and dip-slip earthquakes might have similar scaling behavior

with respect to fault width. We analyze multiple studies of the same event as separate earthquakes as well as using weighted averages in place of the individual studies. Since the scaling relations are very similar, and the t-tests for the self-similar scaling hypothesis are identical, we only report results based on the averaged source parameters for earthquakes with multiple slip models. We examine the scaling properties of the source dimensions by fitting the generic equation $\log Y = a + b \cdot \log M_o$ to the data (Figure 2-3). Since we are interested in predicting parameters for seismic hazard purposes, and to compare our results to previously determined relationships, we use ordinary least-squares (OLS) regression for all analyses. χ^2-tests indicate that the distribution of residuals for all data is consistent with a (log)-normal distribution of the data at 95% significance level. We find from standard t-statistics that all relations are statistically significant at 95% probability level, except the relations between mean displacement and fault length (Table 2.2, 2.3), which are significant at 80% probability level.

The scaling of fault length with seismic moment (Figure 2-3a, Table 2.3) shows slope $b \approx 0.40 \pm 0.05$ for all three categories, which, at 95% confidence level, is consistent with self-similar scaling, slope $b = 0.33$. The least-squares fit of fault width to seismic moment shows slope $b \approx 0.33$ only for dip-slip events (Figure 2-3b, Table 2.3). For strike-slip events, the fault width is almost constant over this range of seismic moment, with slope $b = 0.17 \pm 0.06$ and a low correlation coefficient, $r^2 = 0.58$, indicating that the correlation of width and seismic moment is weak (Table 2.3). Clearly, self-similar scaling breaks down for large strike-slip earthquakes that rupture through the entire seismogenic crust. Since they show similar scaling of M_o with L_{eff}, strike-slip earthquakes must have larger mean slip than dip-slip events of comparable moment. This is reflected in the scaling of mean slip D_{eff} with seismic moment (Figure 2-3c, Table 2.3), in which strike-slip earthquakes show slope $b = 0.43 \pm 0.10$, compared to slope $b = 0.25 \pm 0.09$ for dip-slip earthquakes. Both relations, however, are consistent with self-similar scaling at 95% significance level.

The ratio of mean slip to fault width, D/W, can be interpreted as an *average* strain or stress drop (equation 2.2). From the scaling of mean slip and fault width with seismic moment, we find for strike-slip earthquakes: $D_{eff}/W_{eff} \propto M_o^{0.26}$. In this case, we observe a positive correlation between the ratio of average displacement to fault width and seismic moment, indicating that stress drop increases with seismic moment for strike-slip earthquakes. For dip-slip earthquakes, on the other hand, we find $D_{eff}/L_{eff} \propto M_o^{-0.10}$, i.e. constant stress drop scaling. In Figure 2-4 we plot D_{eff}/W_{eff} against seismic moment M_o.
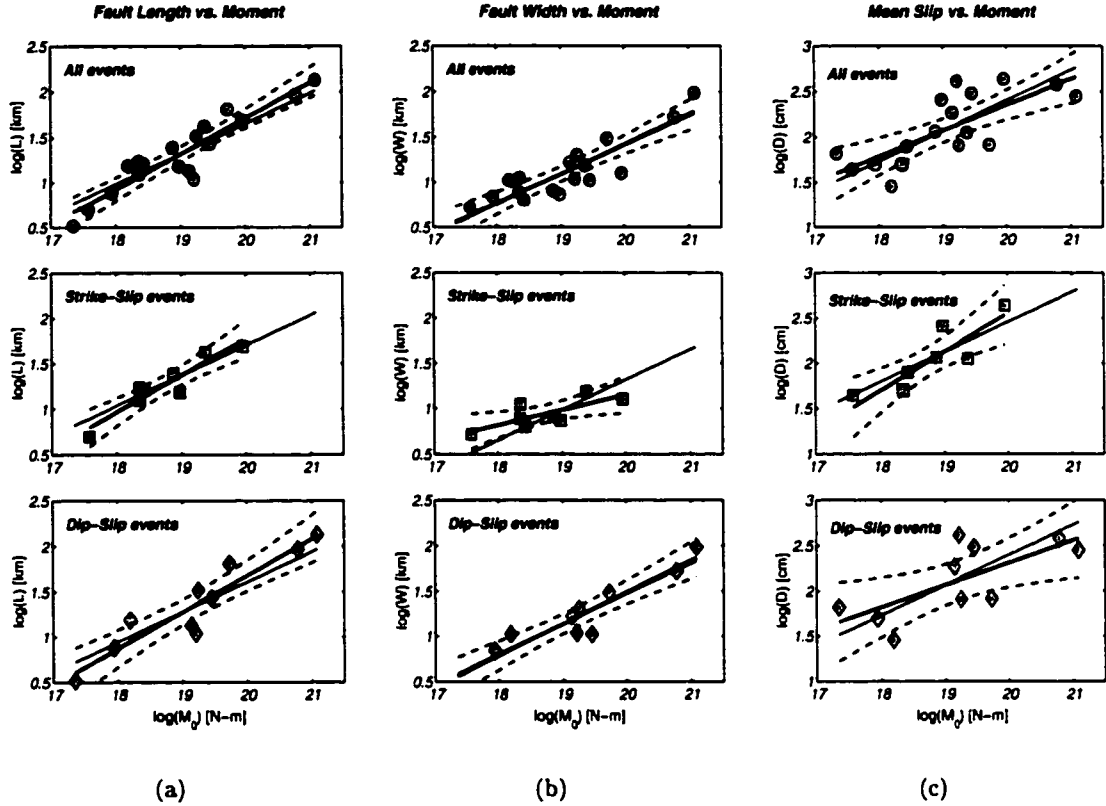
Figure 2-3: (a) Scaling of effective fault length L_{eff} (in km) with seismic moment M_o (in N-m) for all events (top), strike-slip events (middle) and dip-slip events (bottom) on log-log scale. The thin solid line indicates the slope for self-similar scaling, $b = 0.33$, the broken lines denote the 95% confidence interval. The heavy solid line represents the best least-squares fit to the data points, with slopes $b = 0.39(\pm0.04)$, $b = 0.40(\pm0.06)$ and $b = 0.40(\pm0.05)$, from top to bottom. (b) Same as (a) for the scaling of effective fault width W_{eff} (in km) with seismic moment M_o (in N-m). Note how the scaling for strike-slip earthquakes (solid line, middle panel) deviates from self-similarity with slope $b = 0.17(\pm0.05)$. Dip-slip earthquakes show self-similar scaling with slope $b = 0.35(\pm0.04)$. (c) Same as (a) for the scaling of effective mean slip D_{eff} (in cm) with seismic moment M_o (in N-m). The least squares fit for strike-slip earthquakes has slope $b = 0.43(\pm0.10)$, for dip-slip earthquakes we find slope $b = 0.25(\pm0.09)$, indicating that strike-slip earthquakes must have larger mean slip than dip-slip events of comparable moment. Both relations are consistent with self-similar scaling at 95% confidence level, but the width-moment relation (b) clearly shows a breakdown of self-similarity for strike-slip earthquakes.

This graph suggests an increase in the D/W-ratio for strike-slip earthquakes (i.e. average stress drop increases with seismic moment), while dip-slip events show no trend (constant average stress drop). A similar trend exists in the data compiled by *Wells and Coppersmith*

Table 2.2: Scaling coefficients between the source parameters as given by the fault-slip inversion. In case of multiple slip models for a single earthquake, average source dimensions were used.

Equation	slope (error) b_1 (σ_{b_1})	intercept (error) b_0 (σ_{b_0})	standard deviation σ_y	correlation coefficient r^2
All Events				
$\log(L) = b_0 + b_1 M_o$	0.35 (0.04)	-5.20 (0.74)	0.16	0.84
$\log(W) = b_0 + b_1 M_o$	0.29 (0.04)	-4.28 (0.76)	0.17	0.77
$\log(A) = b_0 + b_1 M_o$	0.64 (0.06)	-9.44 (1.14)	0.25	0.88
$\log(D) = b_0 + b_1 M_o$	0.35 (0.06)	-4.98 (1.11)	0.24	0.69
$\log(D) = b_0 + b_1 \log(L)$	0.65 (0.22)	0.69 (0.34)	0.35	0.36
Strike-Slip Earthquakes				
$\log(L) = b_0 + b_1 M_o$	0.36 (0.06)	-5.15 (1.11)	0.11	0.86
$\log(W) = b_0 + b_1 M_o$	0.09 (0.06)	-0.54 (1.14)	0.12	0.26
$\log(A) = b_0 + b_1 M_o$	0.44 (0.11)	-5.59 (2.08)	0.21	0.72
$\log(D) = b_0 + b_1 M_o$	0.55 (0.10)	-8.68 (1.95)	0.20	0.82
$\log(D) = b_0 + b_1 \log(L)$	1.11 (0.46)	-0.07 (0.70)	0.34	0.49
Dip-Slip Earthquakes				
$\log(L) = b_0 + b_1 M_o$	0.38 (0.05)	-5.71 (0.97)	0.18	0.88
$\log(W) = b_0 + b_1 M_o$	0.33 (0.03)	-4.93 (0.65)	0.12	0.92
$\log(A) = b_0 + b_1 M_o$	0.71 (0.07)	-10.64 (1.39)	0.26	0.92
$\log(D) = b_0 + b_1 M_o$	0.29 (0.07)	-3.88 (1.39)	0.26	0.67
$\log(D) = b_0 + b_1 \log(L)$	0.52 (0.26)	0.96 (0.41)	0.36	0.34

[1994], as shown in Figure 2-5, in which we plot the ratio of average surface displacement to rupture width versus seismic moment for strike-slip and dip-slip earthquakes. These observations imply that strike-slip earthquakes show non-self-similar scaling of source dimensions. Dip- slip earthquakes, on the other hand, obey self-similar source scaling over this range of earthquake sizes. Presumably, dip-slip events large enough to rupture the entire seismogenic crust would show a breakdown in self-similarity as well [*Pacheco et al.*, 1992].

Table 2.3: Scaling coefficients between the source parameters as given by the *effective* source dimensions. In case of multiple slip models for a single earthquake, average source dimensions were used.

Equation	slope (error) b_1 (σ_{b_1})	intercept (error) b_0 (σ_{b_0})	standard deviation σ_y	correlation coefficient r^2
All Events				
$\log(L) = b_0 + b_1 M_o$	0.39 (0.04)	-6.13 (0.74)	0.16	0.87
$\log(W) = b_0 + b_1 M_o$	0.32 (0.04)	-5.05 (0.74)	0.16	0.81
$\log(A) = b_0 + b_1 M_o$	0.72 (0.06)	-11.18 (1.18)	0.26	0.89
$\log(D) = b_0 + b_1 M_o$	0.29 (0.06)	-3.34 (1.18)	0.26	0.57
$\log(D) = b_0 + b_1 \log(L)$	0.46 (0.19)	1.47 (0.27)	0.34	0.26
Strike-Slip Earthquakes				
$\log(L) = b_0 + b_1 M_o$	0.40 (0.06)	-6.31 (1.15)	0.12	0.88
$\log(W) = b_0 + b_1 M_o$	0.17 (0.06)	-2.18 (1.09)	0.11	0.58
$\log(A) = b_0 + b_1 M_o$	0.57 (0.10)	-8.49 (1.85)	0.19	0.85
$\log(D) = b_0 + b_1 M_o$	0.43 (0.10)	-6.03 (1.85)	0.19	0.76
$\log(D) = b_0 + b_1 \log(L)$	0.77 (0.34)	1.04 (0.45)	0.29	0.46
Dip-Slip Earthquakes				
$\log(L) = b_0 + b_1 M_o$	0.40 (0.05)	-6.39 (1.04)	0.19	0.88
$\log(W) = b_0 + b_1 M_o$	0.35 (0.04)	-5.51 (0.81)	0.15	0.90
$\log(A) = b_0 + b_1 M_o$	0.75 (0.09)	-11.90 (1.67)	0.31	0.90
$\log(D) = b_0 + b_1 M_o$	0.25 (0.09)	-2.62 (1.67)	0.31	0.50
$\log(D) = b_0 + b_1 \log(L)$	0.35 (0.26)	1.64 (0.37)	0.39	0.19

2.6 Original versus Effective Dimensions

In Table 2.4 we compare scaling relations based on the original and the effective dimensions of finite-source rupture models. We also show scaling laws based on a global catalog of crustal earthquakes [*Wells and Coppersmith*, 1994] (henceforth abbreviated as W&C), and scaling laws we computed from the data used in previous studies [*Scholz*, 1982; *Romanowicz*, 1992] (henceforth abbreviated as S&R). Because *Wells and Coppersmith* [1994] performed

Strain versus Moment
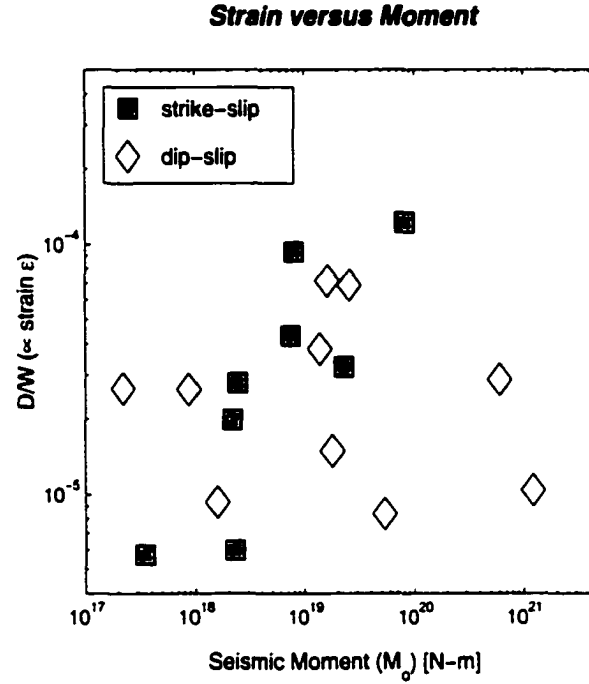
Figure 2-4: Plot of the ratio between mean slip and fault width, D_{eff}/W_{eff}, (both in m) over seismic moment M_o (in N-m) on log-log-scale. The fault width W_{eff} replaces the characteristic length scale L_c in equation (2), and the ratio D_{eff}/W_{eff} represents a measure of the average strain resulting from the faulting process. This ratio is not correlated with seismic moment for dip-slip earthquakes (mean value $D_{eff}/W_{eff} \approx 1 \times 10^{-5}$). For strike-slip earthquakes, however, we observe the tendency that strain appears to increase with seismic moment, ranging from 1×10^{-5} for the small events to 3×10^{-4} for the large earthquakes. For a typical crustal rigidity ($\mu = 30\,\text{GPa}$) we estimate an average static stress drop of $\approx 3\,\text{MPa}$ for dip-slip events, while for strike-slip events, the static stress drop appears to increase with seismic moment, in the range of $0.3\,\text{MPa}$ to $9\,\text{MPa}$.

the regression of fault parameters versus moment magnitude, M_w, we convert their scaling relations for dip-slip and 'all events' to seismic moment using the relation $M_w = 0.67 \cdot \log M_o - 10.7$ [Hanks and Kanamori, 1979]. We separately analyzed their data for strike-slip events for comparison. The finite-source scaling laws and the scaling relationships based on the W&C and S&R-data show similarities, but also important differences. Generally, the S&R-relations seem to be more applicable to very large strike-slip events, whereas our results and the W&C-relations represent the scaling of both very large and moderate-sized strike-slip earthquakes.
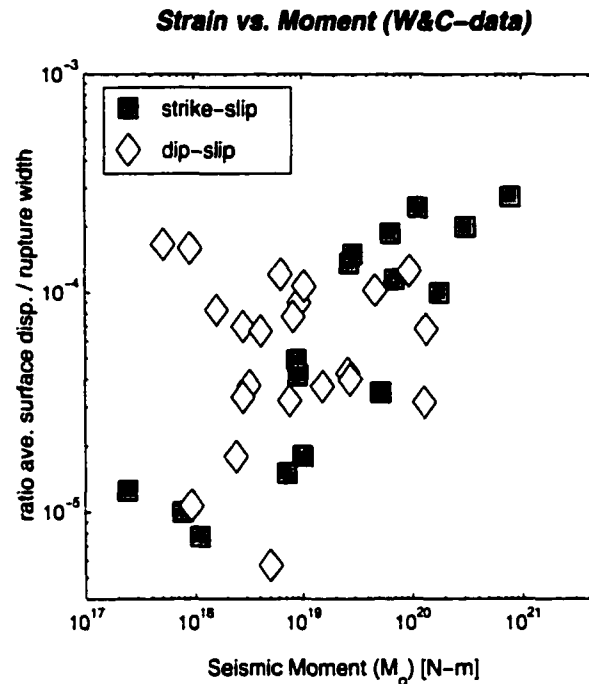
Figure 2-5: Plot of the ratio of average surface displacement to rupture width (D_{as}/W) over seismic moment for 38 earthquakes with reliable source parameters, taken from *Wells and Coppersmith* [1994]. The data show a clear increase in the ration of (D_{as}/W) with increasing seismic moment for strike-slip earthquakes, but no trend for dip-slip earthquakes.

We use t-tests to evaluate the significance of using effective versus original source dimensions for the finite-source slip models. We find that the slopes for scaling relationships of dip-slip events are not statistically different at 95% confidence level for the two cases (Table 2.3). The same is true if we consider all events.For the strike-slip finite-source events the difference in the scaling of fault length with seismic moment is not significant at 95% confidence level; however, all other relations (scaling of fault width, fault area and mean slip with seismic moment) are significantly different when using effective dimensions instead of original dimensions. The width-moment relation has larger slope, and with the small change in the length-moment relation, the slope in the area-moment relation increases considerably. Therefore, the slope in the relation between mean-slip and moment must decrease for strike-slip events. We also find that the length-moment relation for strike-slip and dip slip events is not significantly different (at 95% level), while all the others are.

Table 2.4: Scaling coefficients from different data sets. Coefficients in *italics* are unreliable due to small correlation coefficients and large standard errors. Note that the W&C-data for length, L, are given in surface-rupture length, SRL.

Equation	This Data		W&C Dataset	S&R Dataset
	Org. dimens.	Eff. dimens.		
	b_1 (σ_{b_1})	b_0 (σ_{b_0})	b_1 (σ_{b_1})	b_0 (σ_{b_0})
All Events				
$\log(L) = b_0 + b_1\,M_o$	0.35 (0.04)	0.39 (0.04)	0.39 (0.01)	
$\log(W) = b_0 + b_1\,M_o$	0.29 (0.04)	0.32 (0.04)	0.21 (0.01)	
$\log(A) = b_0 + b_1\,M_o$	0.64 (0.06)	0.72 (0.06)	0.61 (0.02)	
$\log(D) = b_0 + b_1\,M_o$	0.35 (0.06)	0.29 (0.06)	0.46 (0.05)	
$\log(D) = b_0 + b_1\,\log(L)$	*0.65 (0.22)*	*0.46 (0.19)*	*0.88 (0.11)*	
Strike-Slip Earthquakes				
$\log(L) = b_0 + b_1\,M_o$	0.36 (0.06)	0.40 (0.06)	0.43 (0.02)	0.46 (0.05)
$\log(W) = b_0 + b_1\,M_o$	0.09 (0.06)	0.17 (0.06)	0.13 (0.01)	0.06 (0.04)
$\log(A) = b_0 + b_1\,M_o$	0.44 (0.11)	0.57 (0.10)	0.56 (0.02)	0.52 (0.04)
$\log(D) = b_0 + b_1\,M_o$	0.55 (0.10)	0.43 (0.10)	0.45 (0.02)	0.52 (0.06)
$\log(D) = b_0 + b_1\,\log(L)$	*1.11 (0.46)*	*0.77 (0.34)*	*1.04 (0.13)*	*0.64 (0.13)*
Dip-Slip Earthquakes				
$\log(L) = b_0 + b_1\,M_o$	0.38 (0.05)	0.40 (0.05)	0.39 (0.02)	
$\log(W) = b_0 + b_1\,M_o$	0.33 (0.03)	0.35 (0.04)	0.27 (0.02)	
$\log(A) = b_0 + b_1\,M_o$	0.71 (0.07)	0.75 (0.09)	0.65 (0.04)	
$\log(D) = b_0 + b_1\,M_o$	0.29 (0.07)	0.25 (0.09)	0.05 (0.14)	
$\log(D) = b_0 + b_1\,\log(L)$	*0.52 (0.26)*	*0.35 (0.26)*	*0.31 (0.27)*	

While the slopes for the scaling laws may not be significantly different using effective versus original source dimensions, the intercepts are (Tables 2.2, 2.3). This reflects the fact that the smaller effective dimensions imply higher average displacements for a fixed seismic moment. Using (2.2), we estimate an average increase in stress drop by a factor of about 2.5 (this value decreases with increasing seismic moment because the reduction in source dimensions is more pronounced for small than for large earthquakes). To compare

our results with those derived from other data sets, we use the scaling laws based on the effective source dimensions because we believe that they reflect most accurately the source-scaling properties for crustal earthquakes.

2.7 Comparison with Other Data

For strike-slip earthquakes, the finite-source scaling relations agree very well (small differences are not statistically significant) with the scaling relationships based on the W&C-data (Table 2.4). The scaling of mean slip with fault length is unreliable for the finite-source data (large standard errors and low correlation coefficient), hence we cannot resolve possible differences. For dip-slip events we find good agreement between the finite-source relations and scaling relationships given by *Wells and Coppersmith* [1994] only for the length-moment relation. Our results indicate a larger slope in the width-moment relation, and also area-moment relation, than the W&C-relations. This difference is probably explained by the two largest dip-slip events in our catalog (the 1923, Kanto (Japan) and 1985, Michoacan (Mexico) earthquakes), which *Wells and Coppersmith* [1994] do not list in their compilation.

The scaling laws based on the S&R-data are for strike-slip events only and deviate from the W&C-relations and the finite-source scaling laws in that the slope of the length-moment relation is larger, but the slope of the width-moment relation is smaller. Together, the area-moment relation also shows a smaller slope that is compensated by a steeper slope in the displacement-moment relation; however, only the difference in the width-moment relation is statistically significant. Using the S&R-relations, for instance, an increase of rupture area for strike-slip earthquakes is accomplished primarily by increasing the rupture length. The relations between mean slip and fault length are considered very uncertain for all three data sets due to the large standard errors and low correlation coefficient (for example, in all cases, we cannot rule out (at 95% confidence) the hypothesis of slope $b = 0.5$ or slope $b = 1$).

It is important to note that the small differences in the slopes and intercepts in the above scaling relations produce substantially different rupture size predictions. As an illustration, consider two strike-slip earthquakes, a moderate-sized $M_w = 6.0$ and a large $M_w = 7.5$ event. The S&R-relations predict source dimensions of $15 \times 10\,\text{km}$ and $170 \times 15\,\text{km}$, respectively, the W&C-data yield $14 \times 7\,\text{km}$ and $111 \times 17\,\text{km}$, while our finite-source relations predict $18 \times 11\,\text{km}$ and $114 \times 18\,\text{km}$. For the $M_w = 7.5$ event, the S&R-relations predict an

extremely long fault, with mean slip on the order of 2.0 m. The finite-source relations and the W&C-relations roughly agree on a much shorter fault with mean slip of about 2.8 m. These estimates can be compared to the 1992 Landers, California, earthquake ($M_w = 7.3$), for which $L \approx 80$ km, and $D \approx 2$ m.

The data presented in this paper lack the very long strike-slip earthquakes. Although there exist estimates of the slip distribution for the 1906 San Francisco earthquake ($M_w \approx 7.9$), based on sparse geodetic data [Thatcher et al., 1997] and seismic data [Wald et al., 1993], we decided not to include this event in our data compilation because slip on all parts of the faults could not be resolved from the geodetic data, and the two models markedly disagree with each other. However, we believe that the observed trends for strike-slip earthquakes can be extended to very long ruptures. Using the relations presented in Table 2.2, we estimate a rupture area of 3,800 km² for a $M_w \approx 7.9$ strike-slip earthquake. For a rupture width of about 10 km this estimate would translate into a 380 km long earthquake with mean slip on the order of 6 m, roughly in agreement with the source parameters for the 1906 San Francisco event.

Several major earthquakes occurred in summer and fall 1999 (Turkey, Izmit, 08/17/1999, $M_w = 7.6$; Taiwan, Chi-Chi, 09/20/1999, $M_w = 7.6$; Mexico, Oaxaca, 09/30/1999, $M_w = 7.4$; California, Hector Mine, 10/16/1999, $M_w = 7.1$; Turkey, 11/12/199, $M_w = 7.1$). For many of these earthquakes, preliminary finite-source models exist, based on rapid-response modeling of low-frequency teleseismic waves or geodetic data. However, we believe that much better models will be published soon that also include strong motion data and eliminate current discrepancies (e.g. there are strong contradictions between the seismological and the geodetic slip distribution for the Hector Mine earthquake). Therefore, we have not yet included these events in our data base. Nevertheless, these earthquakes can be used to test the scaling relations developed in this paper. Using the scaling relations in Table 2.2, we estimate a rupture area of about 2400 km² for the Izmit earthquake ($M_w = 7.6$), a rupture length on the order of 105 km for a rupture width of 22 km, and mean slip of about 3.5 m. These values roughly agree with the preliminary finite-source results. For the Hector Mine earthquake and the Nov. 12, 1999, Turkey earthquake (both $M_w = 7.1$, strike-slip), we estimate $L = 70$ km, $W = 15$ km and $D = 1.5$ m, values that are similar to the results of the preliminary finite-source inversions. Because of this general consistency of our source-parameter estimates for the recent large strike-slip earthquakes with the preliminary finite-fault inversions, we are confident that we can extend the observed trends for strike-slip

earthquakes to very long ruptures.

As the final results for slip inversions of these recent destructive earthquakes have been published since the appearance of this paper, we recalculated the regressions for developing the above scaling relations (coefficients are listed in Table A.1 in Appendix A). As expected, the updated regression results show only minor changes compared to the original results [*Mai and Beroza*, 2000]. Appendix A also provides an equation relating moment magnitude, M_w, to source area, A, which is commonly used in engineering practice. The deviation of this relation to the widely-used equation by *Wells and Coppersmith* [1994] is remarkable. Our results, however, are in excellent agreement with the more recent study by the *WorkingGroup99* [2000] in that the scaling of large strike-slip earthquake, and hence the prediction of their ground motion intensities, warrants extra care.

2.8   Scaling of Mean Slip

The scaling laws in Figure 2-3 and Table 2.3 suggest constant stress-drop scaling for dip-slip earthquakes, but a breakdown in self-similarity for strike-slip earthquakes. The trend in Figure 2-4 also supports the observation that stress drop increases with seismic moment for large strike-slip earthquakes. This argument is further strengthened by the data shown in Figure 2-5. The rupture width is essentially confined to the thickness of the seismogenic zone, W_0, for large strike-slip events, and as moment increases, both stress drop and rupture lengths tend to increase. This behavior manifests itself in a non-linear relation between mean slip and fault length. For a constant stress drop model, mean slip may increase linearly with fault length ("L-model"), or mean slip may grow with fault width, approaching a constant value when the fault width saturates ("W-model"). However, the strike-slip earthquakes in our catalog do not show slip saturation for very large events. Instead, slip continues to increase, albeit at a decreasing rate. In this case, equation 2.2 predicts that large strike-slip events have higher average static stress drop than small strike-slip events (Figure 2-4). Previously, *Scholz* [1982] has reported an increase in stress drop with seismic moment for strike-slip earthquakes. Independently, *Choy and Boatwright* [1995] and *Pérez-Campos and Beroza* [2001] have found that apparent stress of large strike-slip earthquakes is consistently higher than that of dip-slip events, which is the same sense as we observe for the stress drop.

Another way to examine the apparent non-self similar scaling is by relating mean slip

D and fault length L. The "L-model" results in straight lines with slopes depending on the assumed stress drop. A linear relation between fault length and mean slip would result in straight lines with variable slopes (depending on the assumed *average* stress drop). This L-model is in contrasts to the "W-model" that exhibits a distinct "knee"at $L \approx 2W$ where the slope changes drastically such that slip is independent of rupture length for long ruptures [*Bodin and Brune*, 1996]. *Scholz* [1982] observed a linear relation between mean slip and fault length (L-model) while *Romanowicz* [1992] concluded that mean slip saturates for large earthquakes (W-model). Taking our measurements and the most complete compilation [*Wells and Coppersmith*, 1994], it appears that the field measurements are not well explained by either a simple length or width scaling of average displacement. The scatter in the data, particularly the large uncertainty for the very largest events makes it difficult to discriminate between competing models. We believe, however, that the data presented in this study provide the most accurate estimates of the true fault dimensions. The fact that our scaling laws for strike-slip earthquakes are most consistent with W-model mechanics (i.e., the existence of a locking depth), confirms earlier studies in which less accurate data were used [*Bodin and Brune*, 1996]. We therefore believe that the decreasing increase of mean slip with fault length for large strike-slip events is real, and that this behavior is a manifestation of W-model mechanics.

2.9 Discussion

We have developed source-scaling properties based on finite-source rupture models. These scaling relations suggest a non-linear relationship between average displacement and fault length for strike slip earthquakes (i.e. non-self-similar scaling, in contrast to self-similar scaling observed for dip-slip earthquakes). Such a scaling law is suggestive of W-mechanics, because it is influenced by fault width; however, the earthquakes in our catalog do not show slip saturation for very large strike-slip earthquakes. Instead, slip continues to increase, though at a decreasing rate. The increase of mean slip with increasing rupture length, in excess of the slip increase predicted by the "W-model", may be consistent with a W-model for which the mechanics of the rupture are strongly influenced by the fault width, but slip saturates only for extremely large strike-slip earthquakes.

Scaling relations given by *Wells and Coppersmith* [1994] or computed using the S&R-data support our observation of "W-model"-related scaling. It is important to note, however, that a particular selection of data may lead to contradicting interpretations. Based on a subset of the W&C-data, [*Wang and Ou*, 1998] find that mean slip scales linearly with fault length, thus supporting the "L-model". In contrast, *Bodin and Brune* [1996] conclude from a different subset of the W&C-catalog that the data provide insufficient constraints to rule out either model. *Somerville et al.* [1999] analyze a set of finite-source rupture models that suggest self-similar scaling of fault area and mean slip. Without distinguishing between strike-slip and dip-slip events, they constrain their regression to constant stress-drop (i.e. self-similar) scaling. Hence, their results cannot clarify the issue of non-self-similar scaling for strike-slip earthquakes.

Because the slip distribution in finite-source rupture models is heterogeneous, the scaling relations presented in this study only characterize the overall characteristics of the rupture. Stress drop in these models varies strongly with position and is negative locally (stress increase) as shown, for example, by dynamic rupture modeling [*Mikumo and Miyatake*, 1995; *Beroza and Mikumo*, 1996; *Bouchon et al.*, 1996; *Bouchon*, 1997]. Although the scaling of large strike-slip earthquakes may follow W-mechanics (with a locking depth), heterogeneity in rupture propagation (due to the complex stress distribution) adds variability to the scaling properties, and the width of the fault leads to saturation of the average slip only for the very longest ruptures.

This leaves the question of why slip does not appear to saturate once the rupture length reaches several source depths. An earthquake that begins with an unusually high initial stress drop will tend to propagate farther than a rupture with a small initial stress drop due to the increased energy density in the crack tip [*Scholz*, 1982]. *Heaton* [1990] noted that long, narrow ruptures tend to have higher static stress drop, and therefore larger mean slip (see equation 2.2), a fact that is reflected in the observed increase of stress drop with seismic moment. Thus, a strike-slip earthquake that ruptures a long fault is more likely to occur if it has a strong "push" at the beginning.

Differences in loading mechanisms of small and large earthquakes [1] may provide an

---

[1] Stress accumulation for interplate faults is partly due to viscous drag at the lithospheric base (base loading), and partly due to dislocation pile-ups at horizontal edges of the fault (edge loading). *Matsu'ura and Sato* [1997] derive the stress accumulation rate as $\frac{d\tau}{dt} = V_{pl}(a+bL)$, where V_{pl} is the rate of plate motion, L the fault length, and a, b are constants. For small fault length, the second term dominates (edge loading), while for large L, base loading dominates. In case of edge loading, the dislocation distribution in the end-zones of the fault strongly affects the stress field near the fault edges, and therefore the stress accumulation

alternative explanation for the observation that slip does not saturate for large strike-slip earthquakes. *Matsu'ura and Sato* [1997] showed numerical simulations in which the tectonic loading mechanism may account for the observed break in the moment-length relation for strike-slip earthquakes. More recently, *Fujii and Matsu'ura* [1999] showed good agreement of predicted source-scaling from numerical modeling to the scaling of mean slip versus fault length for a data set of 67 large earthquakes. In both cases, mean slip continues to increase for large strike-slip earthquakes, in agreement with our observations.

Earthquake-scaling relations also have important implications for seismic hazard analysis. While *Wells and Coppersmith* [1994] do not find statistical significant differences in the scaling relations for strike-slip, normal or reverse events, the scaling laws presented in this paper are significantly different for strike-slip and dip-slip earthquakes. It is therefore important to use the corresponding equations when estimating the source size for hypothetical future earthquakes. Moreover, the continuing increase of mean slip with rupture length predicts larger displacements than a simple constant stress-drop model. These larger average displacements are ultimately manifested locally in the stronger excitation of seismic waves and are therefore stronger near-source ground motion.

2.10 Acknowledgements

---

rate is proportional to the inverse of fault length L. Using this model, *Matsu'ura and Sato* [1997] derive a moment-length scaling relation of the form $M_o = \Delta r W \frac{L^2}{(\alpha L + \beta)}$ where α, β are constants, resulting in an L-squared dependence of M_o for moderately large earthquakes (L-model), and a linear L-dependence for very large earthquakes (W-model).

Chapter 3

A Spatial Random-Field Model to Characterize Complexity in Earthquake Slip

3.1 Abstract

Finite-fault source inversions reveal the spatial complexity of earthquake slip over the fault plane. We develop a stochastic characterization of earthquake slip complexity, based on published finite-source rupture models, in which we model the distribution of slip as a spatial random field. The model most consistent with the data follows a *von Karman* autocorrelation function for which the correlation lengths a increase with source dimension. For earthquakes with large fault aspect ratios, we observe substantial differences of the correlation length in the along-strike (a_x) and down-dip (a_z) direction. Increasing correlation length with increasing magnitude can be understood using concepts of dynamic rupture propagation. The power spectrum of the slip distribution can also be well described with a power law decay (i.e. a fractal distribution) in which the fractal dimension D remains scale-invariant, with a median value $D = 2.29 \pm 0.23$, while the corner wave number k_c, which is inversely proportional to source size, decreases with earthquake magnitude, accounting for larger "slip patches" for large-magnitude events. Our stochastic slip model can be used to generate realizations of scenario earthquakes for near-source ground motion simulations.

3.2 Introduction

Images of the spatial and temporal evolution of earthquake slip on fault planes provide compelling evidence that fault displacement is spatially variable at all resolvable scales.

29

These finite-source rupture models are typically derived by inversion of low-pass filtered strong ground motion recordings [e.g. *Beroza and Spudich*, 1988], sometimes augmented with teleseismic data [*Hartzell and Heaton*, 1983; *Wald et al.*, 1991] and/or geodetic measurements [*Heaton*, 1982; *Wald and Somerville*, 1995; *Yoshida et al.*, 1996]. Inversions of geodetic data only are also used to constrain larger-scale slip [*Larsen et al.*, 1992; *Bennet et al.*, 1995], and they provide independent evidence for spatial variability of slip. Some studies of strong motion data indicate that the rupture velocity is spatially variable as well [*Archuleta*, 1984; *Beroza and Spudich*, 1988], adding another degree of complexity into the rupture process. This rupture variablility is of great interest because it strongly influences the level and variability of damaging high-frequency seismic energy radiated by an earthquake [*Madariaga*, 1976, 1981; *Spudich and Frazer*, 1984].

Numerous theoretical studies of extended-source earthquake models describe heterogenous slip distributions on fault planes. *Andrews* [1980b, 1981] showed that a slip spectrum that decays as k^{-2} in the wavenumber domain leads to far-field displacements that follow the widely observed ω^{-2} spectral decay. The fundamental assumption in this model is that stress drop, $\Delta\sigma$, is scale-invariant, i.e. individual large and small earthquakes as well as subevents of different size have about the same stress drop. Based on this concept *Herrero and Bernard* [1994] introduced the "k-square"-model in which the slip spectrum decays as k^{-2} beyond the corner wavenumber, k_c, which is related to fault length. In this representation, slip is fractal. The "k-square"-model assumes that the rupture front propagates with constant rupture velocity v_r, while the rise time depends on wavenumber. The resulting ground motions follow the ω^{-2} decay for far-field displacements, and were used to study directivity effects [*Bernard et al.*, 1996]. Another class of constant stress-drop, extended-source models are the composite source models in which the earthquake is composed of many small events of different size with a fractal size distribution, filling the rupture plane to form the mainshock slip distribution [*Frankel*, 1991; *Zeng et al.*, 1994]. The composite source model has been used successfully to simulate ground motions as well as to invert for earthquake slip distributions [*Zeng et al.*, 1994, 2000; *Su et al.*, 1996]. All of these models have in common a fractal slip distribution, and hence contain no characteristic length scales to describe the size of asperities (large slip patches, areas of high stress drop). The only length scale in the fractal model is a "characteristic" source dimension, L_c (usually fault length) that determines the corner wavenumber, $k_c \propto 1/L_c$, beyond which the spectra show power law decay.
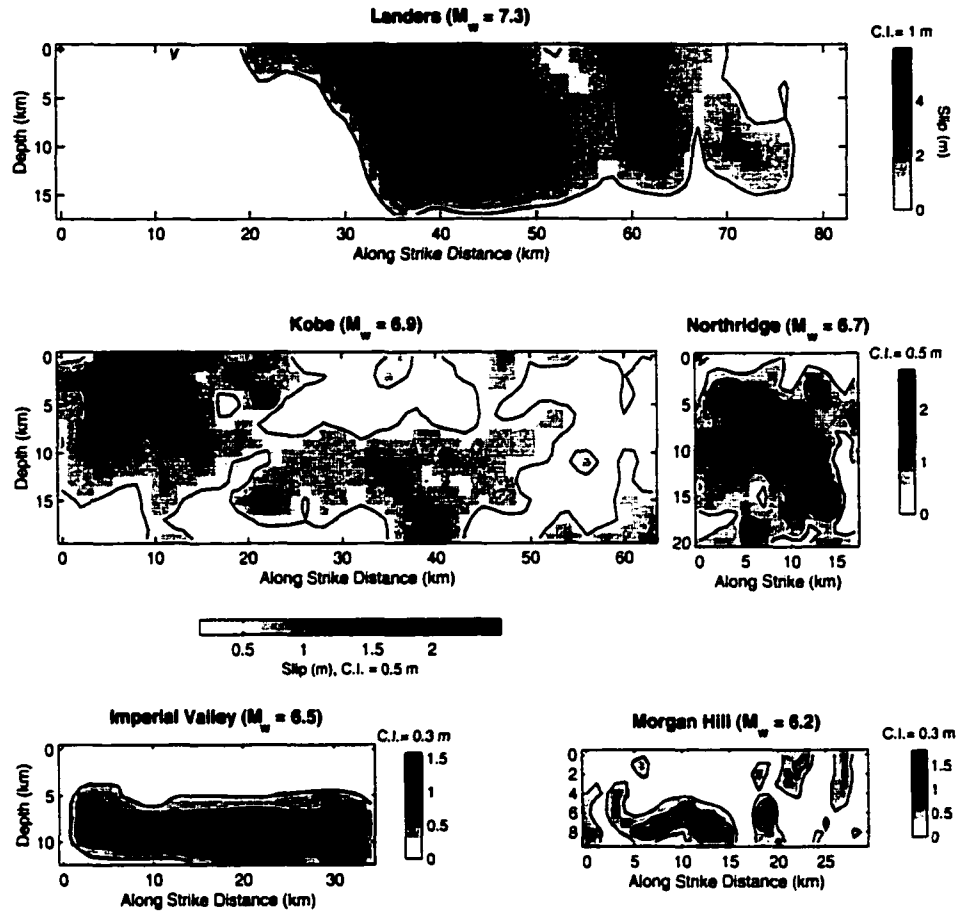
Figure 3-1: Slip distributions from finite-source studies illustrate the spatial variability of slip. The rupture dimensions are plotted approximately on scale, gray-scales indicate slip (in m).

In a recent study, *Somerville et al.* [1999] take a deterministic approach to correlate size and number of asperities with seismic moment for a set of finite-source rupture models. They find that the total number of asperities as well as the asperity size increases with seismic moment. The same study also indicates that for a few selected earthquakes the slip distributions may follow a k^{-2} decay in the wavenumber domain, but there has not yet been an attempt to rigorously verify the k^{-2} model for published finite-source models. *Somerville et al.* [1999] propose that the correlation of size-of-asperity and number-of-asperities with seismic moment can be used to constrain simulated slip distributions that obey a k^{-2} spectral decay.

In this paper we describe a stochastic characterization of the spatial complexity of

earthquake slip as found in finite-source slip inversions (Figure 3-1). We use a spatial random field model for which the slip distribution is described by an autocorrelation function (ACF) in space, or its power spectral density (PSD) in the wavenumber domain, each parametrized by characteristic length scales a_x, a_z. We compiled a database of 44 published finite-source rupture models for 24 different earthquakes Table 2.1, and for each slip model we test whether a Gaussian, an exponential or a von Karman ACF's provide an appropriate description of the inferred slip distribution. We also examine the possibility of slip being fractal (meaning that there are no characteristic scale lengths, aside from the corner wave number k_c) by estimating the fractal dimension, D. Finally, we analyze our measurements of correlation length a_x, a_z, and fractal dimension, D, for dependence on source parameters, i.e. whether there are scaling laws relating the stochastic source parameters (fractal dimension, correlation lengths) with deterministic source parameters (fault length, fault width, seismic moment).

We first discuss the basic concepts of the spatial random field model, and outline the approach we take to determine the best-fitting correlation lengths. We demonstrate the validity of the method and estimate its accuracy using simulated examples of heterogeneous slip maps. Then we apply the technique to published slip distributions, and examine the measured correlation lengths with respect to earthquake source parameters. We discuss the limitations of our analysis, and the implications of the results for rupture dynamics. We use our model to simulate slip distributions for hypothetical future earthquakes that can be used to calculate synthetic near-field ground motions.

3.3 Finite-Source Models as Spatial Random Fields

Spatial random field models are widely used in geosciences to describe quantities with non-homogeneous spatial distribution [*Goff and Jordan*, 1988; *Turcotte*, 1989; *Holliger and Levander*, 1992]. They are characterized either in space by an autocorrelation function, $C(r)$, or in the Fourier domain by a power spectral density, $P(k)$, where r is distance and k is wavenumber. We consider three commonly used correlation functions, the Gaussian (GS), exponential (EX) and von Karman (VK) correlation function with the following expressions

for $C(r)$ and $P(k)$:

	$C(r)$	$P(k)$
GS	e^{-r^2}	$\frac{a_x a_z}{2} e^{-\frac{1}{4}k^2}$
EX	e^{-r}	$\frac{a_x a_z}{(1+k^2)^{\frac{3}{2}}}$
VK	$\frac{G_H(r)}{G_H(0)}$	$\frac{a_x a_z}{(1+k^2)^{H+1}}$.

(3.1)

where $G_H(r) = r^H K_H(r)$. In these expressions, H is the Hurst exponent, K_H is the modified Bessel function of the first kind (order H), and k_x, k_z are horizontal and vertical, wavenumbers, respectively. The characteristic scales are given by the correlation lengths in along-strike and down-dip direction, a_x, a_z, respectively, and $r = \sqrt{\frac{x^2}{a_x^2} + \frac{z^2}{a_z^2}}$, $k = \sqrt{a_x^2 k_x^2 + a_z^2 k_z^2}$. The Hurst exponent H in the expression for the von Karman ACF determines the spectral decay at high wavenumbers. For $H = 0.5$ the von Karman ACF is identical to the exponential ACF. For a fractal medium, the power spectrum is characterized by a power law decay. In the two-dimensional case, this can be written as [Voss, 1988]

$$P(k) \propto \frac{1}{k^{\beta+1}} \propto \frac{1}{(k_x^2 + k_z^2)^{4-D}}$$

(3.2)

where

$$D = E + 1 - H.$$

(3.3)

In (3.3), D is the fractal dimension, E the Euclidian dimension of the fractal medium, therefore $D = 3 - H$ for a two-dimensional fault plane. From (3.2) and (3.3) it follows that $\beta = 1 + 2H$; the "k-square" model therefore implies $H = 1$, or equivalently $D = 2$.

The differences among the random-field models in (3.1) are illustrated in Figure 3-2 for four slip realizations with identical phasing. The bottom panel displays the spectral decay as a one-dimensional slice (at $k_z = 0$) of the two-dimensional spectrum. While the Gaussian random field is smooth with little short-scale variation, the remaining distributions show considerable short-scale variability. The power spectral densities illustrate these differences, with a very rapid decay for the Gaussian model, but a more gradual decay for the exponential, von Karman and fractal models. The beginning of the roll-off of the power spectra
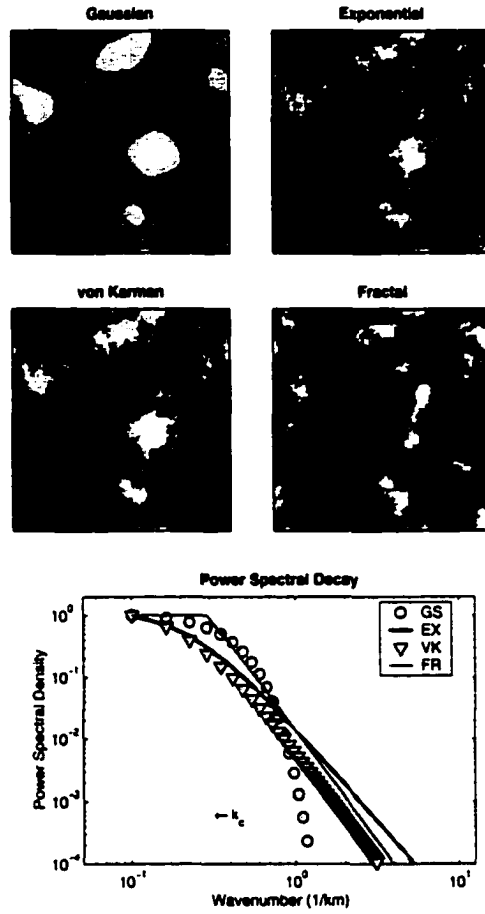
Figure 3-2: Examples of the spatial random field models considered in this study, generated with identical phasing to faciliate the comparison. Grid dimensions are 30×30 km, the correlation lengths are $a = 5$ km for the Gaussian, Exponential and von Karman autocorrelation function. For the von Karman model, $H = 0.8$, for the fractal case, $D = 2.2$ and $k_c = 0.3$. The bottom graph displays the corresponding power spectral decays of a one-dimensional slice (at $k_z = 0$) of the two-dimensional power spectrum $P(k)$.

is related to the correlation lengths for the Gaussian, exponential and von Karman ACF; for the fractal model, the PSD decays with a power law beyond a corner wavenumber, k_c, which is related to the characteristic source dimension.

3.4 Estimating Spectral Decay Parameters

To estimate the best-fitting correlation length for the Gaussian, exponential and von Karman correlation function, we use a grid-search algorithm that operates in the wavenumber domain by fitting power spectra for discrete values of correlation lengths a to measured spectral densities. The fractal dimension, D, can be estimated from a least-squares fit to the power spectral decay beyond the corner wavenumber.

We examine *average* decay properties of the slip spectra using the FACA-method (Fractal Analysis from Circular Average) [*Anguiano et al.*, 1994], before we analyze the spectral decay in along-strike and down-dip direction separately. In the FACA-method, the fractal dimension of a two-dimensional fractal image is estimated from integrated spectral values along a radial wavenumber, k_r, computed from the directional wavenumbers, k_x, k_z, and hence only represents *average* properties of the random field. We extend this approach to more general random fields, parametrized by the autocorrelation functions given in (3.1). This method eliminates possible anisotropy, but it yields more stable average estimates for the decay parameters, which provide a starting point for the subsequent two-dimensional analysis of the slip spectra. We then estimate the best-fitting correlation length a_x, a_z, in along-strike and down-dip direction, respectively, by iteratively sweeping through a large range of correlation lengths (from zero to the maximum source extent at a stepsize of $0.2\,\mathrm{km}$). This is done for each direction separately using the one-dimensional slice at $k_z = 0$ ($k_x = 0$) in along-strike (down-dip) direction of the two-dimensional PSD.

3.4.1 Sensitivity of Spectral Decay Parameters

Before we apply the grid-search algorithm to the inferred slip maps we test the method on simulated slip distributions. We generate test models on a square grid of $30 \times 30\,\mathrm{km}$ with sampling of $dx = dz = 0.5\,\mathrm{km}$, and input correlation lengths in the range of $5 \le a \le 20\,\mathrm{km}$. For the von Karman ACF, we fix the Hurst number to $H = 0.5$, since this allows to simultaneously evaluate the performance of the exponential ACF. For the fractal model, we consider fractal dimensions in the range $2 \le D \le 3$, where the lower limit characterizes the Euclidian dimension while the upper limit defines the "space-filling" (so called Peano) two-dimensional field.

To estimate the accuracy of the spectral decay parameters a_x, a_z, H and D, we apply the inversion to 20 slip realizations for each correlation length and fractal dimension. The
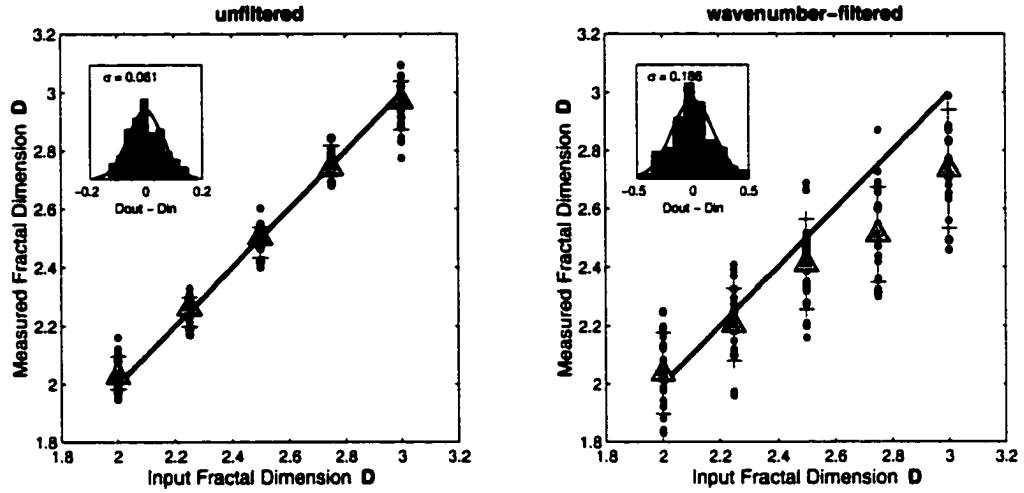
Figure 3-3: Distribution of measured fractal dimensions, D, versus the input fractal dimension for simulated slip distributions. The left panel shows the results for unfiltered slip maps, the right panel for wavenumber-filtered models for which the two-dimensional spectra were filtered at $0.2\,k_{ny}$, where k_{ny} is the Nyquist wavenumber of the simulated models. Stars indicate the actual measurements, the triangle marks the median, the crosses show the 1σ-bounds. The inset displays the cumulative distribution of all five populations (each with 20 realizations) with respect to each population's median, the solid curve depicts the fit to a normal distribution with standard deviation σ. The graphs indicate that the algorithm has difficulties recovering the fractal dimension for large D for the wavenumber-filtered models.

edges of these slip models are tapered to avoid unrealistically large displacements at the rupture boundaries; in a second step, we also low-pass filter the slip realizations to examine the effects that coarse spatial resolution and smoothing constraints in the slip inversion may have on the wavenumber spectrum and the resulting correlation length estimates.

Figure 3-3 shows that the inversion finds the fractal dimension for the unfiltered slip realizations very accurately, and that the standard deviation for each population is about equal; the deviation from each population's input fractal dimensions for all slip realizations jointly is only $\sigma = 0.06$. This changes for the wavenumber-filtered slip models ($k_f \leq 0.2\,k_{ny}$, where k_{ny} is the Nyquist wavenumber of the spatial grid). The cut-off wavenumber k_f was chosen to mimic the spatial resolution for slip models with an "average" grid-size of $dx \approx 3\,\mathrm{km}$ and with spatial smoothing applied in the inversion. Different choices of k_f change the D-estimates slightly, but don't affect our conclusions. The standard deviation for each population is larger, and for fractal dimensions $D \geq 2.5$ we underestimate the true value because the wavenumber filter removes the higher wavenumbers required to represent
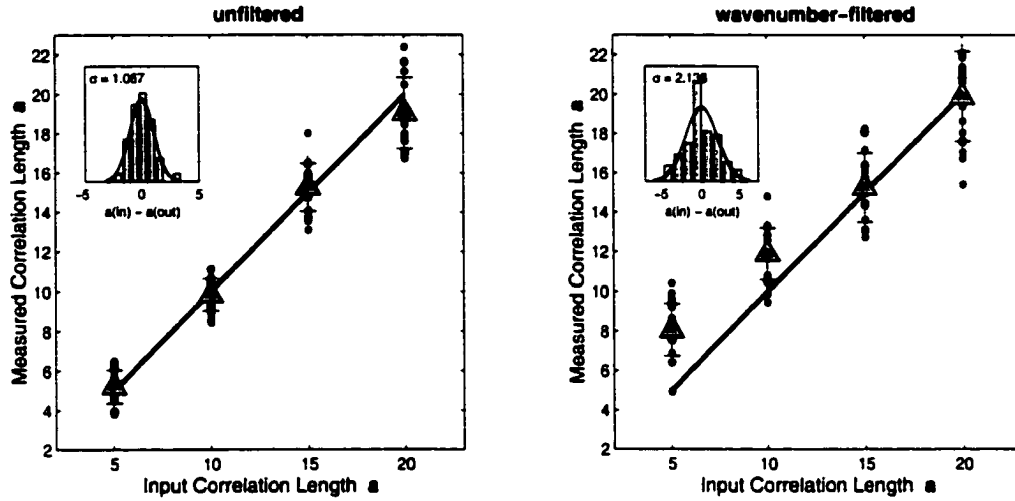
Figure 3-4: Same as Figure 3-3 for the correlation length of the von Karman autocorrelation function for 20 slip realizations. The graph on the right shows that, for short correlation length, the algorithm is biased high for the wavenumber-filtered slip models in which the high-wavenumbers (needed to represent short-scale variability) are most severely affected.

small-scale variability accurately. The standard deviation for all estimates of D jointly about each population's median is $\sigma = 0.19$. Based on these results we assume a D-dependent error for the estimated fractal dimension of inferred slip models, with $\sigma(D)$ increasing with D from $\sigma(D) = 0.1$ for $D \approx 2$ to $\sigma(D) = 0.25$ for $D \approx 3$.

In a similar manner we estimate the error in correlation length and Hurst exponent (Figures 3-4, 3-5, respectively.). For the unfiltered models the input values of a are accurately retrieved, with slightly increasing standard deviation for increasing correlation length a. The estimate for the Hurst exponent H is stable, with mean $\mu = 0.49$ and standard deviation $\sigma = 0.1$ for an input value $H = 0.5$. The effect of the high wavenumbers not being present in case of the filtered slip realizations can clearly be seen for short correlation lengths a that are consistently overestimated by 2.75 (or 55 %) for an input value of $a = 5\,\mathrm{km}$. For longer correlation lengths this effect decreases (though the spread within each population increases), and the error is on the order of ± 2.6 (or 13 %). We therefore assume an a-dependent error for estimated correlation lengths of inferred slip models that decreases from 60 % for short correlation lengths to 15 % for large a. In case of the Hurst exponent H we find that its median estimate of $\mu_H = 0.57$ for the filtered slip realizations is still close to the input value $H = 0.5$, indicating a slight bias towards higher values; the
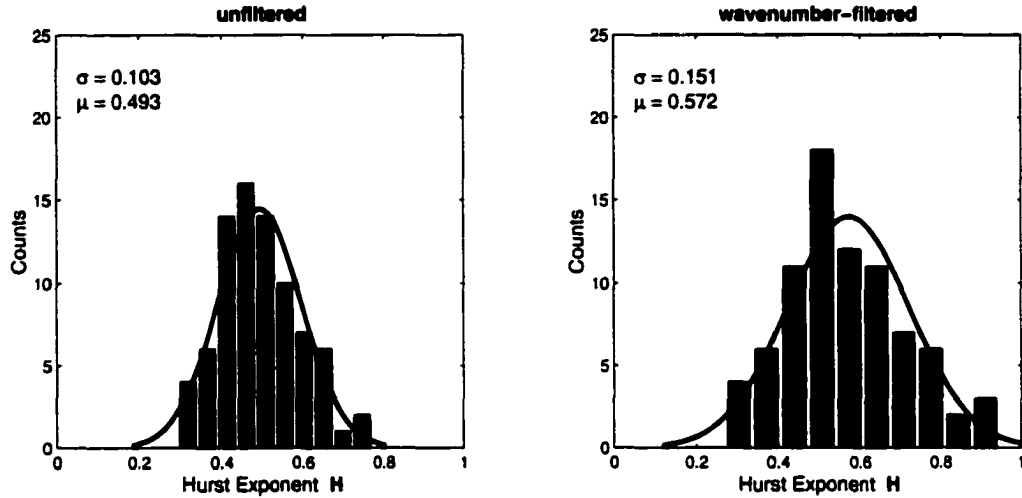
Figure 3-5: Distribution of measured Hurst exponents, H, for an input value of $H = 0.5$, for unfiltered simulated slip models (left) and wavenumber-filtered models (right). The solid line represents the fit of the measurements to a normal distribution with mean μ and standard deviation σ, given in the top-left corner.

standard deviation increased to $\sigma_H = 0.15$. We adopt this value as the standard deviation for the estimates of the Hurst exponent for the inferred slip models.

3.4.2 Application to Finite-Source Models

We estimate the spectral decay parameters of 44 finite-source slip models (Table 2.1) that span a magnitude range of $M_w = 5.9 - 8.0$ and comprise strike-slip and dip-slip earthquakes from various tectonic regimes. These slip models were derived using a number of inversion techniques and data sources (strong motion, teleseismic, geodetic, occasionally combined), different strategies to stabilize the inversion (regularization and smoothing constraints), and with spatial sampling as small as 0.5 km and as large as 10 km. In order to obtain a uniform wavenumber representation for all models and to facilitate the comparison among slip models, we bilinearly interpolate all models onto 1 × 1 km grid spacing such that the power spectral decays are directly comparable. We transform the interpolated models into the two-dimensional wavenumber domain using zero-padded grids of size 256 × 256 km such that each model has an equal number of data points for the inversion.

First we apply the FACA-algorithm to estimate the average spectral decay parameters of the slip maps. Figure 3-6 displays an example of this method, applied to the slip model for
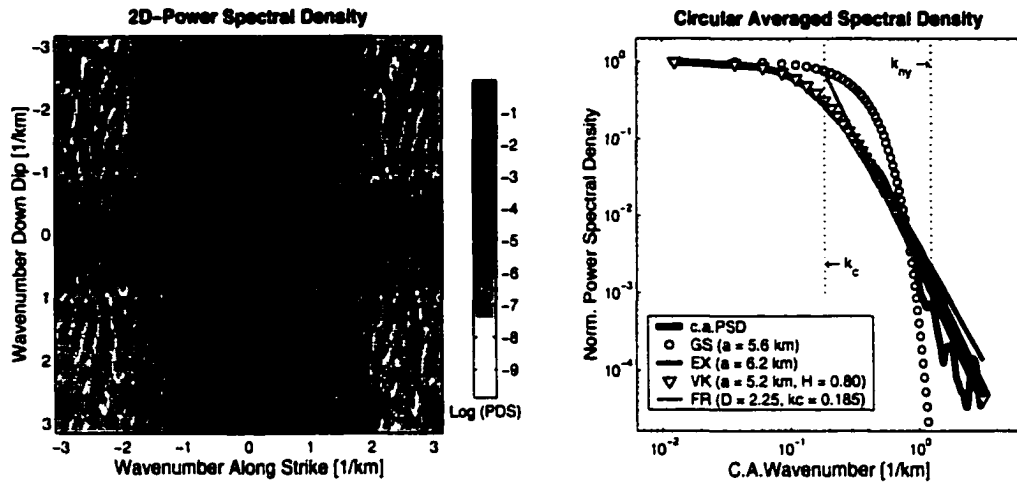
Figure 3-6: FACA-algorithm applied to the slip distribution of the 1979 Imperial Valley earthquake [*Archuleta*, 1984]. Vertical lines at k_c and k_{ny} indicate the band-width of the spectral fit. The Gaussian model can not fit the observed spectra; the fractal model requires a corner wavenumber, and cannot capture the gradual roll-off. Both, the exponential and von Karman ACF provide an excellent fit to the averaged slip spectrum.

the 1979 Imperial Valley earthquake [*Archuleta*, 1984]. We use the circular averaged PSD over the entire wavenumber range to estimate the averaged spectral decay parameters for the Gaussian, exponential and von Karman ACF, while the fractal dimension is computed from the power spectral decay beyond the corner wavenumber, k_c. The results shown in Figure 3-6 already exhibit some important properties: the Gaussian ACF is not a viable model to describe heterogeneous slip in earthquakes, but the exponential and von Karman ACF provide an accurate description of the spectral decay. Both models capture the gradual roll-off at low wavenumber as well as the high-wavenumber decay. The fractal model, on the other hand, is a bilinear model in log-log space (flat for $k < k_c$, linearly decaying for $k \geq k_c$), and does not capture the gradual roll-off of the observed spectrum.

To estimate the directional dependence of the spectral decay parameters, we apply the grid-search algorithm to one-dimensional slices in along-strike and down-dip direction of the two-dimensional PSD. Figure 3-7 displays the results for the 1979 Imperial Valley model for which slip was found to have occured in an horizontally extended zone at depth [*Archuleta*, 1984] (Figure 3-1). The inversion recovers this anisotropy with correlation length in along strike direction, a_x, being much larger than in down-dip direction, a_z, while the fractal dimension D is about equal in both directions. This illustrates that a single fractal dimension

may not be sufficient to model heterogenous slip distributions. Although the exponential and the von Karman ACF measure very similar correlation lengths (and hence RMS-misfits) for this particular example, we generally observe that the von Karman ACF returns slightly lower RMS-misfits than the exponential ACF due to the additional free parameter (Hurst exponent H) in fitting the spectral decay.

3.4.3 Resolution of Spectral Decay Parameters

Before we discuss the estimates of correlation length and fractal dimension for the slip distributions in Table 2.1, we want to point out that the slip-inversion process exerts a strong influence on these measurements, i.e. the lengths scales (asperity sizes) or fractal dimensions found in finite-source rupture models, using either the stochastic approach presented in this paper or a deterministic approach [*Somerville et al.*, 1999]. The results strongly depend on the limitations of finite-source inversion studies. In these inversions, the rupture plane is discretized into many subfaults where the size of the subfaults may depend on the rupture dimensions, on the availability, spatial distribution and frequency bandwidth of data, and the inversion method used. The frequency range of the data used in the inversion is band-limited to the low-frequencies, ranging from 0 Hz in geodetic inversions to a maximum of 4 Hz in inversions of strong motion data. These data limitations (in spatial distribution, frequency, and quality) leave any slip inversion with a component of the model that cannot be constrained by the data (the null space). Also, the resolution of the original models of slip may be anisotropic due to gridding or geometric effects. These factors taken together impose strong limitations on the range of spatial wavenumbers present in the published slip distributions.

We limit the largest wavenumber to be considered in the inversion to the Nyquist wavenumber, $k_{ny} = \pi/dx$, (dx is the spatial discretization in the fault-slip inversion). Since the spatial sampling in the slip inversion depends on the data type and their distribution, as well as the frequency range of seismic recordings, the limiting Nyquist wavenumber implicitly accounts for these factors in the spectral analysis. Table 3.1 lists k_{ny}, as well as the corner wavenumber k_c which is needed to determine the fractal dimension, D. The bandwidth of the spectral fitting ($0 \leq k \leq k_{ny}$ for the autocorrelation functions, $k_c \leq k \leq k_{ny}$ for the fractal model) is depicted in Figure 3-8 showing that k_c decreases for larger magnitudes (i.e. larger dimensions); k_{ny} exhibits a similar trend, though more erratic. The usable wavenumber range for the two largest earthquakes in our data set (No. 1, the 1923
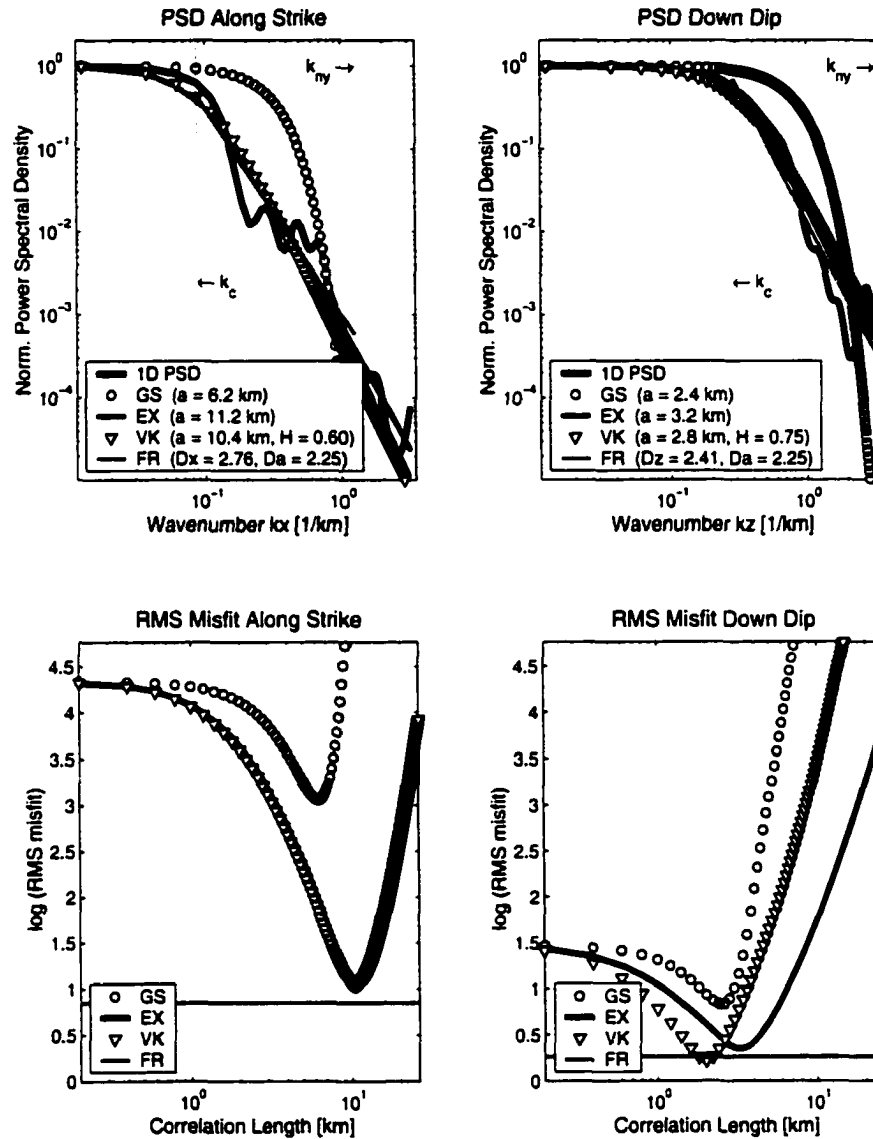
Figure 3-7: Fit of correlation functions to the power spectral decay of the slip distribution of the 1979 Imperial Valley earthquake [*Archuleta*, 1984]. Vertical lines at k_c and k_{ny} indicate the bandwidth of the spectral fit. Note the difference in the correlation lengths in along-strike and down-dip direction for the von Karman and the exponential ACF, reflecting the elongated nature of the area of large slip in this particular model (Figure 3-1).

Kanto earthquake, No. 11, the 1985 Michoacan earthquake) is extremely narrow, and hence the estimates of correlation length and fractal dimension for these events may not be very reliable.
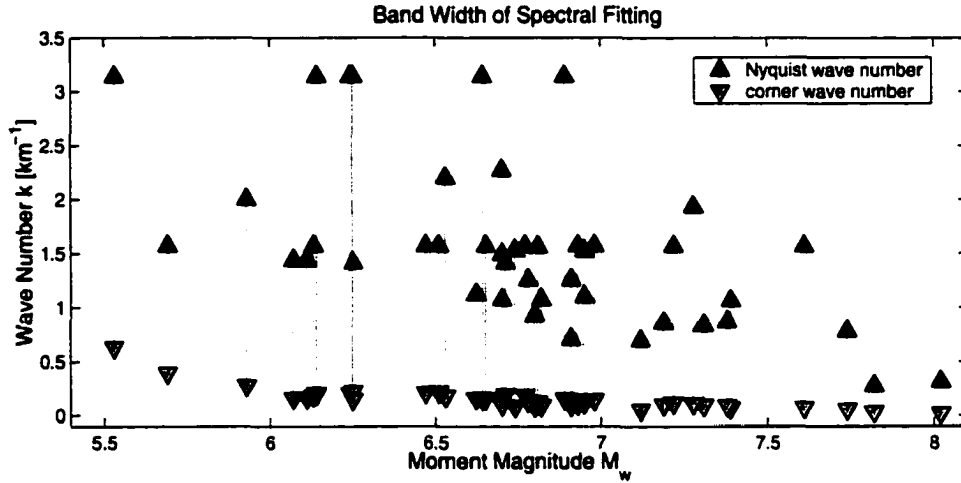
Figure 3-8: Approximate band-width of spectral fitting for all slip models in Table 2.1. The corner wave number k_c is obtained from the effective source dimension, the Nyquist wave number is computed from the spatial discretization dx used in the fault-slip inversion (listed in Table 3.1).

Finite-source inversions also include smoothing constraints to stabilize the inversion. The amount of smoothing, however, is often not a clear-cut objective choice, but rather a subjective one to avoid oscillatory slip maps. We explore this effect using a set of inversion results with different levels of smoothing, made available to us by *Sekiguchi et al.* [2000], who used Akaike's Bayesian information criterion (ABIC) [*Akaike*, 1980a] to determine the optimal amount of smoothing in the inversion. Here, the smoothing parameter λ is varied from less damping ($\lambda = 0.01$, data "overfitted", oscillatory/heterogenous solution) to more damping ($\lambda = 0.5$, data "underfitted", very smooth solution). Analyzing the six inversions for varying λ (Figure 3-9), we find that fractal dimension D decreases slightly with increasing λ, while the Hurst exponent H increases with increasing λ, demonstrating that more smoothing in the inversion results in faster spectral decay. The effect of λ on the estimates of D and H, however is small (less than 10 %). Figure 3-9 shows that the amount of smoothing had a stronger effect on the estimates of the correlation lengths, particularly in the along-strike direction in which a_x increases from ~ 16 km to ~ 24 km with increasing λ (a 50 % increase). The effect is smaller for the circular-average correlation length (~ 30 % increase), and negligible in the down-dip direction (~ 5 % increase).

Measurements of asperity size, characteristic scale lengths or spectral decay parameters,
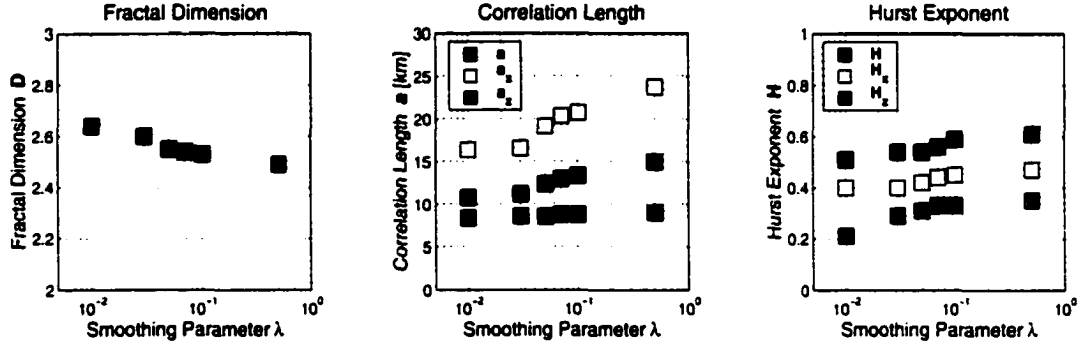
Figure 3-9: Estimates of fractal dimension D (left), correlation length a (center) and Hurst exponent H (right) for 6 slip inversions with variable damping, λ, for the 1995 Kobe earthquake [*Sekiguchi et al.*, 2000]. See text for details.

based on inferred finite-source models, are therefore only estimates of the true slip complexity during an earthquakes. Nevertheless, we believe that the characteristic scales we find from these slip models are likely to be representative of future earthquakes. In particular, since they are themselves derived from strong motion data, they can be used to simulate complex earthquake slip for strong motion prediction (Chapter 4).

3.5 Spectral Decay Parameters of Finite-Source Models

In the following we discuss the estimates of the spectral decay parameters (fractal dimension, D, Hurst exponent, H, and correlation lengths a, a_x and a_z) for 44 published finite-source rupture models (Table 2.1). The results are listed in Table 3.1 for each slip model, along with the *effective* source dimensions, L_{eff} and W_{eff} [*Mai and Beroza*, 2000]. We use these measurements to examine possible dependencies of the spectral decay parameters on source parameters (moment magnitude, M_w, fault length, L_{eff}, fault width, W_{eff}).

3.5.1 Fractal Dimension D

Although fractal dimension D and Hurst exponent H are related by (3.3), they are parameters of two different random-field models, determined by two different strategies. H is estimated within the grid-search algorithm, D is computed within the FACA-algorithm. We find, however, generally good correspondence between D and H estimates, approximately satisfying (3.3).

The estimates of fractal dimension D are shown in Figure 3-10, with 1σ-error bars $\sigma(D)$ as outlined above. The inset shows a quantile plot of all measurements, indicating that the values of D are normally distributed. We find no dependence of fractal dimension on moment magnitude or source dimensions, and there are no significant differences between strike-slip or dip-slip earthquakes. We find a median value of $D = 2.29$ (mean = 2.31, $\sigma_D = 0.23$). These values are also robust applying a boot-strapping technique. *t-test* statistics indicate that the median estimate for D is *not* significantly different from $D = 2$ at the 95 %-level, as proposed in the constant stress-drop model [*Andrews*, 1980b; *Herrero and Bernard*, 1994]. For $D = 2.29$, however, the slip spectrum decays less rapidly than for $D = 2$, and hence leads to more short-scale variability of slip than the "k-square"-model. Assuming that $D > 2$ is not an artifact of the fault-slip inversion method or the inversion for the spectral decay parameters, the observation that $D \geq 2$ has multiple possible interpretations: (1) non-constant stress drop for subevents in a cascade earthquake source model [*Frankel*, 1991]; (2) variability in rise time and/or rupture velocity is mapped into a more heterogeneous slip distribution [*Herrero and Bernard*, 1994]; (3) surfical geometrical complexity of fault systems extends to depth [*Okubo and Aki*, 1987; *Aviles et al.*, 1987].

For an earthquake source model consisting of a cascade of ruptures of different sizes the average stress drop over an area on the fault is assumed to be proportional to the standard deviation of the spatial variations in stress drop over that area [*Frankel*, 1991]. Then, the stress drop over some rupture zone with radius R will be $\Delta\sigma \propto R^\eta$ [*Frankel*, 1991]. For $\eta = 0$, stress drop is independent of scale length, and all subevents will have the same stress drop, independent of their size (magnitude). In contrast, $D > 2$ implies that $\eta < 0$ and hence stress drop $\Delta\sigma$ increases as the rupture size becomes smaller (smaller length scales). Although decreasing stress drop with increasing magnitude is *not* generally observed, it is in qualitative agreement with a study on strength of asperities [*Sammis et al.*, 1999].

An alternative interpretation for $D > 2$ is that it is an artifact that arises from finite-source inversion methods that do not accurately recover the true variability in rise time or rupture velocity. Although dynamic rupture modeling indicates that both rise time and rupture speed are spatially variable over the fault plane [*Day*, 1982], finite-source inversion often treat them as being constant or slowly varying. In order to fit the data, the inversion may therefore map variability in rise time or rupture velocity into a more heterogeneous slip distribution.

Independent evidence for $D > 2$ is found in studies on the geometrical complexity of
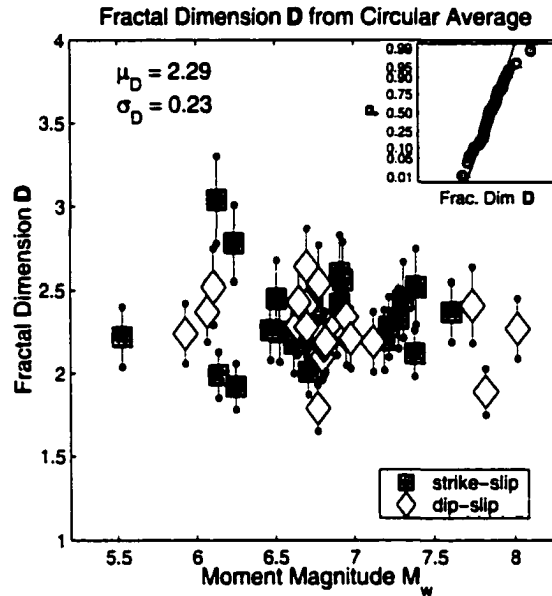
Figure 3-10: Fractal dimension, D, measured for 44 slip models given in Table 2.1. There is no evidence that D is related to magnitude or faulting style. The normal probability plot (inset) indicates that the measurements are normally distributed, with median $\mu = 2.29$ and standard deviation $\sigma = 0.23$.

fault systems [Okubo and Aki, 1987; Aviles et al., 1987]. In particular, Okubo and Aki [1987] find $D = 1.31 \pm 0.02$ for the mapped fault trace of the San Andreas Fault which translates into $D = 2.31$ for the fault surface using $D_{surface} = D_{trace} + 1$ [Okubo and Aki, 1987], consistent with our measurement of $D = 2.29$. In our opinion, the observation of $D > 2$ is probably attributable to a combination of incorrect mapping of rupture variability into the slip distribution as well as the geometric irregularity of the fault surface that is not accounted for in slip inversions. Whether the geometric complexities cause the rupture variability, or whether these are separate effects, remains to be addressed.

3.5.2 Hurst Exponent H

The inversion for spectral-decay parameters returns three estimates of the Hurst exponent for each earthquake (Figure 3-11), an estimate for the circular-averaged spectrum (H, left), for the along-strike (H_x, center) and for the down-dip direction (H_z, right). The median values μ and standard deviations σ (top right corner in each panel) for the three cases are close to each other, indicating that there is no strong directional dependence of H,

and that the Hurst exponent can be reliably estimated from the slip spectra. We find no evidence that the Hurst exponent depends on magnitude. It is interesting to note that the H-estimates are close to $H = 0.5$ for which the von Karman ACF is identical to the exponential ACF, explaining why both the exponential and the von Karman ACF provide similar fits to the observed spectral decay, and generally result in similar correlation length estimates for a given slip model (Table 3.1). he median estimates for H and D approximately satisfy, $D = 3 - H$, although they were derived using different approaches. $H \approx 0.75$ may again indicate that the constant stress drop model ($D = 2$, or equivalently, $H = 1$) [*Andrews*, 1980b; *Herrero and Bernard*, 1994] may not apply to the published slip maps. The observation that $H > 0.5$ becomes important when simulating slip distributions under the condition of finite static self-energy (Appendix B).

3.5.3 Correlation Lengths a

The correlation length estimates for the exponential and the von Karman ACF are listed in Table 3.1; the Gaussian ACF is not discussed further because it does not provide an adequate fit to the observed spectra. We will focus the following discussions on the correlation length estimates for the von Karman ACF because: (1) the Hurst exponents are found to be close to $H = 0.5$ for which the von Karman ACF is identical to the exponential ACF, leading to similar correlation lengths estimates for the two ACF's and our conclusions hold for either ACF; (2) we found that the von Karman ACF generally provides a better fit to the observed spectral decay than the exponential ACF or the fractal model, and we therefore adopt the von Karman ACF as our preferred model to describe complexity of earthquake slip.

The correlation lengths for all 44 slip models are listed in Table 3.1. It is interesting to note that the measurements of correlation lengths (but also D and H) show a remarkable consistency for those earthquakes for which multiple finite-source studies exist. Among the best studied earthquakes are the 1989 Loma Prieta earthquake (No. 20-23) and the 1995 Kobe event (No. 35-38), for which we have four slip models each. For Loma Prieta, for instance, D is about 2.23 with little scatter, and the (von Karman) estimates for a, a_x, a_z are 5.8 (± 0.4), 10.8 (± 1.2), and 3.8 (± 0.3), respectively. We obtain similar consistency in case of the Kobe earthquake for the fractal dimension ($D = 2.56 \pm 0.09$) and the correlation lengths ($a = 10.6 \pm 1.5$, $a_x = 20.1 \pm 2.0$, $a_z = 7.4 \pm 0.9$). The variation of the correlation length estimates among these models is only about 10 %. This is even more remarkable because these source models were derived using different data sources and inversion techniques, and

Table 3.1: Estimates of fractal dimension, D, correlation lengths, a, and Hurst exponents, H, for slip models listed in Table 2.1. Events marked with [†] cannot be fit with the van Karman ACF, but rather with a Gaussian ACF.

No.	L_{eff}	W_{eff}	k_c	$k_{n\nu}$	Fractal D	Exponential a	a_x	a_z	von Karman a	a_x	a_z	H	H_x	H_z
1	92.1	52.4	0.030	0.276	1.89	32.6	43.6	22.6	24.4	32.6	17.4	1.11	1.11	1.11
2	10.9	10.9	0.183	1.571	1.79	5.2	5.2	5.0	4.0	4.0	3.8	1.21	1.21	1.21
3	64.5	30.5	0.048	0.697	2.19	19.4	23.0	12.2	15.8	18.4	10.2	0.78	0.81	0.81
4[†]	5.0	5.2	0.392	1.571	1.50	1.8	1.8	1.8	1.2	1.2	1.2	1.50	1.50	1.50
5	23.5	7.5	0.175	2.199	2.25	6.2	11.2	3.2	5.2	10.4	2.8	0.80	0.60	0.75
6	25.4	8.6	0.156	1.112	2.18	6.6	10.8	3.8	5.4	9.0	3.4	0.82	0.81	0.86
7	21.7	6.3	0.206	1.571	2.26	4.6	7.2	2.6	3.8	6.6	2.2	0.78	0.66	1.02
8	32.6	20.1	0.080	0.927	2.10	11.4	13.8	9.2	9.0	10.8	7.4	0.90	0.90	0.90
9	20.3	6.6	0.201	3.142	2.78	5.0	9.8	3.0	6.4	12.6	3.0	0.22	0.21	0.48
10	14.1	8.9	0.183	1.571	3.04	5.2	6.6	4.0	7.2	10.6	4.8	0.10	0.00	0.26
11	134.9	96.8	0.018	0.314	2.27	50.0	57.4	38.6	41.4	42.2	34.8	0.74	0.92	0.64
12	21.7	10.1	0.145	1.492	2.64	6.2	7.2	4.8	6.0	7.8	5.0	0.52	0.50	0.46
13	24.2	11.6	0.128	1.257	2.54	6.6	7.8	4.8	6.6	6.8	5.4	0.50	0.70	0.34
14	15.9	10.2	0.161	1.439	2.52	5.8	7.0	4.6	5.0	6.4	3.8	0.82	0.68	0.89
15	14.9	10.9	0.159	1.439	2.37	5.2	6.4	4.6	4.8	5.6	3.8	0.62	0.77	0.80
16	7.6	6.9	0.275	2.001	2.24	3.2	3.6	3.0	2.8	3.2	3.4	0.76	0.70	1.15
17	16.2	6.3	0.219	1.414	1.92	4.8	7.2	2.8	3.8	5.6	2.2	1.08	1.08	1.08
18	17.0	7.6	0.190	1.414	2.01	5.4	7.4	3.6	4.0	8.4	2.8	0.99	0.32	0.99
19	13.2	7.2	0.215	1.571	2.45	4.2	5.6	3.0	4.2	6.0	2.6	0.48	0.41	0.86
20	25.3	9.0	0.151	3.142	2.29	6.6	10.0	4.0	5.6	10.0	3.4	0.74	0.50	0.71
21	24.4	10.6	0.135	1.524	2.23	7.2	10.8	4.2	6.2	10.0	3.8	0.70	0.59	0.75
22	31.3	12.1	0.115	1.100	2.34	8.2	13.4	5.2	6.4	11.6	4.6	0.88	0.70	0.70
23	26.3	9.5	0.143	1.571	2.21	6.8	11.4	4.0	6.0	9.8	3.8	0.68	0.72	0.62
24	3.3	3.1	0.630	3.142	2.22	1.2	1.2	1.0	0.8	1.0	1.0	0.78	0.78	0.78
25[†]	15.0	12.5	0.146	3.142	1.50	6.4	6.4	6.4	3.8	3.8	3.8	1.50	1.50	1.50
26	9.8	9.8	0.203	3.142	1.99	3.0	3.0	3.6	2.2	2.4	2.6	1.01	1.01	1.01
27	43.3	13.2	0.099	0.861	2.20	10.2	14.2	6.0	8.4	11.8	5.0	0.80	0.80	0.80
28	56.4	13.5	0.092	0.839	2.44	12.4	29.0	5.8	10.2	24.4	5.0	0.80	0.80	0.80
29	47.0	11.5	0.108	1.935	2.33	10.6	19.8	4.8	9.6	17.0	5.0	0.62	0.70	0.65
30	50.5	10.6	0.115	1.571	2.28	10.6	24.2	5.0	10.4	17.6	4.4	0.54	0.72	0.72
31	11.1	17.5	0.147	3.142	2.29	5.2	5.0	7.4	4.6	4.0	7.0	0.68	0.82	0.58
32	15.6	17.7	0.120	1.561	2.17	8.2	6.8	9.2	6.8	6.0	7.4	0.83	0.83	0.83
33	13.6	14.8	0.141	2.271	2.41	6.6	6.6	7.0	5.2	5.6	5.8	0.84	0.82	0.82
34	11.6	14.2	0.156	1.571	2.43	5.6	4.8	6.0	5.2	4.2	4.8	0.66	0.73	0.86
35	47.9	17.1	0.079	1.530	2.40	12.8	17.6	7.4	11.6	19.2	7.0	0.62	0.40	0.58
36	38.1	15.5	0.091	1.257	2.42	11.6	15.6	7.2	10.6	17.0	8.6	0.62	0.43	0.22
37	39.4	13.6	0.099	0.707	2.60	10.0	17.2	5.8	9.6	16.8	5.4	0.61	0.56	0.72
38	35.6	13.7	0.101	1.571	2.56	9.2	13.2	5.8	10.8	18.0	6.2	0.33	0.22	0.35
39	21.6	23.6	0.088	1.074	2.19	10.0	9.2	10.6	8.2	7.4	9.0	0.81	0.87	0.82
40	21.1	21.1	0.095	1.074	2.28	10.0	10.6	10.6	7.6	8.6	9.8	1.02	0.82	0.65
41	95.5	16.4	0.071	1.571	2.37	18.8	34.8	6.8	16.8	31.2	6.4	0.63	0.63	0.60
42	83.6	18.4	0.066	1.065	2.52	17.2	33.0	7.8	17.6	33.8	7.4	0.47	0.47	0.59
43	57.3	14.3	0.088	0.873	2.12	13.4	24.4	6.0	10.6	18.4	4.8	0.84	0.91	0.94
44	53.0	26.6	0.056	0.785	2.41	15.8	22.0	10.2	14.4	19.8	9.4	0.64	0.66	0.62

to some extent the resulting slip distributions are dissimilar. In contrast, the correlation length estimates for the 1992 Landers earthquake (No. 27-30) differ by about a factor of
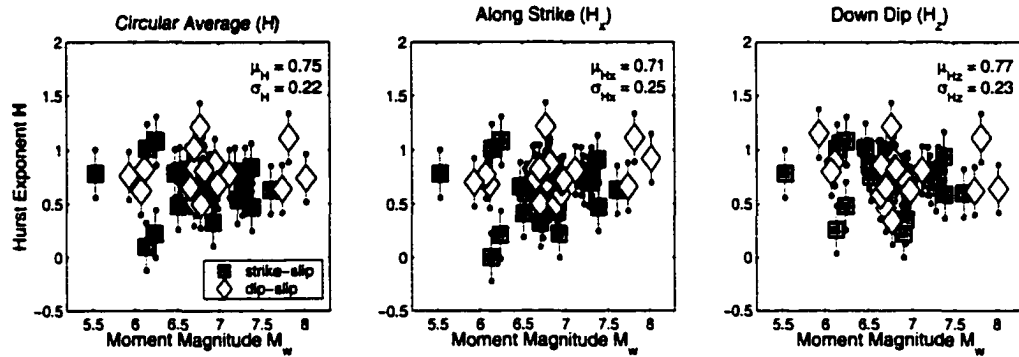
Figure 3-11: Hurst exponent, H, measured for 44 slip models listed in Table 2.1. We find no evidence that H is related to magnitude or faulting style. The distribution in each panel is normal, with median (μ) and standard deviations (σ), given in the top-right corner.

two in the along-strike direction, reflecting the more localized slip in the models by *Cohee and Beroza* [1994] and *Wald and Heaton* [1994], compared to the solutions by *Cotton and Campillo* [1995] and *Zeng et al.* [2000]. Generally, the statistical properties of earthquakes with multiple finite-source slip models seem to be recovered in a consistent manner, and the random-field model we propose is able to capture this similarity.

The correlation lengths we obtain are also similar to the asperity dimensions found be *Somerville et al.* [1999]. While we have estimated *stochastic* properties of a slip distribution, their measurements are *deterministic*, and hence the two sets of measurements are not necessarily directly comparable. We find, however, that for slip models with multiple, small asperities [*Somerville et al.*, 1999], we obtain short correlation lengths and low Hurst exponents. Likewise, where *Somerville et al.* [1999] find only one or two larger slip patches, we observe longer correlation lengths and larger Hurst exponents. In the deterministic model, the asperity size increases with source dimension (magnitude) [*Somerville et al.*, 1999], an observation that is confirmed by our measurements in that larger earthquakes tend to have longer correlation lengths. We therefore conclude that the "characteristic length scales" measured in this study agree qualitatively with those by *Somerville et al.* [1999], though ours is a *stochastic* representation of slip complexity, whereas theirs is a *deterministic* one.

Table 3.2: Coefficients for the scaling of correlation lengths a for the *von Karman* autocorrelation function with source parameters.

Equation	FM	slope (error) $b_1 (\sigma_{b_1})$	intercept (error) $b_0 (\sigma_{b_0})$	standard deviation σ	correlation coefficient r^2
Circular Average					
$\log(a) = b_0 + b_1 M_w$	SS	0.47 (0.06)	-2.32 (0.37)	0.15	0.77
	DS	0.47 (0.06)	-2.32 (0.40)	0.14	0.77
	AL	0.46 (0.04)	-2.30 (0.26)	0.14	0.77
$a = b_0 + b_1 L$	SS	0.19 (0.01)	1.73 (0.57)	1.55	0.90
	DS	0.28 (0.02)	0.51 (0.82)	2.59	0.93
	AL	0.24 (0.02)	0.74 (0.63)	2.65	0.87
$a = b_0 + b_1 W$	SS	0.94 (0.13)	-2.12 (1.53)	2.61	0.71
	DS	0.43 (0.03)	0.65 (0.93)	2.92	0.98
	AL	0.42 (0.04)	2.24 (0.75)	3.41	0.78
Along Strike					
$\log(a) = b_0 + b_1 M_w$	SS	0.60 (0.08)	-2.95 (0.54)	0.21	0.72
	DS	0.47 (0.07)	-2.27 (0.46)	0.15	0.73
	AL	0.52 (0.06)	-2.51 (0.39)	0.20	0.67
$a = b_0 + b_1 L$	SS	0.33 (0.03)	3.61 (1.39)	3.81	0.82
	DS	0.36 (0.01)	0.61 (0.57)	1.79	0.98
	AL	0.35 (0.02)	1.99 (0.75)	3.14	0.90
$a = b_0 + b_1 W$	SS	1.60 (0.29)	-2.57 (3.30)	5.64	0.60
	DS	0.53 (0.04)	1.19 (1.23)	3.89	0.89
	AL	0.48 (0.07)	5.99 (1.53)	6.99	0.52
Down Dip					
$\log(a) = b_0 + b_1 M_w$	SS	0.30 (0.53)	-1.35 (0.36)	0.14	0.60
	DS	0.34 (0.08)	-1.53 (0.53)	0.18	0.52
	AL	0.34 (0.05)	-1.55 (0.33)	0.17	0.54
$a = b_0 + b_1 L$	SS	0.06 (0.01)	2.76 (0.52)	1.44	0.53
	DS	0.21 (0.02)	1.33 (0.97)	3.05	0.83
	AL	0.15 (0.02)	1.46 (0.85)	3.58	0.57
$a = b_0 + b_1 W$	SS	0.45 (0.04)	-0.06 (0.42)	0.72	0.88
	DS	0.36 (0.01)	0.74 (0.25)	0.80	0.99
	AL	0.36 (0.01)	0.86 (0.18)	0.81	0.98

3.5.4 Scaling of Correlation Lengths with Source Dimensions

A careful analysis of the correlation lengths in Table 3.1 suggests that a, a_x, and a_z depend on source dimension. This is manifest in Figure 3-12, which displays the measured correlation lengths for all slip models in Table 3.1 with respect to *effective* fault length L_{eff} (top) and fault width W_{eff} (bottom). Error bars are computed based on the sensitivity tests for random slip models (see earlier section). The graphs demonstrate that the circular-averaged, along-strike and down-dip correlation lengths increase with source size.
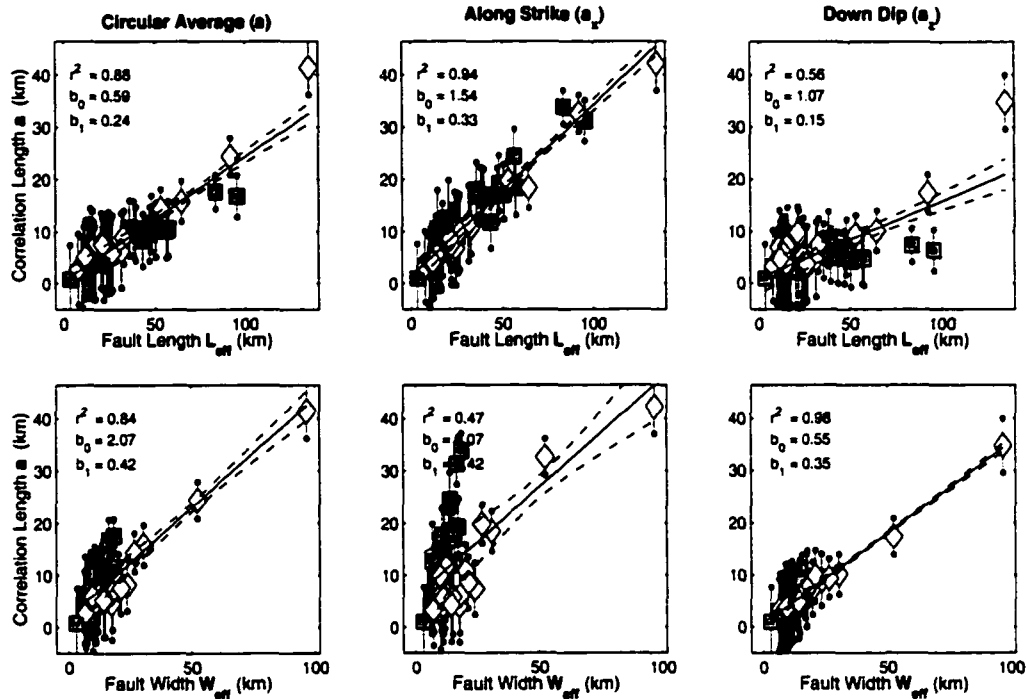
Figure 3-12: Measured correlation length, a, versus effective fault length, L_{eff} (top row) and fault width, W_{eff} (bottom row). The effective source dimensions are given in Table 3.1 [*Mai and Beroza*, 2000]. There is clear evidence that the correlation length a increases with increasing source dimensions. The graphs also show regression curves (solid lines; broken lines indicate 95% confidence limits) with intercept b_0, slope b_1 and correlation coefficient r^2 (top-left corner). Regression coefficients for strike-slip and dip-slip earthquakes considered separately are listed in Table 3.2.

The linear regression curves of correlation lengths on source dimension show this dependence with most correlation coefficients of $r^2 > 0.80$. The down-dip correlation lengths a_z depend only mildly on fault length ($r^2 = 0.56$), likewise for the dependence of the along-strike correlation lengths a_x with fault width ($r^2 = 0.47$). The regression coefficients for the intercept (b_0) and the slope (b_1) are given in the upper left corner; Table 3.1 lists faulting-style dependent coefficients.

The regression of a_x on fault length L_{eff} and a_z on fault width W_{eff} can be used to establish simple scaling relations between these source parameters, which in turn are useful to estimate the correlation length for future earthquakes. The results shown in Figure 3-12
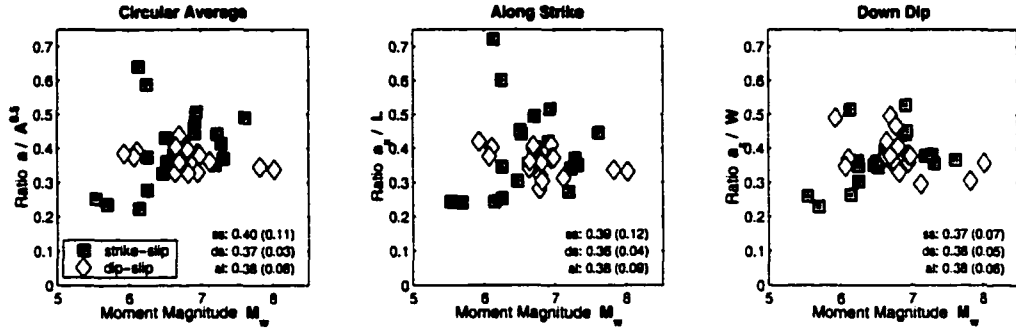
Figure 3-13: Ratio of correlation lengths and effective source dimensions, $a/\sqrt{A_{eff}}$ (left), a_x/L_{eff} (center) and a_z/W_{eff} (right), with the *medians (st.dev.)* given for the different faulting styles (ss – strike-slip; ds– dip-slip; al – all mechanisms). The ratios are independent of magnitude, and tend to be in the narrow range of 0.25 to 0.6; on average, the correlation lengths are 40% of the characteristic source dimension.

and Table 3.2 suggest a simplified scaling as

$$a_x \approx 2.0 + \tfrac{1}{3} L_{eff}$$

$$a_z \approx 1.0 + \tfrac{1}{3} W_{eff}$$

(3.4)

in which the slope of $b_1 = \tfrac{1}{3}$ in (3.4) indicates that correlation lengths scale linearly with effective source dimension. For earthquakes with small aspect ratio L_{eff}/W_{eff}, (3.4) yields roughly isotropic correlation lengths, while for earthquakes with large aspect ratios (i.e. great strike-slip earthquakes) the correlation length along-strike is larger. Equation (3.4) also implies that the ratio $a_x/L_{eff} \approx 1/3$, which is represented in Figure 3-13. For dip-slip earthquakes, this ratio remains constant over the given magnitude range, while for strike-slip earthquakes the ratio increases with increasing magnitude, with a_z/W_{eff} perhaps saturating at $M_w \approx 7$. For all three cases (circular-averaged, along-strike and down-dip), the ratio is 0.38 ($\pm$ 0.09), varying in the narrow range of 0.25 to 0.6.

Figure 3-14 shows log(a) versus moment magnitude, M_w, again overlain by least-squares regression curves. In the case of the circular-average a and the along-strike a_x, the slope of the regression is about 0.5, indicating that the correlation length increases with magnitude in a self-similar fashion. Although the estimates in down-dip direction deviate from this apparent self-similarity, we hypothesize a simplified relation between the correlation length
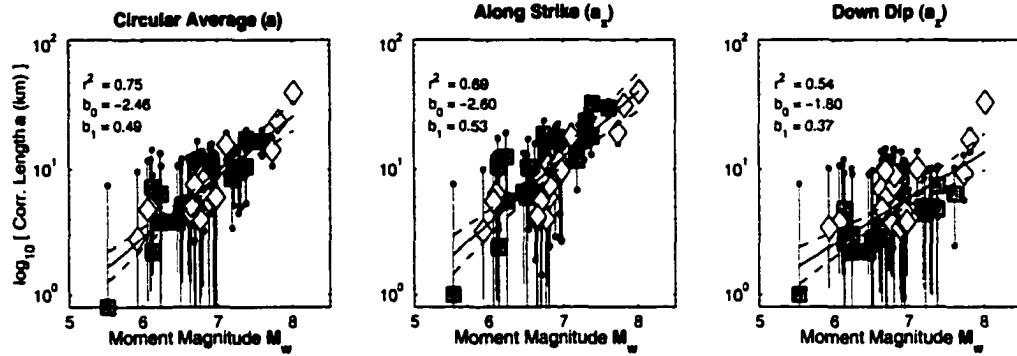
Figure 3-14: Measured correlation length, a, versus moment magnitude, M_w, for 44 slip models listed in Table 2.1; filled squares denote strike-slip earthquakes, open diamonds represent dip-slip events. The slope of the regression curves (solid lines) is $b_1 \approx 0.5$, an indication that correlation lengths scales with moment magnitude in a self-similar manner. Table 3.2 lists the regression coefficients if strike-slip and dip-slip earthquakes are considered separately.

and moment magnitude (Table 3.2) as

$$\log(a_g) \approx -2.5 + \tfrac{1}{2} M_w$$

$$\log(a_z) \approx -1.5 + \tfrac{1}{3} M_w$$

$$(3.5)$$

where a_g is either circular-average or along-strike correlation length. The relations in (3.5) are very similar to results of a recent study in which the characteristic subevent size Δl was estimated based on source-parameter modeling [Beresnev and Atkinson, 2001]. They find that Δl scales with magnitude as

$$\log(\Delta l) = -2 + 0.4 M_w,$$

$$(3.6)$$

and reanalyzing the catalog of events of Somerville et al. [1999] they find

$$\log(\Delta l) = -2 + 0.5 M_w,$$

$$(3.7)$$

interpreting Δl as the asperity size. The simple linear scaling presented in eqs. (3.5), (3.6) and (3.7) for the correlation length, subfault size and asperity size, respectively, suggest a fundamental property of extended-source earthquake models, namely that the characteristic length scales with earthquake magnitude. This property can be used to estimate the

characteristics of hypothetical future earthquakes, but it also may be interpreted in terms of the rupture physics.

3.6 Discussion

In this section we address the question how well the fractal dimension D may be resolved from inversion of near-source strong motion data, and what effect variable D has on synthetic seismograms. We propose what additional data may be useful to constrain the fractal dimension or correlation lengths of earthquake slip, and we discuss the implications of our results for dynamic rupture propagation.

3.6.1 Data-Dependence of D-estimates

The fractal dimension we have obtained from analysis of finite-source models is subject to several sources of uncertainty. We are encouraged that our results are meaningful because we find that fractal dimension D or correlation length a (Table 3.1) are very consistent for independently derived models of the same earthquake. The spatial discretization of the source models is potentially important, but Figure 3-8 and Figure 3-10, suggest that it exerts only a minor influence on the estimate of D, i.e. the fractal dimension does not depend significantly on the grid size. Earthquakes with $M_w \geq 7$ generally have a lower Nyquist wave number (k_{ny}), yet their D-estimates agree with the general observation, $D > 2$. Only for the 1923 Kanto earthquake (No. 1) do we find a considerably smaller fractal dimension ($D = 1.89$), This may be attributable to the very sparse data for this event.

In contrast, we observe a significant influence of the type of data used in the fault-slip inversion. Inversions of only geodetic data result in rather low estimates of D (events No. 17, 18, 25, 32). Likewise, models derived from teleseismic data alone have fractal dimension that is somewhat below the average D (events No. 39, 40, 43). Using or incorporating strong motion data in the slip inversion, on the other hand, results in a larger degree of spatial complexity (i.e. higher D). This is attributable to the sensitivity of near-source strong motion recordings to the details of the rupture process.

To investigate the effect that variable D excerts on near-source seismograms, we generate four slip models ($M_w = 7$, source dimensions $15 \times 40\,\mathrm{km}$) with varying fractal dimension, but identical phase, such that asperities are located in the same regions (Figure 3-15, left column). Using the same hypocenter, average rupture velocity, rise time and slip-velocity
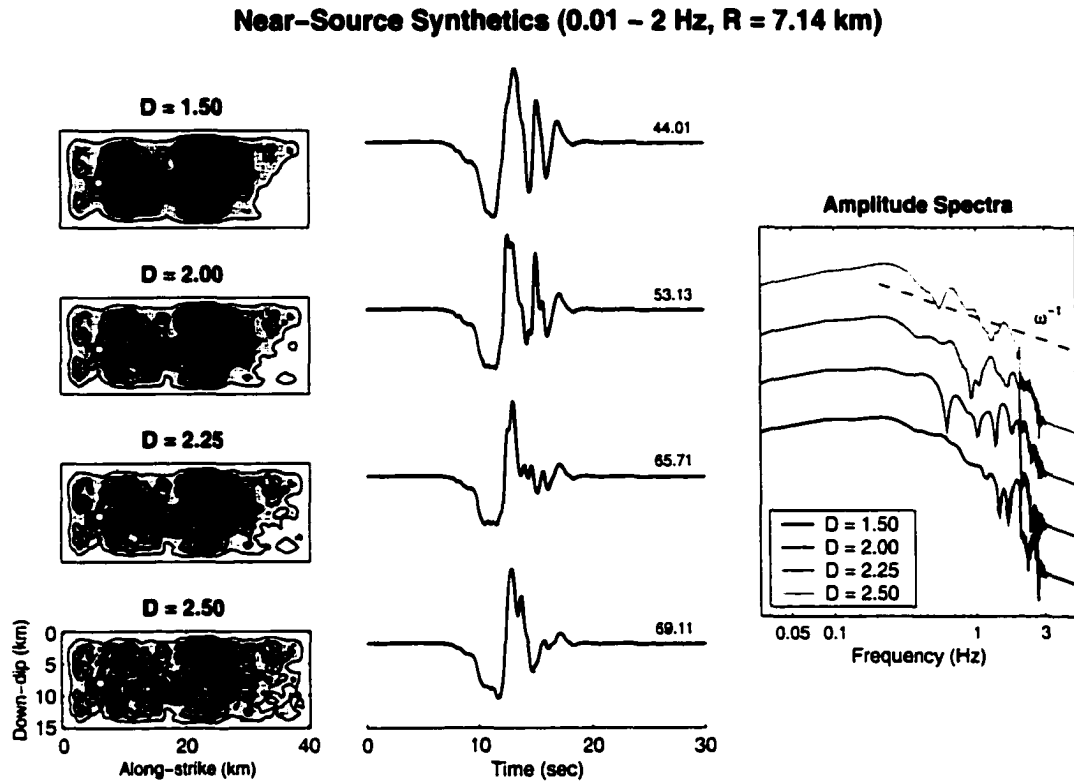
Figure 3-15: (center) Near-source synthetic seismograms (fault-parallel component, bandpassed at 0.01 – 2 Hz) for phase-identical slip distributions with variable fractal dimension, D (left). The hypocenter is indicated by a star. Note how the variation in D is reflected in the waveforms and the corresponding peak-ground velocities. The velocity spectra (right, vertically shifted) display only minor differences, and their decay ($\propto \omega^{-1}$) is consistent with observed flat acceleration spectra.

function, we calculate synthetic seismograms on a grid of 36 locations. The seismograms in Figure 3-15 display waveforms for an observer located at $x = 45$ km along-strike (fault length is 40 km) at a distance of 5 km in the fault-normal direction. We bandpassed the seismograms from 0.01 – 2 Hz, to reflect the bandwidth of seismic data used in strong motion inversion.

As the waveforms in Figure 3-15 indicate, increasing fractal dimension (i.e. more short-scale variability) results in more complex wavetrains, while their low-frequency character remains similar. The differences in these waveforms and their peak-velocities are large enough to matter in slip inversions using near-source recordings, and estimated slip distributions for well recorded earthquakes should reflect these differences. We also observe that

velocity spectra (vertically shifted in Figure 3-15, right column) exhibit differences for all four fractal dimensions, but their frequency decay ($\propto \omega^{-1}$) remains unchanged for variable D, consistent with the generall observation of flat acceleration spectra.

3.6.2   Additional Data to Constrain Slip Complexity

It may also be possible to measure fractal dimension D and correlation lengths a, a_x, a_z of earthquake slip distributions indirectly. Limitations in resolution and accuracy of slip inversions limit the accuracy of the measured fractal dimension and correlation length, particularly at high wavenumbers. There are several others kinds of data that might also constrain the nature of earthquake slip complexity.

Perhaps the most intuitive source of data are measuremements of surface slip for large earthquakes. These one-dimensional surface-slip distributions could be analyzed both deterministically (i.e. correlating large surface slip with slip at depth) and stochastically (i.e. measuring correlation length), and hence could provide additional insight into earthquake source complexity. The disadvantages of such surface-slip measurements are, however, their highly irregular spatial sampling, their large uncertainties [*Hough et al.*, 2000], and the fact that such data only exist for very few, large earthquakes. We suspect, therefore, such data may be only of limited use to study earthquake source complexity.

Analyzing the spatial distribution of micro-seismicity is another possible approach for studying the spatial complexity of earthquake slip and stress. The spatial distribution of a-values and b-values, as imaged by *Wiemer and Katsumata* [1999], for example, could help to illuminate the spatial complexity of stress drop [*Frankel*, 1991]. Of course, micro-earthquake locations are also subject to uncertainties, so it would be most useful to work with a catalog of high-precision earthquake locations [e.g. *Schaff et al.*, 2001], Such data are only available in very well-instrumented regions (e.g. California, Japan, Taiwan), but could potentially help to constrain earthquake source complexity, particularly in terms of the geometric fault plane complexities.

3.6.3   Implications of Correlation Lengths for Rupture Dynamics

Uniform correlation lengths for all magnitudes would lead to problems in accomodating the slip (seismic moment) present in large earthquakes. If correlation lengths were constant, a large earthquake would be comprised of many small, localized zones in which almost all

the moment has to be released. These areas would have very large stress drops, yet would have to rupture in isolation from the surrounding high-slip areas in order to maintain short correlation lengths. It would be difficult to support such behavior from a rupture-dynamics view point where neighboring points of the fault interact strongly with each other, and hence are unlikely to allow isolated rupture zones of large stress drops. These arguments lead us to believe that the increasing correlation length for larger earthquakes is not an artifact due to the fault-slip inversions (due to coarser fault discretization and longer periods for larger earthquakes), but rather a real property of the earthquake source.

One could argue that the observed correlation length scaling is merely determined by the overall extent of the source (geometry), and that at smaller length scales the slip function is purely self-affine (fractal) with a fractal dimension D arising from scale-independent rupture dynamics. We take an alternative view that the correlation length of the two-dimensional slip distribution of an earthquake is governed by length scales in the rupture process other than the overall source extent and that these may not be purely fractal. An earthquake will contain length scales spanning many orders of magnitudes, from the grain-size scale to total fault length. Length scales of juxtaposed rock units are on the order of $10^2 - 10^5$ m [*Warner et al.*, 1994; *Holliger and Levander*, 1992]. Geometric irregularities (fault bends, jogs, offsets) occur at lengths scales of $10^2 - 10^4$ m and smaller. These 'static' length scales will affect the characteristic lengths during an earthquake.

The dynamics of earthquake rupture will also affect the correlation distances of the final slip distribution. If an earthquake encounters a strong asperity early in the rupture, the seismic load [*Andrews*, 1985] may not be sufficiently large to break the asperity, and the rupture is arrested early, resulting in a small earthquake with a short correlation distance. If the earthquake manages to break that asperity, its size and moment would grow, and the rupture would have a large area of slip. This scenario would result in a longer correlation distance for a somewhat bigger earthquake. Similarly, late into the rupture (when the seismic load is larger), stress drops may become large locally, and the rupture may become more difficult to stop and hence run to longer distances with significant slip, effectively increasing the correlation length of the final slip for large earthquakes.

3.7 Conclusions

We have developed an approach to characterize spatial complexity of earthquake slip imaged in finite-source rupture inversions. The characterization of slip heterogeneity as a spatial random field successfully captures the observed gradual roll-off of the wavenumber spectra as well as the directional dependence of the correlation lengths. In the case of slip being fractal, we find no indication that the fractal dimension, D, depends on other source parameters, and we conclude that D is independent of seismic moment. For the fractal model, however, the corner wavenumber k_c (representing an "outer scale length") decreases with increasing source dimension. In contrast to the constant stress-drop model ($D = 2$), the observation $D > 2$ may imply: size-dependent stress drop for subevents within an, earthquake incorrect mapping of varibility in rupture speed and/or rise time into a more heterogeneous slip distribution, or extension of geometric fault trace complexity to depth.

The correlation lengths a, a_x and a_z for the von Karman ACF depend on earthquake source parameters. Independent studies [*Somerville et al.*, 1999; *Beresnev and Atkinson*, 2001] are consistent with the increase of characteristic scale lengths with increasing magnitude that we have found. Simplified scaling relations imply that correlation lengths scale linearly with source dimension, in agreement with [*Beresnev and Atkinson*, 2001].

The spatial random field model for earthquake slip can be used to generate scenario earthquakes for strong motion prediction. We calculate the source dimensions using scaling relations [e.g. *Mai and Beroza*, 2000], and generate spatially variable slip distributions using the spectral synthesis method [*Pardo-Igúzquiza and Chica-Olmo*, 1993]. Each realization of heterogeneous earthquake slip, however, is subject to the condition that the static strain energy associated with the slip distribution remains finite (Appendix). This condition ensures that stresses cannot become infinite (though locally they may become very large). Strong motion synthetics computed from these simulated slip distributions, assuming simple kinematic rupture parameters (constant rupture velocity, constant rise time, boxcar source time function) show the utility of the model for strong motion prediction [*Mai and Beroza*, 1999]. Sofar, we have considered only heterogeneity in earthquake slip. Future work will address the question of how to obtain physically realistic distributions of rise time and rupture velocity, based on simulated slip (stress) distributions [*Guatteri et al.*, 2001].

3.8 Acknowledgments

Chapter 4

A Hybrid Method for Calculating Near-Source, Broadband Seismograms: Application to Strong Motion Prediction

4.1 Abstract

We present a hybrid method to compute broadband strong motion seismograms in the near-field of large earthquakes. We combine complete seismograms at low-frequency with ray theory seismograms at high frequency to form a composite broadband seismogram that spans the entire frequency range of interest. Our approach reconciles the amplitude spectra of the two sets of synthetic seismograms at intermediate frequencies where their domain of validity overlaps.

We demonstrate the method with scenario earthquakes based on the spatial random-field model for complex earthquake slip [*Mai and Beroza*, 2001a]. The hybrid near-source, broadband seismograms are useful both for detailed source modeling and for incorporating source effects into probabilistic seismic hazard analysis.

4.2 Introduction

Prediction of strong ground motion in future earthquakes is the central challenge of engineering seismology. Attenuation relations have long been used to predict the behavior of simple characterizations of ground motion intensity (such as peak ground acceleration or spectral ordinates for given frequency and damping) as a function of earthquake size and

distance. Although the recent large earthquakes in Taiwan and Turkey have added important new observations, there remains a scarcity of strong motion data in the extreme near field of large earthquakes on which to base strong ground motion attenuation relations.

Several factors cause the ground motion to be qualitatively different in the extreme near-field than at somewhat larger distances. Directivity effects are likely to be most pronounced close in to large earthquakes, leading to the possibility of large pulses of short duration, particularly in the forward direction of rupture propagation. These directivity effects were only recently included into strong motion attenuation laws [*Somerville et al.*, 1997]. In this near-field regime, the rise time will also have a strong effect on strong ground motion, and near-fault stations may experience large permanent displacements. All of these factors will act to make near-field ground motion for a particular intensity (e.g., PGA) substantially different from ground motion of the same intensity, observed at greater distances from the fault.

Moreover, as structural engineers face the challenges presented by performance-based engineering, it will become increasingly important to model structures as non-linear multi-degree-of-freedom systems. To analyze such behavior it is important to use the entire time series of strong ground motion, rather than some simplified intensity measure. Until we have more plentiful recordings of strong ground motion, simulation will have to play a central role in predicting the level and variability of strong ground motion due to source effects in the near-field of large earthquakes.

Current methods for broadband strong motion simulation combine deterministic low-frequency waveforms with stochastic high-frequency synthetics seismograms [*Saikia and Somerville*, 1997]. This technique yields strong motion seismograms that cover the frequency range of engineering interest. Such modeling also reproduces the widely observed ω^{-2} spectral decay for far-field displacement seismograms. It has been noted, however, that the resulting response spectra show unusual behavior at frequencies where the deterministic signal ends and the stochastic signal begins (*Cornell, personal communication*). The likely explanation for this observation is that while the amplitude spectrum of the two signals is easily matched, the phase spectrum is not. This mismatch of the phase may cause unusual behavior near the matching frequency, which is in the center of the frequency band of engineering interest.

In this paper, we take a different approach to generate broadband strong motion seismograms, using simulated earthquake source models for which we compute complete low-frequency near-field ground motions as well as approximate high-frequency ground motions. We combine these synthetic seismograms in the frequency domain to form a composite broadband strong motion signal that contains exact low-frequency near-field terms and approximate high-frequency contributions. The proposed method avoids the difficulties associated with reconciling deterministic low-frequency synthetics with stochastic high-frequency simulations. We generate extended-source rupture models based on the random-field model for complex earthquake slip [*Mai and Beroza*, 2001a](Chapter 3). In this model, earthquake slip is characterized as a random-field with an autocorrelation function whose correlation lengths depend earthquake magnitude, and allows to simulate earthquake rupture with non-isotropic correlation length (i.e. elongated "asperities" of large displacement) and source variability down to very short scale length.

Previously, *Berge et al.* [1998] have introduced a time-domain method to calculate near-source strong motion synthetics (based on the k^2-model by *Herrero and Bernard* [1994]) that requires the computation of three band-limited seismograms to form one broadband composite seismogram. The advantage of the method presented in this paper is that seismograms are combined in the frequency domain, and only two band-limited strong motion seismograms are required to form the broadband composite seismogram. Aside from their importance for strong motion prediction, broadband strong motion seismograms are also potentially useful for improved source modeling [*Hartzell*, 1980; *Choy and Boatwright*, 1981].

4.3   Method for Computing Hybrid Broadband Seismograms

While the near-field terms of the radiated elastic field decay rapidly with distance from the source, the far-field terms persist to large distances. There is, however, no distance at which the far-field terms can be ignored. The relative importance of near-field and far-field terms depends on both distance and frequency [*Aki and Richards*, 1980; *Spudich and Frazer*, 1984; *Ichinose et al.*, 2000] and can be examined using the dimensionless scalar $\gamma = \frac{\omega r}{c}$, where ω is angular frequency, r is distance and c is the wave speed. According to this ratio, the near-field and far-field terms are comparable at low frequencies and short distances ($\gamma \ll 1$), while the far-field terms dominate at high frequencies and long distances ($\gamma \gg 1$) [*Ichinose*
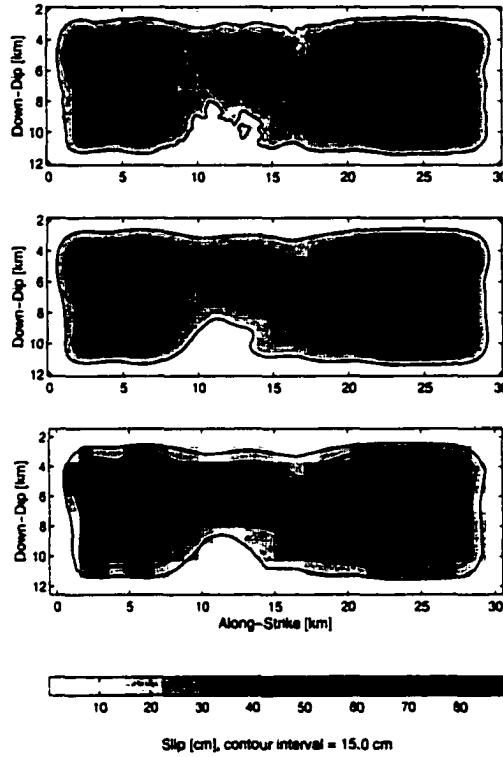
Figure 4-1: Simulated slip distribution for the computation of hybrid broadband seismograms. The top panel shows the source model, $D(\xi)$, that contains short-scale variability at high spatial wavenumbers. We use $D(\xi)$ to compute the high-frequency seismograms. The center panel displays the low-wavenumber filtered version, $D^{LW}(\xi)$, $(k_c = 0.33\,km^{-1})$. The bottom panel shows the decimated version, $D^{LW}_{dec}(\xi)$, used to calculate low-frequency seismograms.

et al., 2000]. Depending on the distance and frequency range of interest, one may use a complete Green's functions code to calculate low-frequency near-source seismograms or a ray-theory approximation for high-frequency seismograms. The computation costs for complete Green's functions, however, increase dramatically with increasing frequency f, and hence its applicability is usually limited to low frequencies ($f \leq 3\,Hz$). Ray-theory seismograms, on the other hand, are very efficiently calculated even up to high frequencies, but they are not accurate at low frequencies.

4.3.1 Theoretical Background

In order to calculate near-source, broadband seismograms for an extended source model, we propose to combine low-frequency, complete seismograms and high-frequency ray-theory
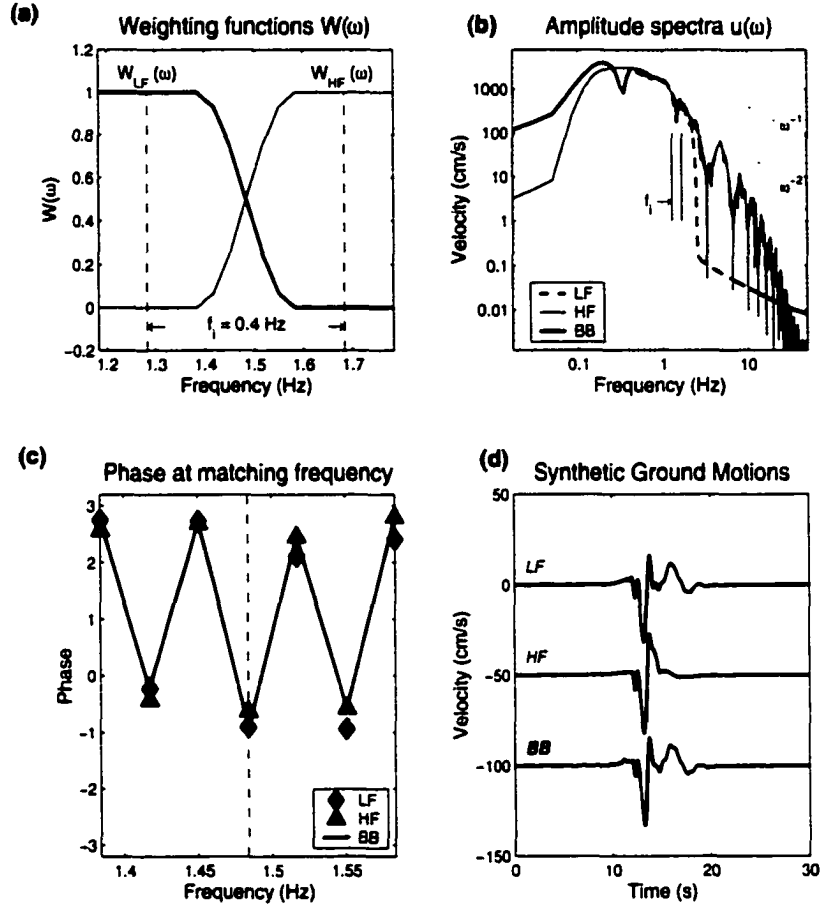
Figure 4-2: Method to compute hybrid broadband seismograms. a) Weighting functions $W(\omega)$ for the amplitude spectra $u^{LF}(\omega)$ and $u^{HF}(\omega)$. b) Amplitude spectra $u^{LF}(\omega)$ and $u^{HF}(\omega)$ and the composite spectrum, $u^c(\omega)$. c) Phase spectra of u^{LF} and u^{HF} at the optimized matching frequency. d) Synthetic ground motions for the fault-normal component, near-field (top), far-field (center) and composite broadband signal (bottom).

seismograms. These composite broadband seismograms reflect realistically the source complexity even at short scale lengths, i.e. they capture the short-range variability of earthquake source models. We reconcile the amplitude spectra of seismograms calculated by the two techniques at intermediate frequencies where their domain of validity overlaps. Independent of their relative contribution to the ground displacement, u, we separately compute the low-frequency and high-frequency displacement, u^{LF} and u^{HF}, respectively, for a two-dimensional dislocation model, $D(\xi)$, that may contain spatial complexity at all scales (ξ is

the position on the fault plane). We combine the low-frequency and high-frequency displacements to form a broadband seismogram as

$$u\left[D(\xi)\right] = u^{LF}\left[D(\xi)\right] + u^{HF}\left[D(\xi)\right]. \tag{4.1}$$

High-frequency, near-source displacements, u^{HF}, are efficiently calculated using ray-theory approximation, even for a finely-sampled dislocation model, $D(\xi)$ (Figure 4-1, top). For the complete low-frequency Green's functions, on the other hand, only the large-scale variations of the dislocation model are important. We therefore decompose the dislocation model, $D(\xi)$, into its low-wavenumber (large-scale) and its high-wavenumber (small-scale) components

$$D(\xi) = D^{LW}(\xi) + D^{HW}(\xi), \tag{4.2}$$

where $D^{HW}(\xi)$ is the high-wavenumber complement of the low-wavenumber dislocation model, $D^{LW}(\xi)$ (filtered at corner wavenumber $k < k_c$; Figure 4-1, center). For source-receiver distances R greater than $R > \frac{2\pi}{k_c}$, it is sufficient to consider a decimated version, $D^{LW}_{dec}(\xi)$, of the low-wavenumber filtered dislocation model to compute the low-frequency displacements [*Berge et al.*, 1998], and hence we approximate

$$u^{LF}\left[D(\xi)\right] \approx u^{LF}\left[D^{LW}_{dec}(\xi)\right]. \tag{4.3}$$

Combining equations (4.1), (4.2) and (4.3) we compute approximate broadband strong ground motion as

$$u\left[D(\xi)\right] \approx u^{LF}\left[D^{LW}_{dec}(\xi)\right] + u^{HF}\left[D(\xi)\right]. \tag{4.4}$$

The composition of the hybrid broadband seismograms is done most effectively in the frequency domain. Using appropriate weighting functions $W^{LF}(\omega)$ and $W^{HF}(\omega)$ that sum to unity at each frequency, we compute the approximate broadband displacments as

$$u(\omega) = u^{LF}(\omega) \cdot W^{LF}(\omega) + u^{HF}(\omega) \cdot W^{HF}(\omega). \tag{4.5}$$

We use the discrete-wavenumber/finite-element technique (DWFE) [*Olson et al.*, 1984], extended to finite-fault source characterization [*Spudich and Archuleta*, 1987; *Spudich and*

Xu., 2002], to compute low-frequency seismograms, and the isochrone integration method [*Spudich and Frazer*, 1984; *Spudich and Xu.*, 2002] to calculate high-frequency ray-theory seismograms. Due to different internal representation of spatial grids in the two codes, minor timing differences occur, which we account for using cross-correlation. Because low-frequency and high-frequency seismograms are computed for the same source model, their phase spectra are virtually identical, and no significant phase mismatch occurs.

Figure 4-2 displays an example for the computation of a hybrid near-source seismogram. We adopt an algorithm similar to the simultaneous deconvolution approach [*Harvey and Choy*, 1982]. After Fourier transforming u^{LF} $[D_{dec}^{LW}]$ and u^{HF} $[D]$, we apply frequency-dependent weighting functions $W(\omega)$ to the individual amplitude spectra. The spectral weighting function $W^{LF}(\omega)$ for $u^{LF}(\omega)$ is unity over the low frequency range, zero at high-frequencies, and tapers as a one-sided Hanning window at the matching frequency ($f \approx 1.5\,\mathrm{Hz}$). $W^{HF}(\omega)$ is a mirror image of $W^{LF}(\omega)$, being zero at low frequencies and unity at high frequencies (Figure 4-2a), and hence both weighting functions sum to unity at each frequency. We obtain the composite broadband amplitude spectrum $u^c(\omega)$ by summing $u^{LF}(\omega)$ and $u^{HF}(\omega)$, multiplied by their respective weigthing functions, $W^{LF}(\omega)$ and $W^{HF}(\omega)$ (Figure 4-2b). Because the phase spectra for both u^{LF} and u^{HF} are determined by virtually the same dislocation model, the differences at the matching frequency are small and require only minor adjustments (Figure 4-2c). Inverse Fourier transform of $u^c(\omega)$ yields the final composite broadband time series (Figure 4-2d).

The velocity time histories in Figure 4-2d are computed for an observer location in almost perfect alignment with the fault and rupture direction (observer 3 in Figure 4-3). The low-frequency seismogram (fault-normal component) clearly shows near-field effects that are not present in the far-field seismograms, like the small initial ramp and the large second pulse (generated by S waves that depart the fault nearly horizontally and that have a horizontal slowness close to that of a horizontally converted P wave at the free surface, resulting in a SV-to-P diffracted wave at the surface which is not accounted for in simple ray theory). These features are correctly represented in the broadband composite seismogram.

4.3.2 Example for Hybrid Broadband Seismograms

We illustrate the method for a moderate strike-slip earthquake using a source-receiver configuration similar to the station distribution and fault location in the 1984 Morgan Hill, California, ($M_w = 6.2$) (Figure 4-3). This enables us to compare our broadband strong
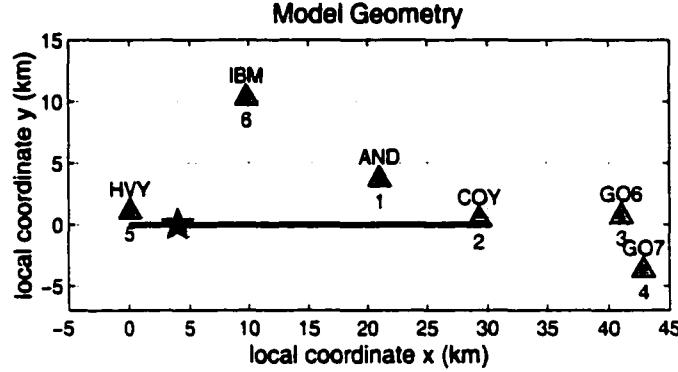
Figure 4-3: Source-receiver geometry used for the earthquake scenarios resembling the 1984 Morgan Hill earthquake ($M_w = 6.2$). The observer locations correspond to station locations that recorded strong ground motions during the 1984 earthquake.

motion simulations to actual recordings, in terms of waveforms, amplitude spectra and response spectra.

The earthquake source is modeled as a rectangular fault plane, discretized in many subfaults. The number of subfaults, and hence the spatial discretization Δx of the rupture plane, depends on the maximum frequency under consideration, f_{max}, and the rupture velocity, v_r, roughly as $f_{max} < \frac{v_r}{\Delta x}$ [*Bernard et al.*, 1996]. In the present application, we consider rupture velocities of about 2.7 km/s and frequencies up to about $f_{max} \approx 10$ Hz, requiring a fault plane discretization of $\Delta x \approx 250$ m in along-strike and down-dip direction. We calculate high-frequency seismograms $u^{HF}[D]$ on a fine grid ($\Delta x = 250$ m) for $f_{max} \approx$ 10 Hz, and complete Green's functions $u^{LF}[D^{LW}_{dec}]$ using a maximum frequency of $f_{max} \approx$ 2.5 Hz and a grid spacing of $\Delta x = 1$ km.

The spatially variable slip distribution on the fault plane is a realization of a *von Karman* autocorrelation function for the power spectral decay of the slip distribution [*Mai and Beroza*, 2001a] (Chapter 3). Figure 4-1 displays the slip realization: the complete dislocation model, $D(\xi)$ (top), the low-wavenumber filtered, $D^{LW}(\xi)$ (middle), and its decimated version, $D^{LW}_{dec}(\xi)$ (bottom). In this example, the correlation lengths in along-strike and down-dip direction are $a_x = 6$ km, $a_z = 4$ km, respectively, the Hurst exponent is $H = 0.8$, corresponding to a fractal dimension $D = 2.2$. This choice for the Hurst exponent generates a slip spectrum that decays slightly more slowly than the k^2-model, in which $H = 1$, and hence the spatial slip distribution contains less short-scale variability [*Herrero and Bernard*,
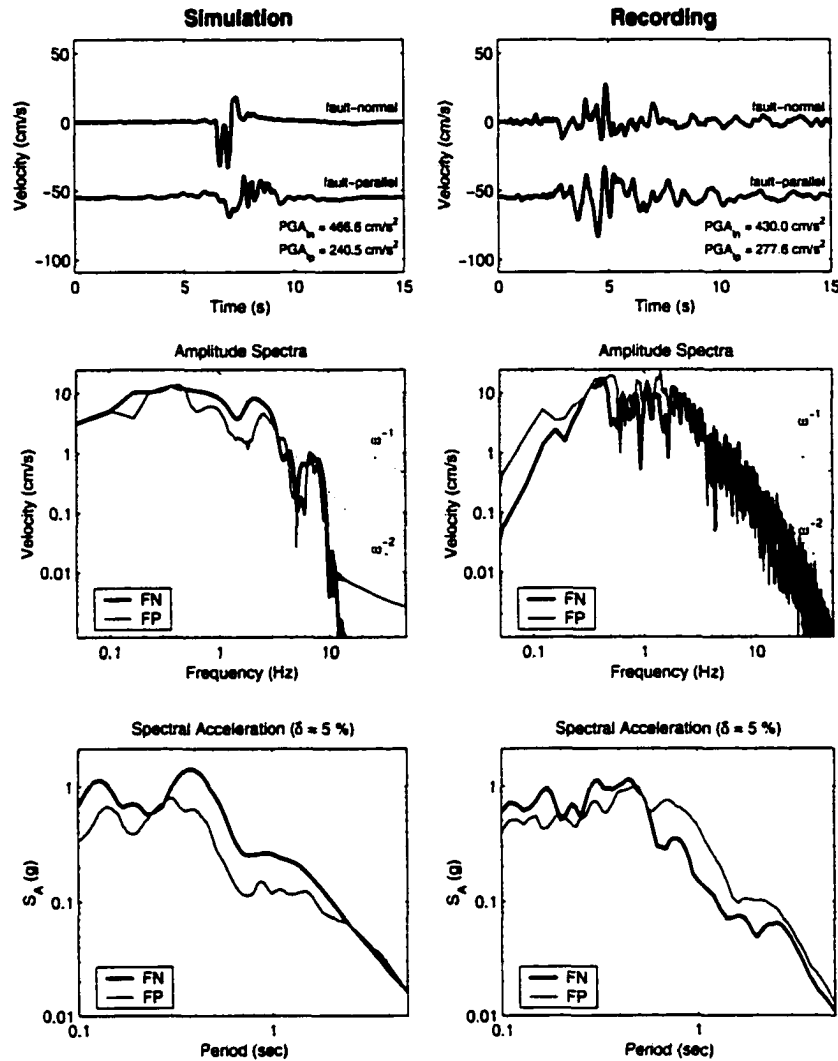
Figure 4-4: Comparison of waveforms (top row), amplitude spectra (center) and response spectra (δ = 5 % damping) (bottom) for simulated broadband strong motion (observer 1, left column) and recordings for the 1984 Morgan Hill, California, earthquake (station AND, right column). Note the close agreement of the PGA-values for both components of the simulated and the recorded waveforms although the source models are different. There is also a good correspondence of the amplitude spectra and the response spectra for the simulated and recorded ground motions, both in terms of spectral shapes and amplitude levels (note that the simulated waveforms are computed up to f_{max} = 10 Hz, whereas the recordings are high-pass filtered at f = 0.05 Hz).

1994]. The final dislocation occurs on a 30 × 10 km fault plane, its moment magnitude is M_w = 6.2. The width of the seismogenic zone is 12 km, and no surface rupture occurs.

Synthetic seismograms in this study are computed for a simple rupture propagation

parametrization, though nothing in our method requires this. In the present example, we construct a *kinematic* source model in which the rupture propagates over the fault plane at a constant fraction of the local shear-wave velocity, $v_r = 0.85 \, v_s$. We also assume a constant rise time of $\tau_r = 0.3\,$s, in agreement with findings for the Morgan Hill earthquake [*Beroza and Spudich,* 1988; *Hartzell and Heaton,* 1986]. The source time function is a simple boxcar function of length τ_r, and is uniform over the fault plane. The hypocenter is located at along-strike coordinate $x = 4.0\,$km and depth $z = 10.5\,$km, the velocity structure is identical to the one used by *Beroza and Spudich* [1988] in their fault-slip inversion.

To account for anelastic attenuation due to energy dissipation and scattering, we use an Azimi operator, assuming a path-averaged Q-value of $Q = 200$ (representative for shallow ray-path in the velocity model). Figure 4-4 displays the resulting time histories (top), Fourier spectra (center) as well as response spectra (bottom) for observer 1, and compares the simulated fault-normal and fault-parallel seismograms with observation at the corresponding station (station AND). Because we are not using the same source model, differences in the waveforms are expected, yet the peak-ground velocity and peak-ground acceleration values are in good agreement with the observations. We find that the velocity spectra of the recorded ground motions decay approximately as ω^{-2} at high frequencies, corresponding to an ω^{-3}-decay in displacement (Figure 4-4 center). This is in contrast to the widely observed ω^{-2}-model for the decay of displacement spectra, and we attribute this rapid decay to attenuation of seismic waves along their travel path. While the simulations are truncated at $f_{max} \approx 10\,$Hz, the recorded ground motions were subjected to a high-pass filter with corner at $f = 0.05\,$Hz, and hence the amplitude spectra should be compared only in the range $0.1 \leq f \leq 10\,$Hz. For further comparison we compute response spectra (SDOF, linear, damping $\delta = 5\,\%$) for the simulated and the recorded ground motions (Figure 4-4, bottom). Though the details of the response spectra vary, their overall shape and their spectral levels for the simulated signals and the recorded ones are about the same. Based on these comparisons, we conclude that our hybrid method for calculating near-source broadband strong motion synthetics yields waveforms, spectral amplitudes and response spectral levels that provide realistic estimates of ground motions expected in future earthquakes.

4.4 Application to Scenario Earthquakes

In this section, we apply our method for computing hybrid broadband seismograms to two earthquake scenarios that resemble past earthquakes, the 1984 Morgan Hill, California, earthquake (strike-slip, $M_w = 6.2$) and the 1992 Northridge, California rupture (dip-slip, $M_w = 6.7$). This allows us to evaluate the quality of our simulations against actual strong motion measurements. For each earthquake scenario, we generate 30 slip distribution, representing slip on the fault plane as a spatial random field with correlation lengths depending on seismic moment [*Mai and Beroza*, 2001a]. In this model, slip heterogeneity is described by an autocorrelation function $C(r)$ in space, or its power spectral density $P(k)$ in the wavenumber domain (r is distance, k is wavenumber). Here, we use the *von Karman* autocorrelation function with $C(r)$ and $P(k)$ given in Chapter 3, Equation (3.1).

The earthquake rupture is modelled kinematically, i.e. we prescribe slip, rise time, rupture velocity and the slip-velocity function (a boxcar in this study). We compute the rise time τ_r for each rupture based on the relation given by *Somerville et al.* [1999], using a log-normal standard deviation of 40 % for rise time w.r.t. to seismic moment. The rupture speed v_r for each model is calculated as a fraction of the shear-wave velocity, with variability in v_r among the models introduced using a normal distribution centered at $v_r = 0.85 \, v_s$.

4.4.1 $M_w = 6.2$ Strike-Slip Earthquake

Figure 4-5 displays 30 realizations of a $M_w = 6.2$ strike-slip earthquake. The source dimensions are computed based on source-scaling relations [*Mai and Beroza*, 2000] (Chapter 2). Slip on the fault plane is generated using a von Karman correlation function with correlation lengths a_x, a_z computed from the scaling of correlation length with seismic moment [*Mai and Beroza*, 2001a] (Chapter 3). Table 4.1 lists the entire set of source parameters, as well as the rise times and rupture velocities (calculated as outlined above). The bottom of each fault plane corresponds to the seismogenic depth at 12.5 km, hence the burial depth of the fault planes are variable. The hypocentral locations are constrained to be at depth $z = 9.5 \pm 2 \, \text{km}$, and along-strike coordinate $x = 5 \pm 2 \, \text{km}$.

Figure 4-6 shows hybrid broadband velocity seismograms and acceleration time histories (obtained by differentiating the velocity seismogram) calculated at observer location 1 (Figure 4-3). We plot the fault-normal component that exhibits large shear-wave pulses due to the SH-wave radiation pattern. In many cases we observe distinct two-sided velocity pulses
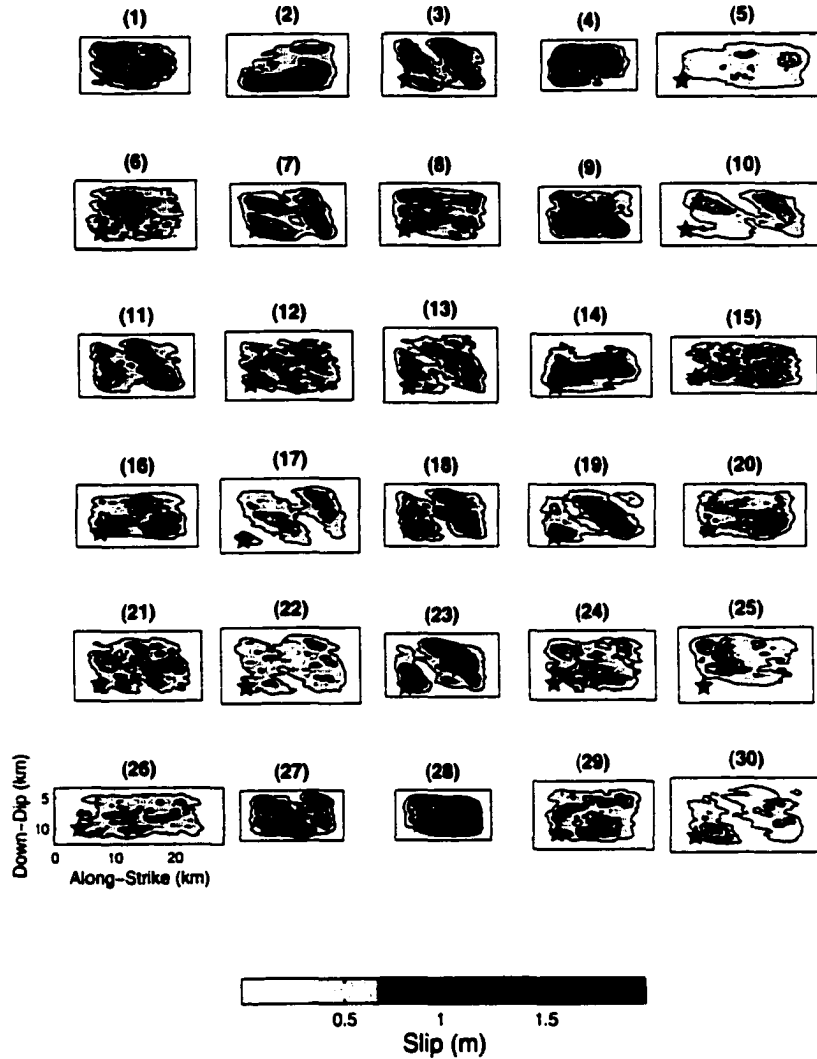
Figure 4-5: 30 realizations of a $M_w = 6.2$ strike-slip earthquake, where slip is color coded and contoured (C.I. = 30 cm). Source dimensions are computed using scaling relations [Mai and Beroza, 2000] the correlation lengths a_x, a_z are calculated as given in Mai and Beroza [2001a]. Table 4.1 lists the parameters of each slip distribution.

that are particularly hazardous to structures. Figure 4-7 displays statistics for the peak ground acceleration (PGA) and peak ground velocity (PGV), and also the median spectral acceleration (S_A) and spectral displacement (S_D). Comparing to the recorded strong ground motion, we find that our simulations slightly underpredict PGA, but overpredict PGV. We also find that the median spectral response of the simulations is smaller than

Table 4.1: Source parameters for 30 realizations of a $M_w = 6.2$ strike-slip earthquake. The rupture dimensions are computed following Mai and Beroza [2000]. The heterogeneity spectra follow a von Karman correlation function with correlation lengths a_x, a_z and Hurst exponent H.

No				Rupture Parameters					Correlation Function	
No	L [km]	W [km]	D [cm]	D_{max} [cm]	M_o [N-m]	τ_r [sec]	v_r-ratio	a_x [km]	a_z [km]	H
1	18	9	41.88	144.81	2.24e+18	0.23	0.86	5.75	2.28	0.96
2	20	10	33.92	115.93	2.24e+18	0.26	0.86	10.88	3.85	0.83
3	19	10	35.71	143.55	2.24e+18	0.42	0.86	7.02	2.98	0.85
4	16	8	53.00	198.66	2.24e+18	0.23	0.87	5.62	2.89	0.90
5	28	10	24.23	72.34	2.24e+18	0.27	0.83	9.97	3.92	0.81
6	20	11	30.84	113.93	2.24e+18	0.23	0.82	8.60	2.65	0.75
7	19	10	35.71	110.18	2.24e+18	0.31	0.83	10.99	4.06	0.96
8	20	10	33.92	117.31	2.24e+18	0.26	0.87	6.11	1.77	0.57
9	17	9	44.34	153.85	2.24e+18	0.28	0.84	9.87	3.82	0.91
10	27	10	25.13	93.66	2.24e+18	0.35	0.78	9.70	3.13	0.78
11	19	10	35.71	125.31	2.24e+18	0.29	0.88	8.61	2.89	0.76
12	21	11	29.37	105.40	2.24e+18	0.27	0.83	7.58	2.14	0.63
13	19	12	29.75	107.87	2.24e+18	0.30	0.86	10.56	2.35	0.52
14	20	10	33.92	122.30	2.24e+18	0.26	0.86	6.43	1.91	0.89
15	24	9	31.41	116.48	2.24e+18	0.30	0.85	9.03	2.27	0.51
16	20	10	33.92	103.41	2.24e+18	0.35	0.82	7.87	2.53	0.70
17	23	12	24.58	95.78	2.24e+18	0.30	0.85	9.18	2.54	0.69
18	19	10	35.71	118.63	2.24e+18	0.28	0.76	7.38	2.43	0.70
19	21	10	32.30	138.00	2.24e+18	0.26	0.81	8.11	2.60	0.71
20	20	10	33.92	115.43	2.24e+18	0.39	0.86	7.42	2.29	0.55
21	21	11	29.37	96.63	2.24e+18	0.35	0.84	10.29	3.29	0.83
22	23	12	24.58	72.97	2.24e+18	0.34	0.85	7.97	2.02	0.60
23	19	10	35.71	144.19	2.24e+18	0.39	0.87	8.64	2.92	0.86
24	21	11	29.37	93.37	2.24e+18	0.28	0.83	10.24	3.33	0.82
25	22	12	25.70	94.54	2.24e+18	0.34	0.85	10.48	3.16	0.73
26	28	9	26.92	93.43	2.24e+18	0.31	0.81	11.02	3.17	0.64
27	17	8	49.88	186.40	2.24e+18	0.34	0.84	6.29	2.39	0.72
28	16	8	53.00	157.81	2.24e+18	0.42	0.82	6.02	2.31	0.68
29	20	11	30.84	114.43	2.24e+18	0.32	0.78	9.95	3.36	0.93
30	25	12	22.61	82.34	2.24e+18	0.41	0.82	9.61	3.58	0.58

the recordings at short periods ($T < 1$ sec), but larger at longer periods.

The observation that the simulated ground motions cannot reproduce the recorded ground motions has lternative explanations. Firstly, we use a simple one-dimensional velocity structure and do not account for local site effects. More importantly, however, the rupture propagation is strongly simplifed (as is the assumption of boxcar slip-velocity function instead of a more realistic Kostrov-type). While the assumed constant rupture velocity produces a smooth rupture propagation that enhances directivity effects (and hence generates large velocity pulses), variability of the rupture velocity may diminish directivity effects but increase high-frequency radiation [Madariaga, 1983]. Dynamic rupture modelling shows
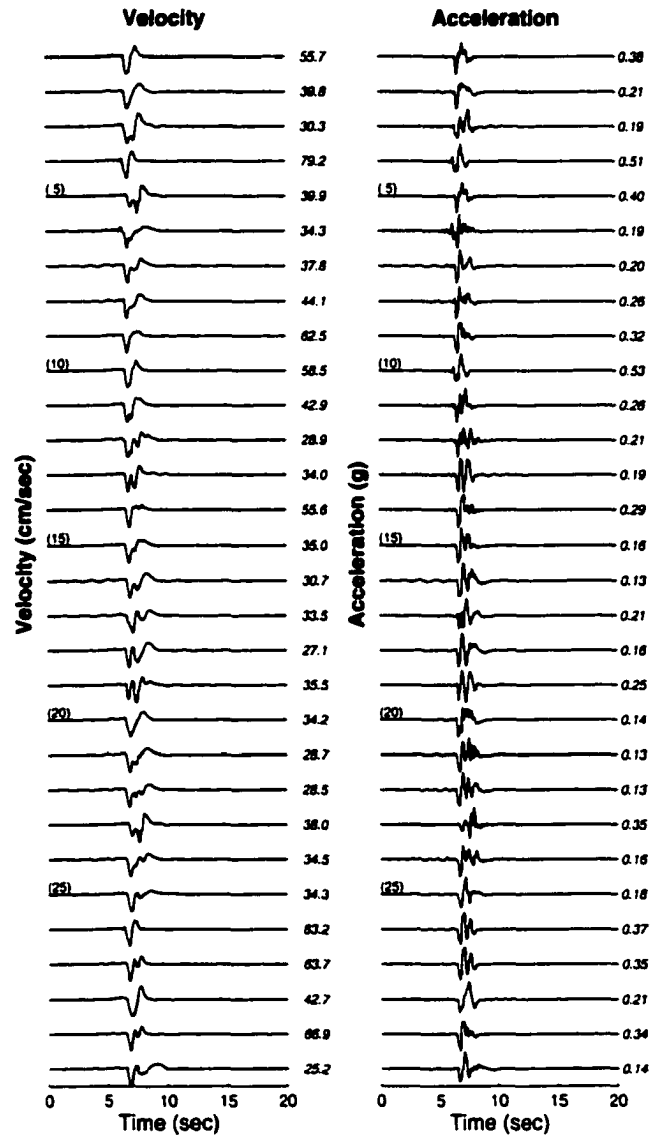
Figure 4-6: Velocity (left) and acceleration time histories (right) at observer 1 (Figure 4-3) for 30 realization of a M_w = 6.2 strike-slip earthquake. All seismograms are scaled to their maximum; the numbers to the right list the individual peak ground velocity and peak ground acceleration, respectively.

the variability of rupture velocity of the fault plane, i.e. the slowing of the rupture front at high-strength barriers and the subsequent acceleration when it overcomes those barriers and ruptures into high-stress regions [Guatteri, 2000b]. Including more physically-motivated distributions of rupture velocity (and rise time) as well as realistic slip-velocity functions
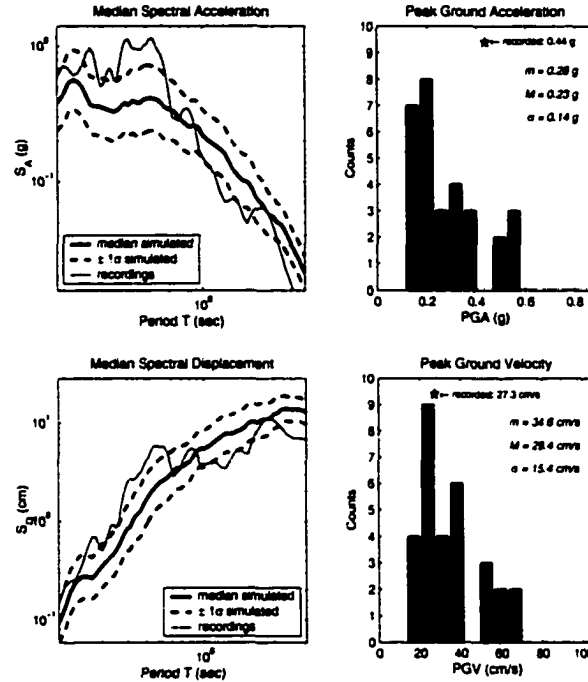
Figure 4-7: Response spectra and peak ground motions for the 30 records shown in Figure 4-6, compared to recordings for the 1984 Morgan Hill earthquake at station AND (observer 1). Mean and median peak-ground accelerations and peak-ground velocities are denoted m and M, respectively, σ is their standard deviation.

into strong motion prediction is an active area of research [Mai and Beroza, 2001b].

4.4.2 $M_w = 6.7$ Thrust-Faulting Earthquake

Figure 4-9 displays 30 realizations of a $M_w = 6.7$ thrust-faulting earthquake. In this example, we fix the source dimensions to 24 km in down-dip, and 18 km in along-strike direction, respectively, in agreement what has been used in the fault-slip inversion [Wald et al., 1996b]. The bottom of the rupture corresponds to the base of the seismogenic zone at 20 km. The top of the fault plane is at 5 km depth, and the fault plane dips at 40°. The hypocentral locations are constrained to be at $z = 17 \pm 2$ km, and along-strike coordinate at $x = 14 \pm 2$ km. Slip on the fault plane is generated using a von Karman correlation function with correlation lengths a_x, a_z computed from the scaling of correlation length with seismic moment [Mai and Beroza, 2001a] (Chapter 3). Table 4.2 lists the entire set of source parameters, as well as the rise times and rupture velocities.
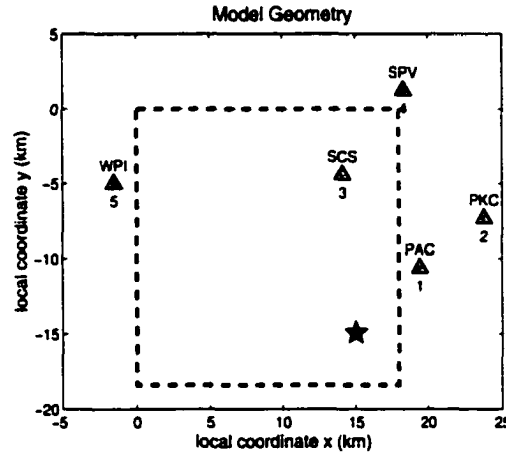
Figure 4-8: Source-receiver geometry used for the earthquake scenarios resembling the 1992 Northridge earthquake ($M_w = 6.7$). The observer locations correspond to a subset of rock sites that recorded strong ground motions during the earthquake.

Figure 4-10 shows hybrid broadband velocity seismograms and acceleration time histories calculated at observer location 5 (Figure 4-8). The fault-normal component exhibits large shear-wave pulses due to the SH-wave radiation pattern. The velocity pulses are broader (i.e. longer period) than in the strike-slip case, and maximum PGV-values are on the order of 120 cm/s. Figure 4-11 displays statistics for the peak ground acceleration (PGA) and peak ground velocity (PGV), and also the median spectral acceleration (S_A) and spectral displacement (S_D). Comparing with the recorded strong ground motion, we find that our simulations reproduce the observed PGA, but slightly underpredict PGV. The median spectral response of the simulations agree with the recordings at shorter periods, but they are smaller at longer periods ($T > 1$ sec). The larger long-period spectral responses are perhaps attributable to unaccounted basin effects.

As for the strike-slip scenarios, several assumptions are built into our simulations which affect the resulting ground motions. We assume a simplified one-dimensional velocity structure for a rock-site geology. This excludes basin-edges effects imposed onto the seismic wavefield by the sedimentary basins in the Los Angeles region. The rupture propagation assumes constant rupture velocity, and a simple boxcar slip-velocity function. We constrain the rake angle to 90° (i.e. pure thrust) while the 1994 Northridge earthquake had somewhat variable rake vectors with an average of 105°. Despite these simplifying assumptions, we find a reasonable agreement between the observed and simulated ground motions.
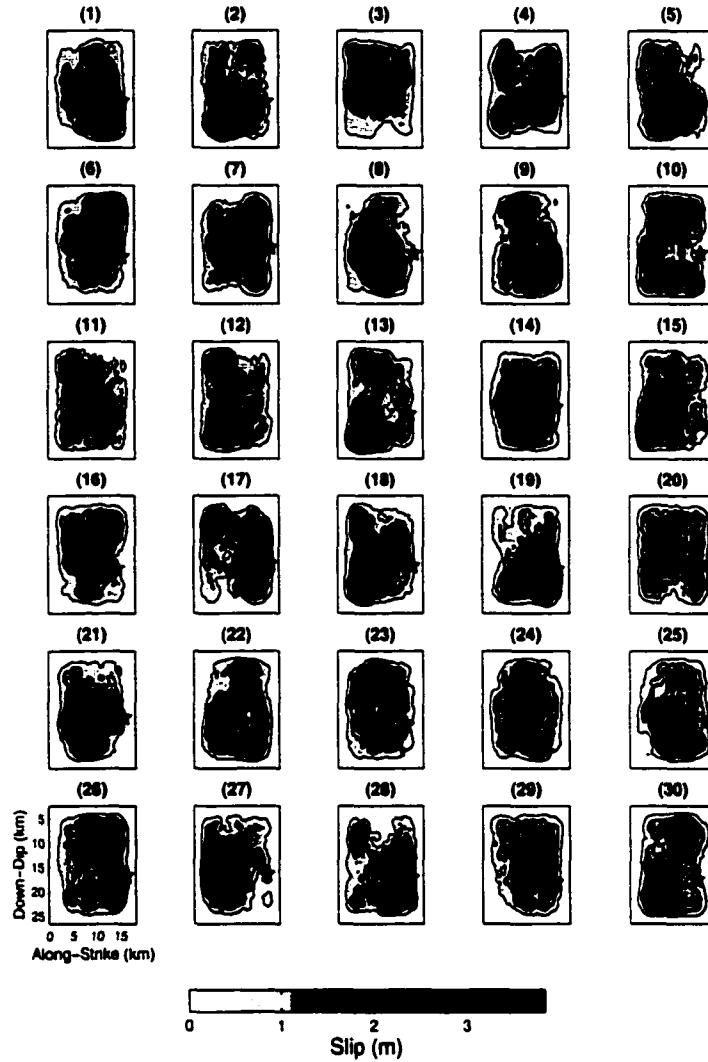
Figure 4-9: 30 realizations of a M_w = 6.7 dip-slip earthquake, where slip is color coded and contoured (C.I. = 50 cm). The source dimensions are fixed to 18 km in along-strike and 24 km in down-dip direction, respectively. The correlation lengths a_x, a_z are calculated as given in *Mai and Beroza* [2001a]. The specifications of each slip distribution are given in Table 4.2.

4.5 Conclusions

We present a hybrid method for calculating near-source broadband strong motion seismograms for an extended source. Our approach does not involve a stochastic wavefield at high frequency, instead seismograms are obtained for a stochastic source model, using ray theory to compute the high-frequency contributions of radiated seismic energy, and complete

Table 4.2: Source parameters for 30 realizations of a $M_w = 6.7$ dip-slip earthquake. The rupture dimensions are fixed to 24 km down-dip and 18 km along-strike. The heterogeneity spectra follow a von Karman correlation function with correlation lengths a_x, a_z and Hurst exponent H.

No	Rupture Parameters							Correlation Function		
	L [km]	W [km]	D [cm]	D_{max} [cm]	M_o [N-m]	τ_r [sec]	v_r-ratio	a_x [km]	a_z [km]	H
1	18	24	88.31	260.34	1.26e+19	0.81	0.81	7.01	10.25	0.89
2	18	24	88.31	337.08	1.26e+19	0.79	0.84	4.84	7.54	0.64
3	18	24	88.31	261.17	1.26e+19	0.89	0.86	7.31	9.38	0.99
4	18	24	88.31	345.88	1.26e+19	0.75	0.89	7.05	8.67	1.00
5	18	24	88.31	338.10	1.26e+19	0.85	0.83	5.44	8.30	0.71
6	18	24	88.31	278.65	1.26e+19	0.84	0.81	6.55	9.68	0.84
7	18	24	88.31	266.01	1.26e+19	0.63	0.82	6.68	9.84	0.86
8	18	24	88.31	284.70	1.26e+19	0.71	0.83	4.90	7.41	0.90
9	18	24	88.31	292.98	1.26e+19	1.09	0.86	6.22	9.27	0.81
10	18	24	88.31	266.90	1.26e+19	0.55	0.80	5.99	8.98	0.78
11	18	24	88.31	307.88	1.26e+19	0.69	0.85	3.85	6.10	0.44
12	18	24	88.31	304.08	1.26e+19	0.77	0.87	5.67	10.83	0.63
13	18	24	88.31	341.56	1.26e+19	1.34	0.83	7.45	10.78	0.94
14	18	24	88.31	252.21	1.26e+19	0.86	0.86	7.03	10.27	0.79
15	18	24	88.31	275.63	1.26e+19	0.57	0.87	5.98	8.96	0.61
16	18	24	88.31	269.95	1.26e+19	1.15	0.83	5.64	7.11	0.82
17	18	24	88.31	279.88	1.26e+19	0.73	0.80	6.71	10.05	0.75
18	18	24	88.31	273.42	1.26e+19	1.02	0.85	6.10	8.69	0.90
19	18	24	88.31	332.33	1.26e+19	0.90	0.85	6.18	9.16	0.83
20	18	24	88.31	251.57	1.26e+19	0.82	0.81	4.34	6.90	0.58
21	18	24	88.31	382.24	1.26e+19	1.02	0.86	7.87	11.44	0.90
22	18	24	88.31	250.52	1.26e+19	1.00	0.79	5.77	8.56	0.73
23	18	24	88.31	306.88	1.26e+19	0.97	0.78	6.46	9.57	0.69
24	18	24	88.31	249.19	1.26e+19	0.72	0.81	7.63	11.01	0.64
25	18	24	88.31	296.55	1.26e+19	0.89	0.82	4.78	7.46	0.81
26	18	24	88.31	232.41	1.26e+19	0.86	0.78	5.90	9.39	0.74
27	18	24	88.31	332.03	1.26e+19	0.98	0.80	6.21	8.07	0.87
28	18	24	88.31	343.62	1.26e+19	0.89	0.87	5.88	8.03	0.81
29	18	24	88.31	263.65	1.26e+19	0.73	0.83	5.64	8.50	0.69
30	18	24	88.31	275.67	1.26e+19	0.61	0.79	7.05	10.30	0.90

Green's functions for the low-frequency terms. We compose the approximate broadband seismograms in the Fourier domain by adding the amplitude spectra, appropriately weighted by frequency-dependent weighting functions. Comparison of waveforms, amplitude spectra and response spectral levels of recorded ground motions validates our approach.

We apply our method to compute composite broadband seismograms to two scenario earthquakes that are meant to resemble past earthquakes: the 1984 Morgan Hill ($M_w = 6.2$) earthquake and the 1992 Northridge ($M_w = 6.7$) earthquake. The waveforms for 30 realizations of each scenario event illustrate the variability of ground motions in the near-field of earthquakes, in particular the pulse-like character of fault-normal velocity waveforms
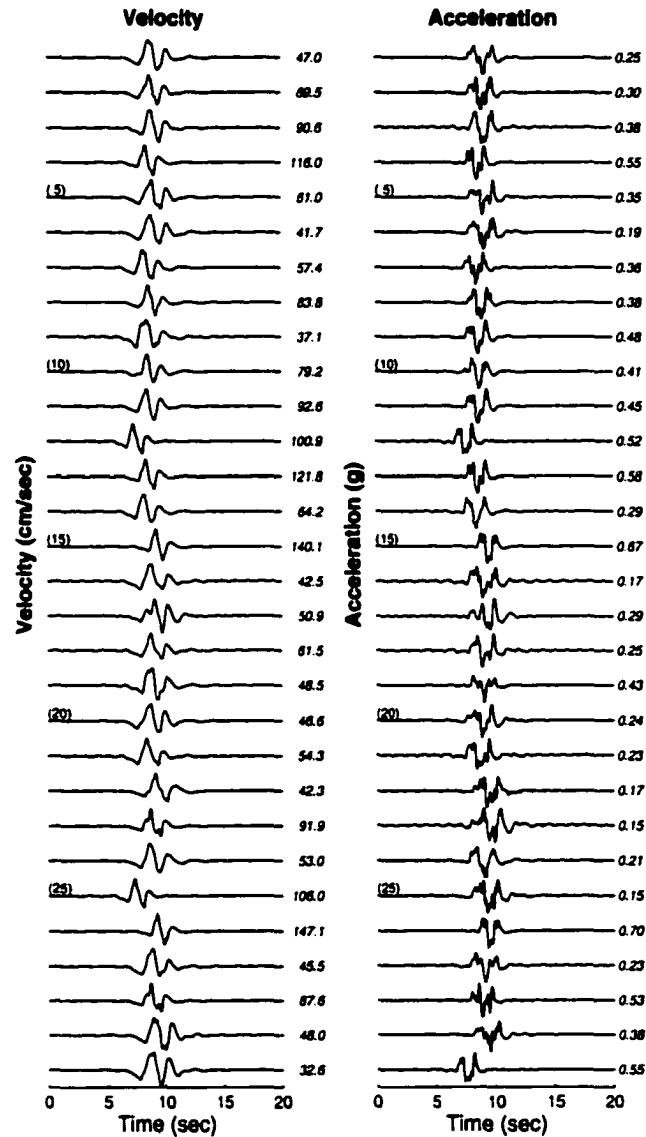
Figure 4-10: Velocity (left) and acceleration time histories (right) at observer 1 (Figure 4-3) for 30 realization of a $M_w = 6.7$ thrust-faulting earthquake. All seismograms are scaled to their maximum; the numbers to the right list the individual peak ground velocity and peak ground acceleration, respectively. Slight shifts in the phase arrival is due to variable hypocenter position.

that are affected by the directivity effect. Median ground motion intensities (response spectral values and peak ground acceleration) for these scenarios are in good agreement with the observed values, but the large scatter of the simulations around these median values may have important implications for seismic hazard. In addition, the availability of
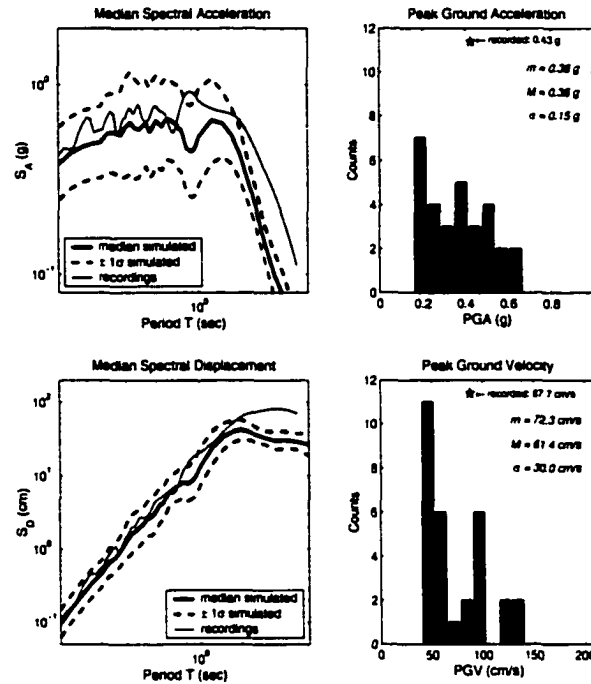
Figure 4-11: Response spectra and peak ground motions for the 30 records shown in Figure 4-10, compared to recordings for the 1992 Northridge earthquake at station WPI (observer 5). Mean and median peak-ground accelerations and peak-ground velocities are denoted m and M, respectively, σ is their standard deviation.

simulated time series for many earthquake scenarios will be beneficial for efforts to model structures as non-linear multi-degree-of-freedom systems.

The ability to compute broadband near-source seismograms efficiently is potentially important for detailed source modeling, because it allows the study of earthquake source complexity in greater spatial and temporal detail. Moreover, the hybrid method for calculating near-source broadband strong motion makes it feasible to compute large sets of near-field strong motion synthetics that capture realistic source complexity at all scales. Such simulations of strong ground motion should help to predict better strong ground motion and its variability in future earthquakes, and thus can add an important capability to seismic hazard studies.

As pointed out already, the strong motion calculations in this chapter are *kinematic*, meaning that we impose a slip model, but we assume the rupture velocity, the rise time, as well as a (simple) slip-velocity function. Moreover, each of these three source parameters

is constant over the fault plane. These are, of course, very strong assumptions, leading to a kinematic source characterization that may not be physical plausible. Dynamic rupture modeling, on the other hand, has shown that the propagation of the rupture front and the rise time are spatially variable as well [*Day*, 1982; *Quin*, 1990; *Guatteri*, 2000b]. Assuming a kinematic source model may lead to larger velocity pulses due to rupture coherency, but the wavefield may be depleted in high-frequency energy (particulary notable in accelerograms, and hence in *PGA*-values) because rupture acceleration/stopping increases high-frequency contributions [*Madariaga*, 1983]. The explanation for the discrepancies between simulated and recorded ground motions is therefore twofold: unknown/unmodeled geology, and unmodeled source characterization.

The use or more detailed velocity models, and incorporating 3-dimensional basin-edge effects by using appropriate simulation codes (e.g. Finite-Differences) comes at high computational costs, but is in principle straightforward. Recent work on wavefield propagation and ground motion amplification in sedimentary basins is based on this approach [*Olsen et al.*, 1997; *Pitarka et al.*, 1998], and future strong motion simulations will inceasingly use this technique. Incorporating more realistic source complexity in strong motion simulation, on the other hand, has not yet received much attention because it requires time-consuming and computational-expensive dynamic rupture modeling. This approach, however, seems very appealing because it provides a self-consistent, physically plausible earthquake source model. In such a dynamic model, rupture velocity, rise time and the slip-velocity function may be spatially variable, and hence such a rupture model may provide very realistic ground motions.

The following Chaper 5 pursues this idea in that we perform dynamic rupture calculations for a set of simulated source models. The resulting dynamic rupture models are then used to develop a *pseudo-dynamic* source characterization that circumvents the need to carry out full-dynamic rupture modeling, but provides an approximate dynamic model with spatially variable rupture velocity, rise time, and slip-velocity function.

4.6 Acknowledgments

Chapter 5

Pseudo-Dynamic Description of Earthquake Source Parameters

5.1 Abstract

We have developed a stochastic-dynamic earthquake source model that characterizes the variability of source properties as observed in past earthquakes, and allows us to calculate near-source ground motions for realistic scenario earthquakes. Our model starts with a random-field characterization of earthquake slip, consistent with published finite-source rupture models (Chapter 3). Using dynamic spontaneous rupture calculations, based on a boundary integral method, we model spatially variable rupture velocity, rise time, and complex slip-velocity functions. Guided by these full-dynamic source parameters we develop a *pseudo-dynamic* source characterization that avoids the full-dynamic calculations. In our *pseudo-dynamic* source model rupture velocity and rise time are parameterized based on stress drop and simple models of rupture dynamics.

We use our earthquake-source model to simulate realistic strong ground motion in order to characterize the variability of source effects in the near-field of large earthquakes. A stochastic source description, and output that consists of strong motion time series for a suite of realizations, rather than a single number or model, merges naturally with a probabilistic approach for seismic hazard analysis.

5.2 Introduction

Parametric scaling relations for strong ground motion, often referred to as "attenuation laws," have been used extensively to predict simple ground motion intensity measures, such as peak ground acceleration (PGA) or spectral acceleration (S_A), as a function of earthquake size and distance [*Abrahamson and Silva*, 1997]. Due to the scarcity of strong motion data in close proximity of fault rupture, however, these attenuation relations may not be adequate in the near-field regime, particularly for large earthquakes.

There is also evidence of important differences in the character of strong ground motion close in to the fault compared with that farther from the fault. In the near-fault regime (the area within about 10 km of the rupture plane), the rise time, the time dependence of slip after rupture, and particularly the directivity effect lead to ground motion that may be dominated by large pulses of short duration, particularly in the forward directivity [*Somerville et al.*, 1997], so that standard measures of ground motion intensity may not capture the damage potential of strong ground motion [*Hall and Heaton*, 1995]. Thus, even though strong motion attenuation relations can be modified to take directivity into account [*Somerville et al.*, 1997], simply extrapolating ground motion intensity measures, such as S_A, from more distant locations to the near-fault region might lead to unreliable predictions of ground motion.

Moreover, the challenges of performance-based engineering will increasingly require to model buildings and structures as what they are: complex, dynamic, non-linear multi-degree-of-freedom systems. This approach requires the entire time series of strong ground motion as input, rather than a single intensity measure, and therefore an alternative approach to strong motion prediction is needed. Given all of these factors we are led to use our limited understanding of earthquake behavior to try to predict the nature of ground motion in the near-fault region.

In this paper we present a stochastic-dynamic approach for the prediction of strong ground motion, in which we model earthquake slip as a spatial random field [*Mai and Beroza*, 2001a]. Using spontaneous rupture modeling, we develop a corresponding description of the temporal evolution of slip, i.e. the rupture velocity, the rise time, and the slip-velocity function. While those parameters could be specified independently, there is no guarantee that the resulting model of earthquake rupture would be physically plausible. In the dynamic modeling, we specify the dynamic parameters of the source, i.e. the

fracture energy and stress drop, as spatial random fields, leading to a self-consistent model of the entire spatio-temporal evolution of earthquake rupture. Based on the dynamic rupture modeling, we develop a parametrization of variable rupture velocity and variable rise time using the stress drop (derived from slip distribution) and simple models of rupture dynamics. Thus, we obtain a *pseudo-dynamic* earthquake source model that avoids the computationally expensive dynamic rupture calculations, but provides realistic temporal variability of the rupture process, a key factor for improved strong motion prediction.

5.3 Stochastic-Dynamic Rupture Modeling

Dynamic descriptions of the earthquake source are based on models that satisfy elasto-dynamic equations with a prescribed fracture criterion on a pre-determined fault plane [*Andrews*, 1976a; *Day*, 1982; *Das and Kostrov*, 1987; *Quin and Das*, 1989]. An earthquake is modeled as a dynamically propagating shear crack that radiates seismic waves. The slipping fault is associated with a drop in shear stress, and the evolution of rupture depends on the initial conditions and the failure criterion. *Kinematic* descriptions of the earthquake source, on the other hand, specify the slip as a function of space and time *without* explicit consideration of a physical model for the rupture process, which therefore may not be physically realizable. We model spontaneous rupture using a boundary integral method [*Boatwright and Quin*, 1986; *Das and Kostrov*, 1987], modified to include the effect of the free surface reflection and a layered velocity structure [*Guatteri and Spudich* 1998].

The details of the dynamic rupture modeling are described elsewhere [*Guatteri*, 2000b], and we therefore summarize only the key steps. Assuming a homogeneous distribution of initial stress over the fault plane, we impose the static stress drop distribution derived from simulated slip realizations [*Mai and Beroza*, 2001a], for which we compute stress drop using (B.4) and (B.5) [*Andrews*, 1980a]. We assume that the fault responds to the imposed stress following a slip-weakening friction model in which friction drops from a static level to a lower dynamic level over the characteristic slip-weakening displacement (Figure 5-1). Given the initial shear stress, σ_0, the slip-weakening model is described by the stress drop, $\Delta\sigma = \sigma_0 - \sigma_f$, the strength excess $\sigma_y - \sigma_0$, and the slip-weakening displacement, D_c, after which the stress has reached the dynamic friction level, σ_f. The slip-weakening model can be thought of as an approximation to more general fault-constitutive behavior [*Guatteri et al.*, 2001], and eliminates the singularity in stress and slip velocity at the crack tip, which
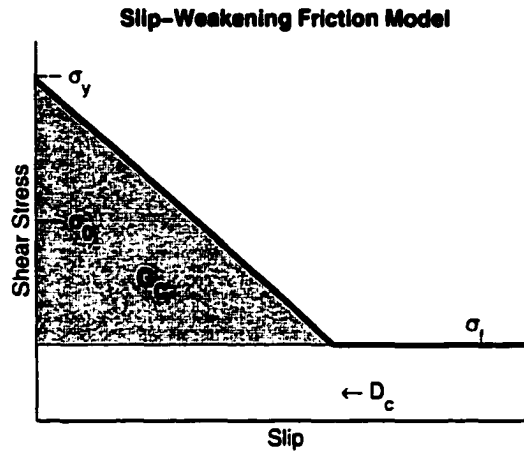
Figure 5-1: Slip-weakening friction model for dynamic rupture modeling. See text for details.

is present in elastic-brittle models. The fracture energy, G_c, is the energy per unit area required to extend the crack, and hence is a measure of the resistance of the fault to failure. Fracture energy is simply the area under the slip-weakening displacement curve.

The combination of the stress drop distribution, the friction law, and the fracture energy distribution is sufficient to specify a dynamic rupture model, with the only additional parameter being the hypocenter where rupture initiates. For each model, we prescribe the fracture energy distribution, using the respective stress drop distribution and spatially homogeneous values of strength excess and slip-weakening distance. Then, by *trial and error* we perturb the distribution of stress excess and slip-weakening displacement on selected portions of the fault plane, to obtain a (non-unique) fracture energy distribution that results in a sub-shear rupture speed over the fault. In our modeling the average rupture velocity is 85 % of the shear-wave velocity, consistent with observations of the average rupture velocity in previous earthquakes.

5.3.1 Earthquake Source Models

The realizations for the scenario earthquake we consider are designed to be representative of a $M_w = 7.0$ strike-slip earthquake in California. We assign fault length ($L = 36\,\text{km}$) and a fault width ($W = 16\,\text{km}$) consistent with source-scaling relations [*Mai and Beroza*, 2000]. Rupture models, A, B, and C are based on three different slip realizations having the same hypocenter at $x = 10\,\text{km}$ in along-strike direction at a depth of 11 km. Figure 5-2 displays
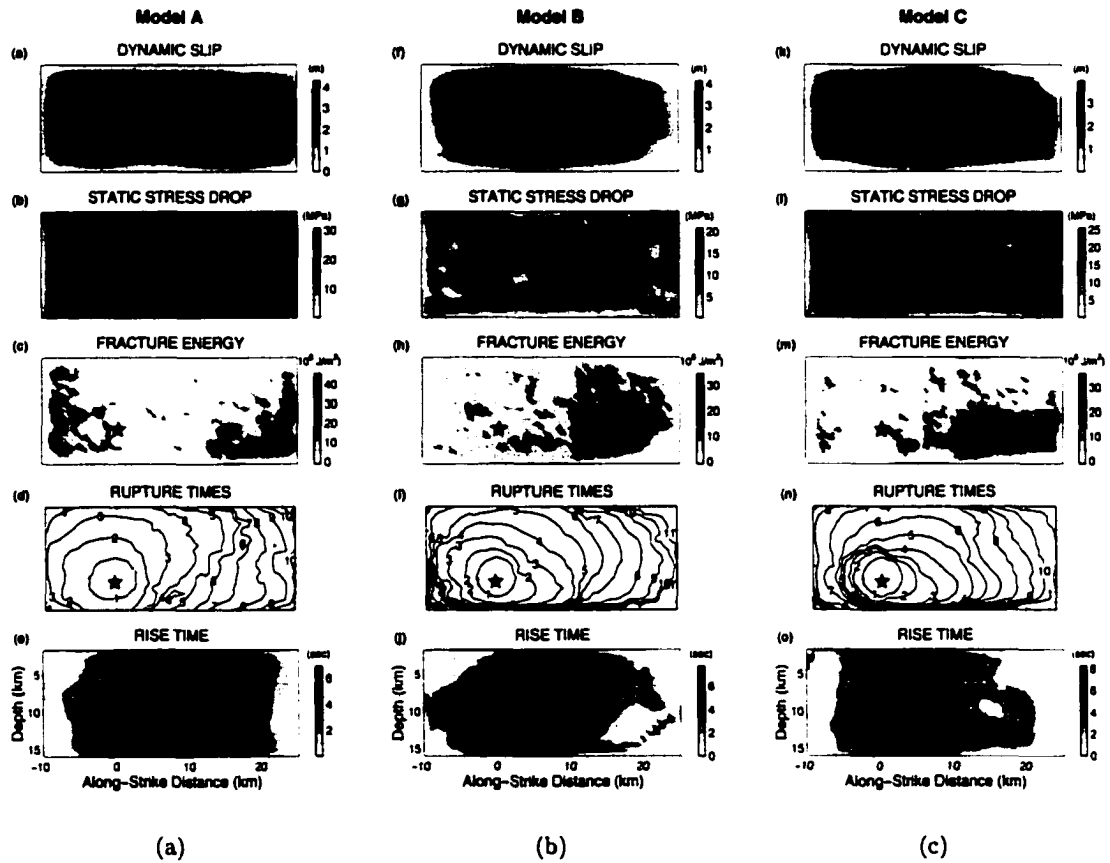
Figure 5-2: Distribution of input parameters for dynamic rupture modeling (b,c; g,h; l,m) and the resulting rupture times and rise times (d,e; i,j; n,o) for models A, B, C. The star marks the hypocenter. See text for details.

the distribution of source parameters for models A, B, C.To further investigate directivity effects , we introduce models D1, D2 and D3 which are based on model B, but have different hypocentral locations at 15, 20, and 25 km along strike, respectively (Figure 5-3). The top row shows the spatial distribution of slip on the fault plane, the second row displays the corresponding distribution of static stress drop, followed by the modeled distribution of apparent fracture energy (third row). The latter two are the input parameters for dynamic rupture modeling.

Contours of rupture times that arise from the spontaneous rupture calculation, and the local rise time (defined as the time required to accumulate from 10 % to 90 % of the total slip at a point on the fault) are displayed in the bottom rows. Notice that the variability
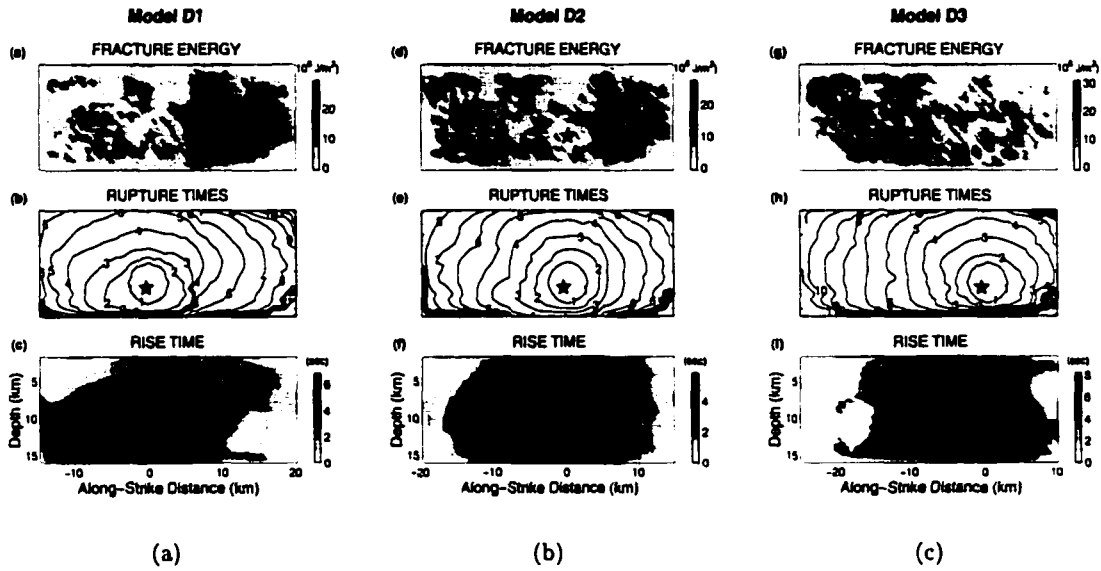
Figure 5-3: Distribution of fracture energy, rupture time and rise time for models D1-D3 with identical slip (stress drop) distribution of model B (Figure 5-2), but variable hypocenter location (denoted by the star). Notice the change of the fracture energy distribution, and hence the rupture times, with varying hypocenter.

in rupture time and rise time is a derived, rather than an assumed characteristic of the rupture model, depending, however, on the assumptions used to model fracture energy. The distribution of fracture energy changes for the various models to maintain average sub-shear rupture velocity over areas of high slip. Peak values of the fracture energy shift, to be located away from the hypocenter, because the rupture tends to accelerate as it grows due to an increase in the strength of the dynamic stress concentration [Andrews, 1985]. Although the average rupture velocity over the fault plane remains sub-shear, locally it may approach the shear-wave velocity in regions of high stress drop. Together, slip, rupture time and rise time form a complete description of the temporal behavior of slip during an earthquake. Since our modeling commences with kinematic slip distributions that are based on the character of slip variability in past earthquakes, such a dynamic source model may represent a viable approximation to the complex rupture process occurring in real earthquakes.

In this study, we seek to characterize the spatial and temporal variability of the earthquake source without carrying out full dynamic rupture modeling (which is time-consuming and CPU-intensive). To do so, we develop a *pseudo-dynamic* rupture characterization,
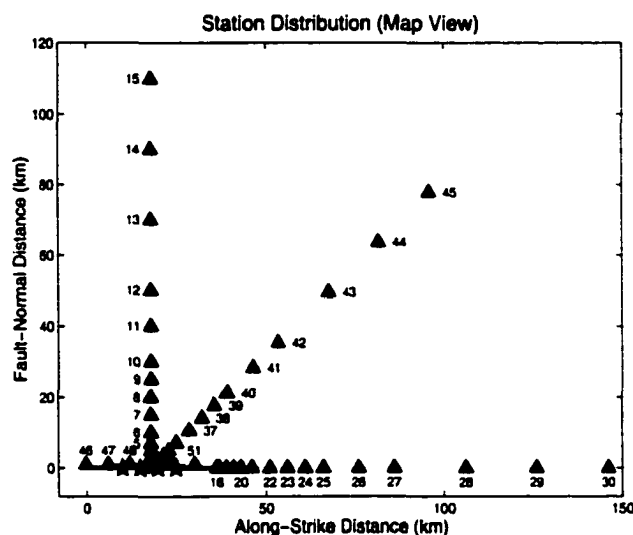
Figure 5-4: Observer locations (triangles), and hypocenter positions (stars) used for strong motion simulations. The fault stretches from 0 to 36 km.

based on stress drop, that can be used to calculate realistic strong motion seismograms. Before we proceed, however, we compute synthetic seismograms for the dynamic rupture models to evaluate how well they match empirical attenuation relations, and to determine what degree of complexity we need to include in source characterizations to improve strong ground motion prediction with respect to traditional *kinematic* approaches.

5.4 Strong Motion Simulation for Dynamic and Kinematic Source Models

We demonstrate the advantages of a dynamically consistent source characterization over a simple kinematic approach by calculating synthetic seismograms for both sets of source models. The fault plane is discretized into 960 subfaults (0.75 × 0.75 km). Using the previously described DWFE-method [*Olson et al.*, 1984] in the COMPSYN- package [*Spudich and Xu.*, 2002], and a generic velocity structure in California [*Boore and Joyner*, 1997], we calculate ground velocity at 51 observer locations (Figure 5-4) in the frequency band 0 - 2.3 Hz. The choice of the station distribution was motivated by the need to simulate strong-ground motion in the near-fault region ($R \leq 10$ km), where the sparsity of recordings affects the reliability of current parametric scaling relations. At intermediate to large

distances, the density of available recordings allows model validation. We compare response spectra for simulated ground motions against the empirical attenuation relations (rock sites, 5% damped) of *Abrahamson and Silva* [1997], derived for a worldwide data set of shallow crustal earthquakes. This data set, however, contains only very few recordings of $M_w \geq 7$ earthquakes to constrain these relations at short distances.

Corresponding to each *dynamic* model, we develop the *kinematic* source characterization in which we assign the original kinematic slip distribution, a box-car slip-velocity function of constant rise time ($\tau_r = 1\,\text{sec}$) over the entire fault plane, and a uniform rupture velocity equal to 85% of the local shear-wave velocity. Figure 5-5 displays velocity waveforms as well as Fourier spectral amplitudes at a near-source location. The simple pulse-like character of the kinematic waveforms (with large *PGV*-values) are due to the coherent rupture propagation (constant v_r) and the simple, constant slip-velocity function (boxcar, constant τ_r), also accounting for the depletion of high-frequency seismic energy which is generated by changes in the rupture velocity [*Spudich and Frazer*, 1984]. The dynamic waveforms, in contrast, are more complex, with longer wavetrains and more high-frequency energy ($f \geq 1\,\text{Hz}$), owing to the variable rupture propagation and variation of the slip-velocity function in space and time.

Figure 5-6 compares empirical and simulated spectral acceleration at several periods for the two simulation approaches. For each method we plot the geometric mean of the two simulated horizontal components of spectral acceleration for all slip models and all stations, excluding stations 16-30 (aligned along a nodal plane where the fault-parallel component of motion is zero). Note that the near-fault ground motions ($R \leq 2\,\text{km}$) show much more variability of S_A in the dynamic models than in the kinematic models, attributable to variations in the slip-velocity function, and hence variations in directivity. Interestingly, the variability in S_A in this near-source region is much greater for both simulation approaches than empirical predictions, yet, their average S_A-values are lower. This effect is partly be due to the three-dimensional radiation pattern, however, it is largely explained by the location of areas of high stress drop with respect to the individual observers[1]. These observations only underscore the importance of understanding better the rupture dynamics to be able to

---

[1]The measure of closest rupture distance, R_{rup}, cannot capture the larger distance from the observer to the centroid location (region of largest moment release). Plotting S_A using such a distance measure, $R_{centroid}$, largely eliminates this effect of low spectral accelerations in the extreme near-field. This approach, however, is not useful in the prediction exercise as we do not know in advance where the largest moment release will occur on the fault plane.

Near-Source Synthetics, obs. 3 (R_{rup} = 3.2 km, fault-normal)
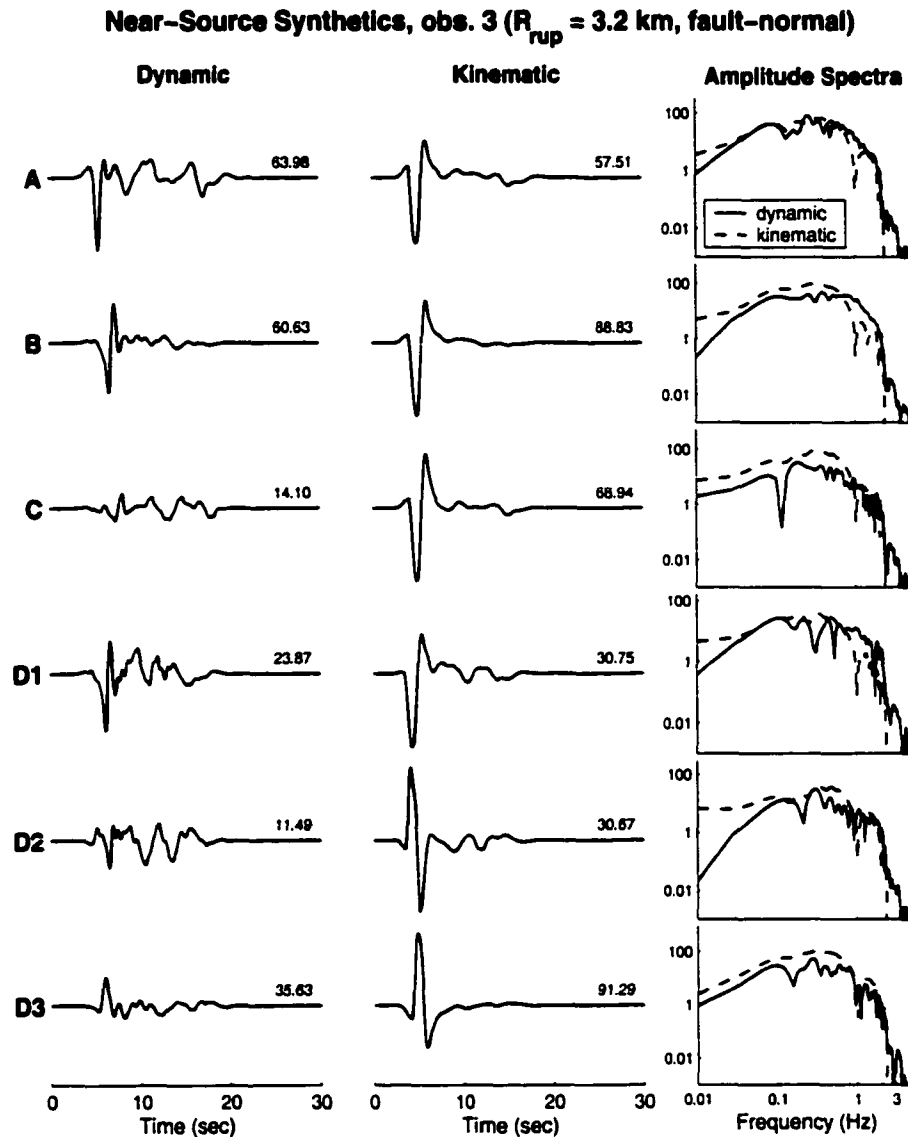
Figure 5-5: Dynamic (left) and kinematic (center) near-source velocity seismograms with their Fourier spectral amplitudes (right) for the six source models A-C, D1-D3. The small numbers indicate *PGV*-values. Note the difference in amplitude, waveform character, and spectral shape between the two sets of simulations. See text for details.

reliably predict strong ground motion in the near-fault region. In general, the simulations from the kinematic approach underperform those obtained from the dynamic model, both in response- spectral levels as well as in the consistency of the distance-decay with the empirical relation.
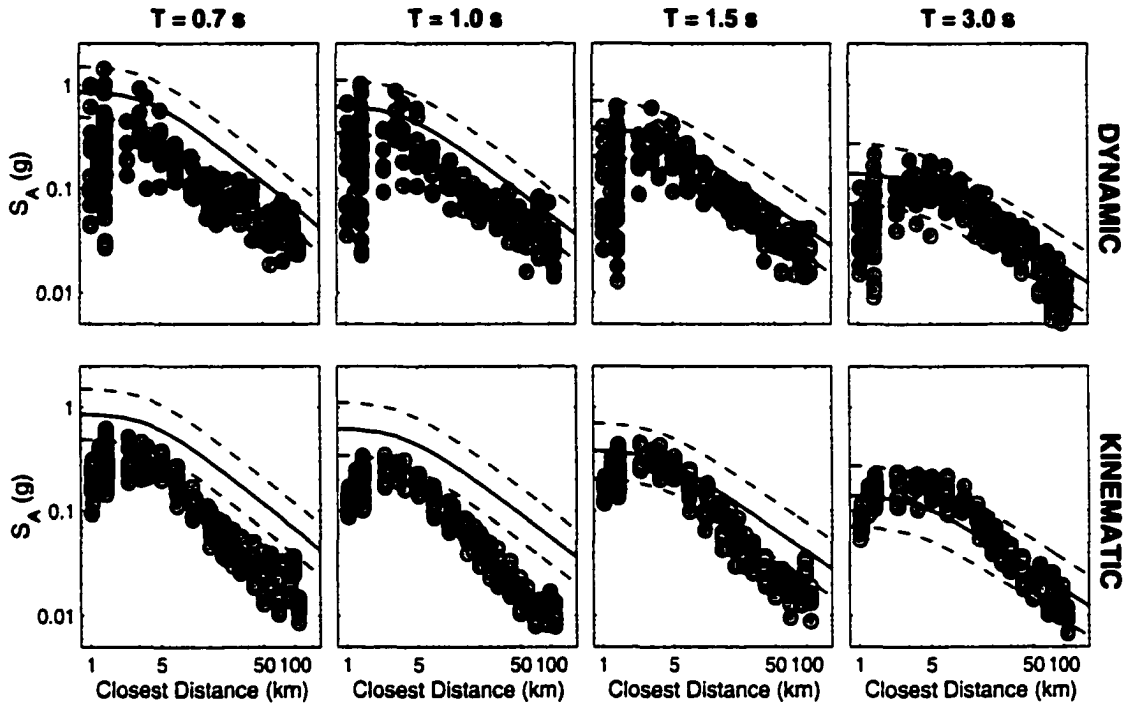
Figure 5-6: Simulated and empirical average-horizontal spectral acceleration (*Abrahamson and Silva* [1997], solid line; dashed line indicates standard deviation) for $M = 7$ strike-slip earthquakes. The simulated values were obtained for source models A-C, D1-D3, for both the *dynamic* and *kinematic* approach. Only non-nodal stations are shown (see text).

We observe that the dynamic simulations follow the slope of the empirical relation better than the kinematic approach, particularly at intermediate distances, where sufficient data exist to constrain the empirical relations. At short periods ($T = 0.7$ s), the simulated spectral accelerations are depleted in high frequency with respect to the empirical values. At longer periods ($T > 1.5$ s), the kinematic simulation roughly agrees with the empirical relations at close distances, with remaining discrepancies at intermediate (for $T = 3$ s) and large (for $T = 1.5$ s) distances. It's interesting to note that the dynamic simulations agree well with the empirical relations for longer periods over all distances but the extreme near-field ($R < 3$ km). In this regime, our simulations show a much greater variation of S_A than empirically predicted, and median spectral levels appear to be smaller than what extrapolation of attenuation laws from large distances would predict [2].

[2]By analyzing the response spectra for the source models D1-D3 (not shown here), we also find that the dynamic simulations capture the variability of directivity effects among those models with different

Based on the comparison of simulated strong ground motions for *dynamic* and *kinematic* source models, we conclude that strong motion prediction can be significantly improved if we include dynamically-consistent source parameters. By that we mean to consider spatial variations of the rupture velocity, the rise time as well as a realistic slip-velocity function in strong motion computations.

5.5 Pseudo-Dynamic Source Characterization

As pointed out already, spontaneous rupture calulations are CPU-intense and time consuming, and involve the researchers experience (and subjectivity) for modeling the fracture energy. There is no doubt that this approach to dynamic rupture modeling is too tedious to be applied routinely to strong motion prediction for scenario earthquakes. On the other hand, we have also seen that variability in rupture velocity and rise time greatly affect the gound motion estimates. It is therefore our goal to find a *pseudo-dynamic* earthquake source model that avoids the full-dynamic calculations, but still approximates the spatial variability of dynamic source parameters.

5.5.1 Rupture Velocity

To help develop realistic source models, it is important to discuss how rupture velocity is expected to vary over the fault plane for a given slip distribution. As the crack grows, the rupture tends to accelerate [*Andrews*, 1985; *Day*, 1982] due to the effect of dynamic loading from the ruptured area of the fault. Areas of local high stress drop, $\Delta\sigma$, also promote fast rupture propagation. For this reason relatively large values of fracture energy, G_c, corresponding to high fault resistance, are needed there to slow down the accelerating rupture growth. The variability in the rupture time distribution is a result both of heterogenous stress drop and fracture energy distributions.

The set of models with identical slip model, but varying hypocenter allows us to study the variability of rupture velocity with respect to stress distribution and hypocenter location. Though the median values of fracture energy are comparable for each source model (Figures 5-2, 5-3), the location of zones of large fracture energy depends on the hypocenter location. As discussed above, local large values of G_c are necessary as soon as the crack has

---

hypocenters, while the analysis of the kinematic results does not reveal any substantial difference among these models. See *Guatteri et al.* [2000] for details.
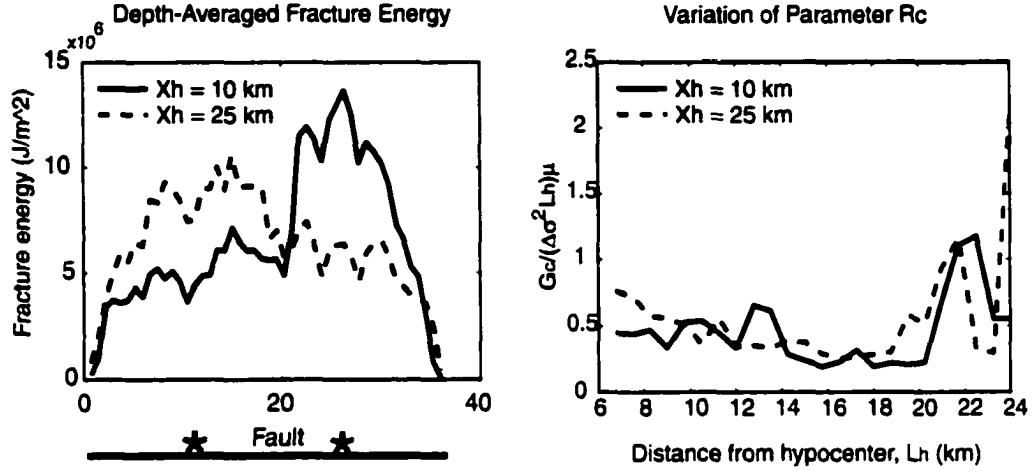
Figure 5-7: (Left) Depth-averaged fracture energy for dynamic rupture models with identical slip distribution, but varying hypocenter (stars) (model B, D3). X_h denotes the hypocenter position in along-strike direction. Large values of fracture energy occur where it is necessary to slow down rupture velocity. (Right) Dimensionless parameter R_c that depends on fracture energy, stress drop, and crack length. The similarities of R_c for the two different models suggests that R_c controls the rupture velocity even in a 3D, heterogeneous model (modified after *Guatteri et al.*, [2000c]).

extended over large distances. Figure 5-7 (left) shows the depth-averaged fracture energy for model B and D3 (same slip, different hypocenters) that represent the two extremes with regard to the effect on the local rupture velocity. The right panel displays a dimensionless parameter, R_c, defined below. *Andrews* [1976a] obtained an analytical relation between rupture velocity and fracture energy, stress drop and crack length, L_c, valid in simple anti-plane strain with uniform stress drop and frictional properties. We define the dimensionless parameter R_c which we call crack resistance

$$R_c = \frac{\mu \cdot G_c}{\Delta\sigma^2 \cdot L_c} \tag{5.1}$$

and rewrite *Andrews'* equation 23 in terms of R_c

$$1 - \frac{\nu^2}{\beta^2} = C \cdot \left[\frac{R_c}{2}\right]^2. \tag{5.2}$$

In (5.2), ν is the rupture velocity, β is the shear-wave velocity, μ is the shear modulus, $\Delta\sigma$ is the stress drop, and L_c is the crack length, taken to be the distance from the hypocenter.
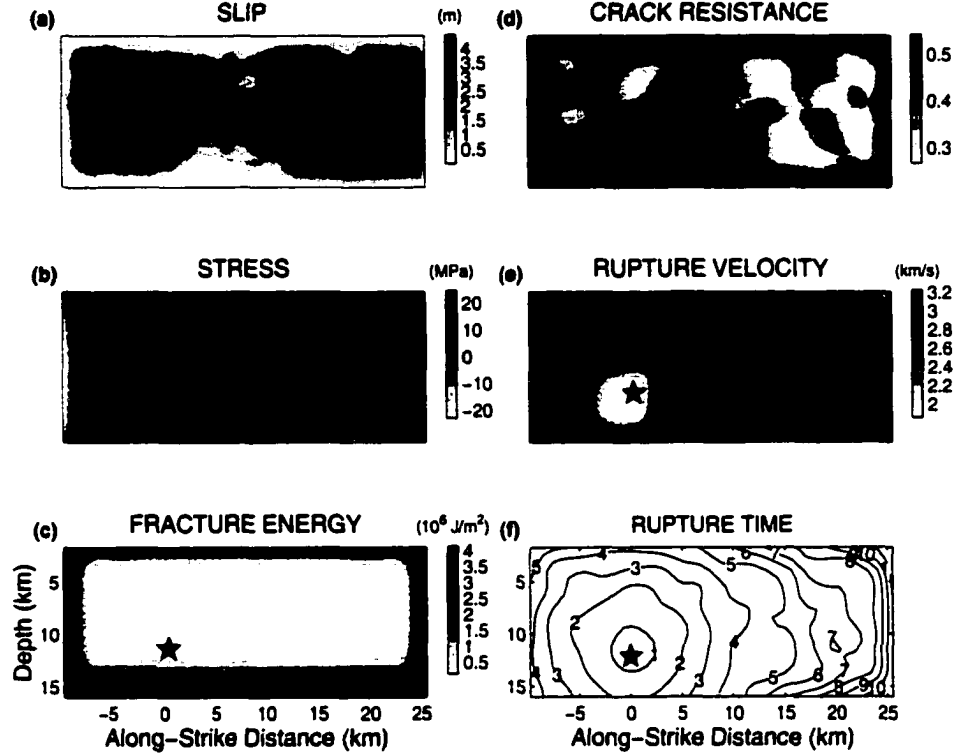
Figure 5-8: Example for the computation of variable rupture velocity based on (5.3). Slip and stress (a,b) are known, the fracture energy (c) is chosen to stop the rupture at the fault edges. The crack resistance, R_c, (d) displays spatial variability which is mapped in the rupture velocity (e), and hence into the rupture time contours (f).

For the case of simple anti-plane strain, the constant C is about 2π. Even though the models shown in Figure 5-7 have different hypocenters, their rupture velocities are very similar, in particular away from the hypocenter ($L_c > 7$ km). The similarity between the parameter R_c for these two models suggests that Andrews' relation applies approximately to 3-D heterogenous dynamic models. The median value of R_c for model B ($Xh = 10$ km) is about 0.4, and assuming an average rupture speed of about 85 % of the shear-wave speed, we can empirically determine $C \approx 7$, comparable to Andrews' result.

Based on these observations, we write (5.2) in a form that can be used to estimate the local rupture velocity for known stress drop and crack length, and an assumed or modeled fracture energy,

$$\nu = \beta \cdot \left[1 - \frac{\pi^2}{4} \cdot R_c^2 \right]^{\frac{1}{2}} \tag{5.3}$$

Distribution of Dynamic and Pseudo-Dynamic Rupture Time
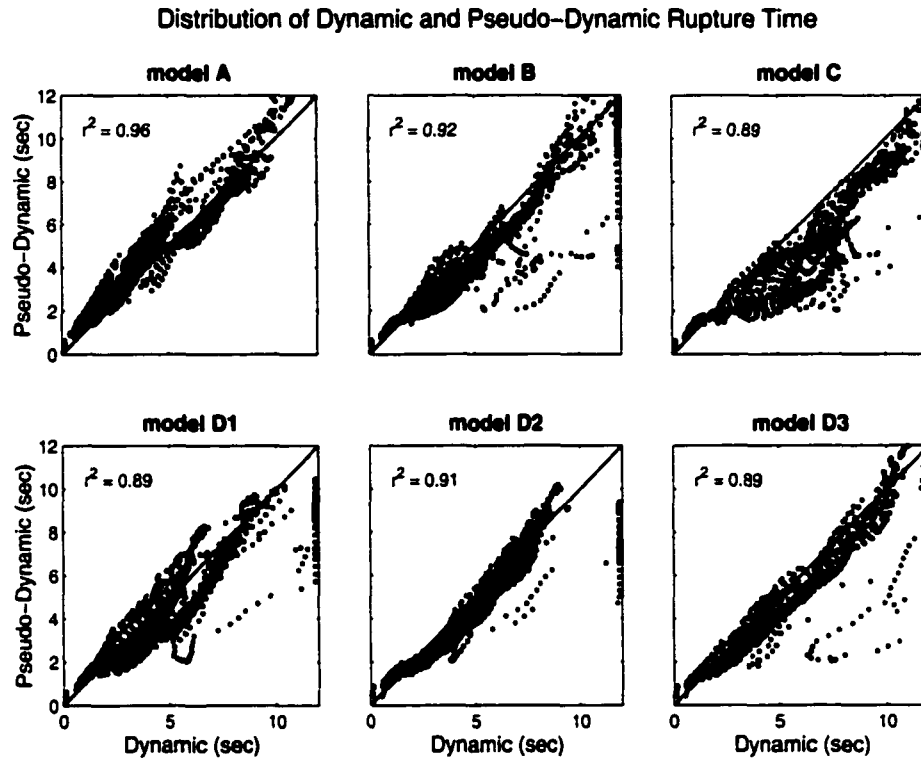
Figure 5-9: Scatter plots for *pseudo-dynamic* versus *full-dynamic* rupture times for all six source models. The center line indicates where the values would fall for a perfect match; r^2 denotes the correlation coefficient.

where R_c is defined above. We then use (5.3) to calculate the rupture time distribution consistent with corresponding stress drop distribution (Figure 5-8). The fracture energy distribution is chosen such to stop rupture at the fault edges. We also introduce a small circular nucleation zone around the hypocenter in which rupture starts to grow slowly, in accordance with dynamic rupture modeling [*Day*, 1982; *Archuleta*, 1984]. The size of the nucleation zone is computed from an informal regression to the nucleation radii measured for earthquakes of various magnitude [*Beroza and Ellsworth*, 1996].

Applying (5.3) to models A, B, C as well as D1 - D3 allows us to quantify the quality of our approximation. In Figure 5-9 we plot the *pseudo-dynamic* rupture times over the *dynamic* rupture times. If these rupture times matched perfectly, they would fall onto a single line (indicated in each panel). Of course, the correspondence is not perfect, but the correlation coefficients of $r^2 \approx 0.9$ indicate a large degree of consistency between the
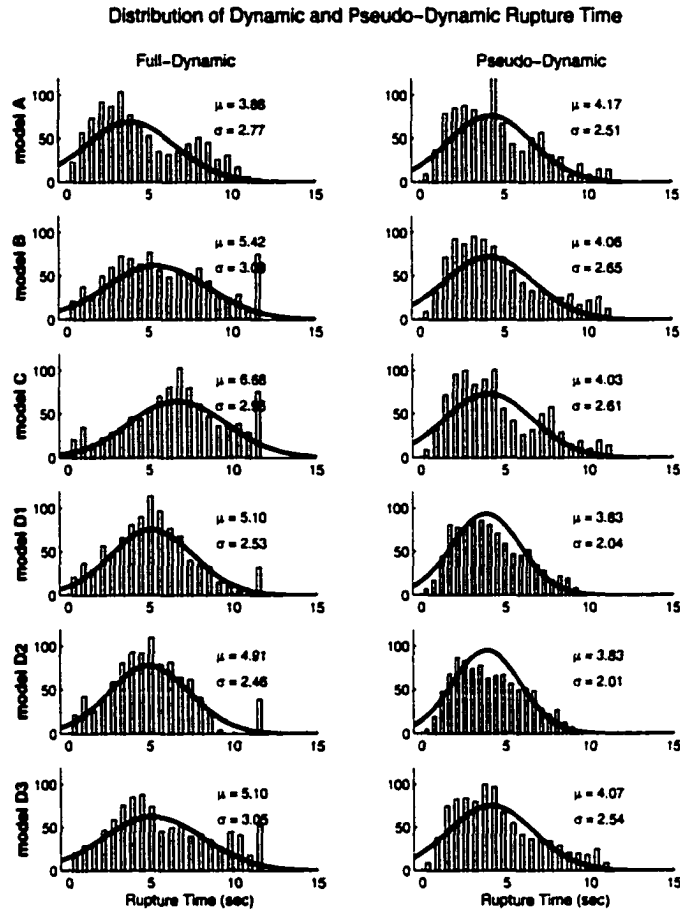
Figure 5-10: Marginal distributions for the *full-dynamic* (left) and the *pseudo-dynamic* rupture times (right) for all six source models. In each panel, the population mean is given by μ, the standard deviation by σ. Note the good agreement between the two distributions for a given source model.

full-dynamic and the *pseudo-dynamic* rupture times. We also find good agreement between the marginal distributions of the rupture times for each source model (Figure 5-10), and we therefore conclude that (5.3) provides a useful relation to estimate spatially variable rupture velocity. Using this approach, we assume a very simple, and largely unphysical distribution of the fracture energy (Figure 5-8). Future work may relax this assumption, and model the fracture energy as a "random" field, perhaps related to the spatial heterogeneity of the stress drop distribution.
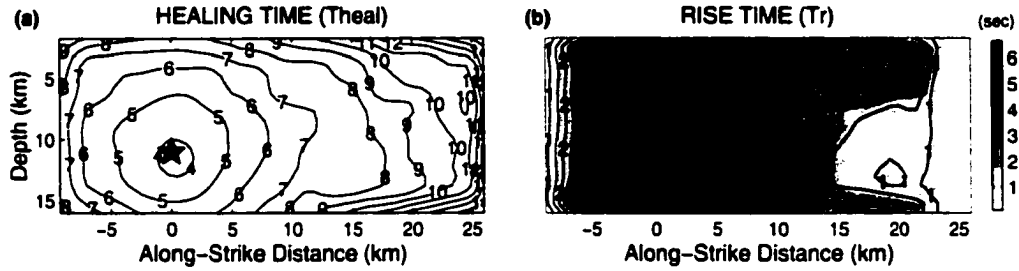
Figure 5-11: Example for the computation of variable rise time (b), based on the propagation of a healing front (a) whose contours are locally affected by regions of low stress drop.

5.5.2 Rise Time

In our dynamic simulations, the pattern of variation in the distribution of rise time over the fault (Figure 5-2) is typical for a crack model governed by a slip-weakening law [Day, 1982]. The rise time is large around the hypocenter and shortens towards the edges of the fault, with values that depend on the total rupture duration. Heterogeneity in the stress parameters adds additional variability in the typical rise time distribution, i.e. the rise time is influenced by short (compared to fault dimensions) scale lengths in the heterogeneous slip (stress-drop) distribution [Beroza and Mikumo, 1996]. In this case, regions of low stress drop may initiate local rupture healing before healing occurs from the fault edges.

In order to simulate variable rise time, τ_r, on the fault plane, we adopt the concept of a rupture healing front propagating over the rupture plane with a velocity slightly lower than the shear-wave velocity. By investigating the healing behavior of the dynamic source models (i.e. by analyzing the time when each point on the fault has stopped slipping, given by summing the rupture time and the rise time), we find that the healing front initiates at a point close to the hypocenter which stops slipping first. The rise time at each point is then simply the difference of the arrival of the healing front (t_{heal}) and the initiation of rupture (t_{rup}), $\tau_r = t_{heal} - t_{rup}$. Locally, areas of low stress drop alter the propagation of the healing phase, creating a complex pattern of rupture stopping times on the fault plane (Figure 5-11). The rise time distribution on the fault plane generated using this approach generally shows similar features to the full-dynamic rise times, though without the full-dynamic simulation we can not reproduce the details.

To quantitatively assess how well the pseudo-dynamic rise times reproduce the full-dynamic rise times, we show a similar graph as for the rupture times (Figure 5-12). Notice

Distribution of Dynamic and Pseudo-Dynamic Rise Time
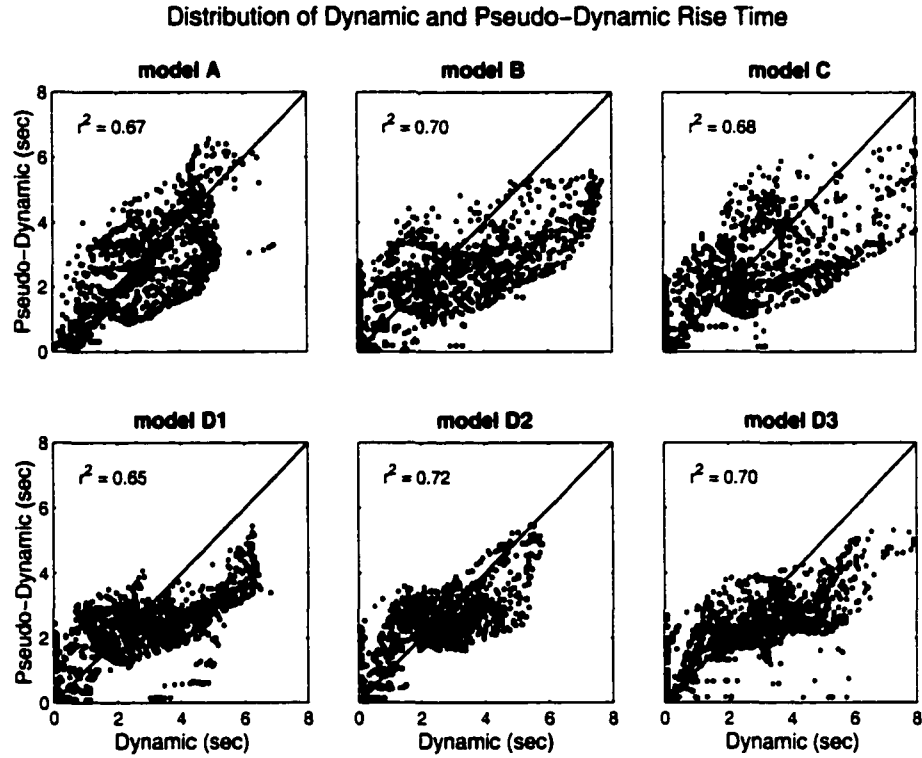
Figure 5-12: Scatter plots for *pseudo-dynamic* versus *full-dynamic* rise times for all six source models. The center line indicates where the values would fall for a perfect match; r^2 denotes the correlation coefficient.

the lower correlation coefficients, $r^2 \approx 2/3$, and the large scatter around the center line (indicating perfect match). Figure 5-13 also shows considerable differences in the marginal distributions of the full-dynamic and *pseudo-dynamic* rise times. This can only be partly attributed to the particular definition of rise time, and the fact that the full-dynamic slip-velocity functions exhibit a large degree of complexity (see next section). Most of the discrepancies of the marginal distributions for the rise time, however, is due to its insufficient characterization in the *pseudo-dynamic* source model, and future work will address this question.

5.5.3 Slip-Velocity Function

Comparing the slip velocity functions (SVF) for the four dynamic models with identical slip distribution but variable hypocenter, we find that the slip velocity functions are substantially

Distribution of Dynamic and Pseudo-Dynamic Rise Time
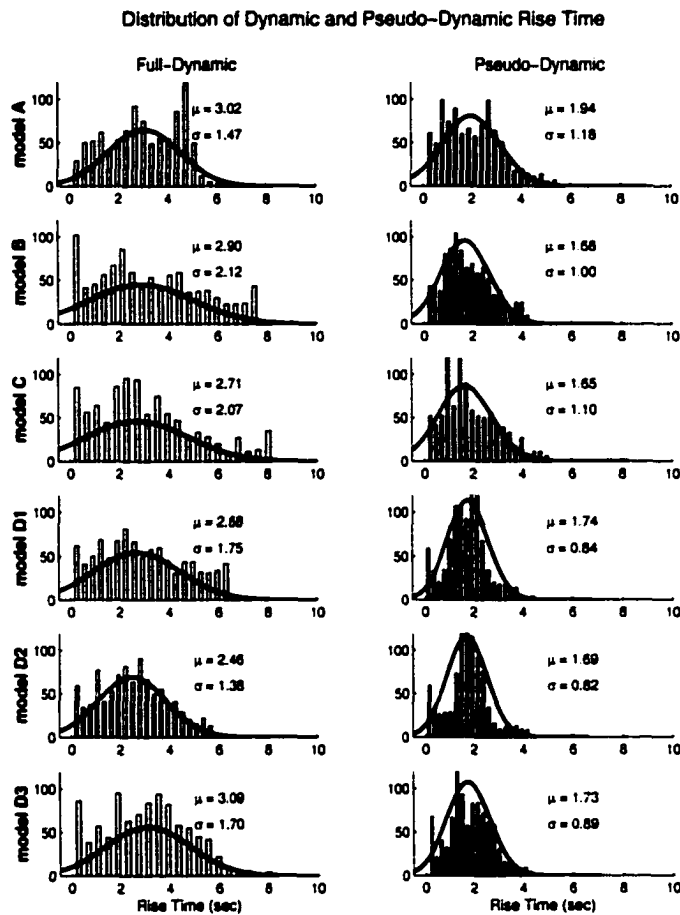
Figure 5-13: Marginal distributions for the *full-dynamic* (left) and the *pseudo-dynamic* rise times (right) for all six source models. In each panel, the population mean is given by μ, the standard deviation by σ. Note that there are considerable differences between the two distributions for a given source model.

different on the same points of the fault. The hypocentral location, which has a strong effect on directivity, also has a strong effect on the shape of the slip-velocity function. Figure 5-14 displays full-dynamic slip-velocity functions at various points along-strike for fixed depth, showing the temporal complexity of the SVF's as well as their variability with position on the fault. Large dynamic loading (at points distant from the hypocenter) has the effect of narrowing the SVF resulting in large peak slip-velocities, locally large stress drop causes similar effects. Clearly, a box-car slip-velocity function (as used in some *kinematic* strong motion simulation) is inadequate to characterize the fault behavior, whereas a truncated

Subfault Slip-Velocity Functions, Model A (along-strike, Z = 8.5 km)
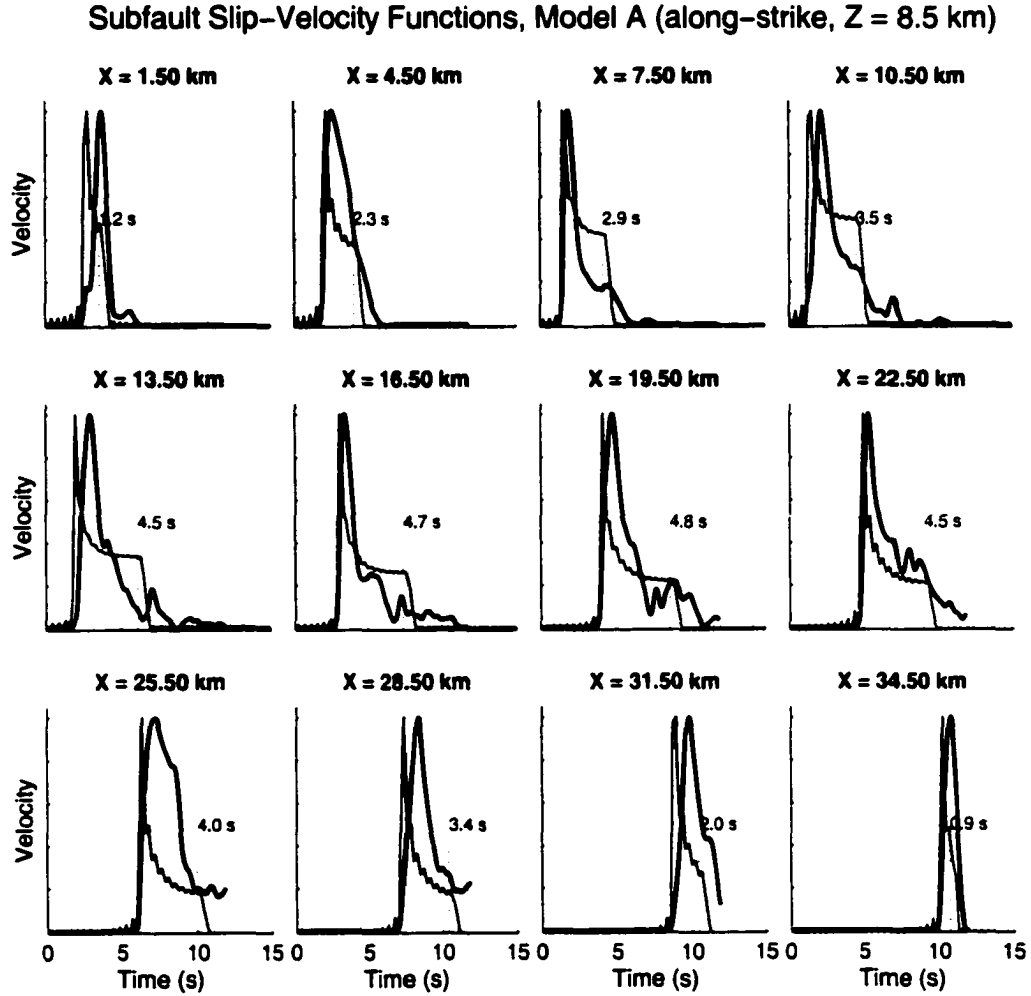
Figure 5-14: Slip-velocity functions for model A at various points along-strike (depth Z = 8.5 km). The black line depicts the full-dynamic SVF's, the gray line shows the time-domain representation of the frequency-domain approximation. The number above the dotted line indicates the rise time calculated for the full-dynamic SVF.

Kostrov function [*Archuleta and Hartzell*, 1981], overlapping triangles [*Wald et al.*, 1991] or a cosine slip function [*Cotton and Campillo*, 1995] provide a better description.

The quasi-dynamic slip-time function is given as [*Archuleta and Hartzell*, 1981]

$$\dot{s}(r,t) = C(\nu,\alpha,\beta) \cdot \frac{\sigma_e}{\mu} \cdot \beta \cdot t \cdot \frac{H(t-r/\nu)}{[t^2 - r^2/\nu^2]^{1/2}} \tag{5.4}$$

where r is the distance on the fault from the hypocenter, $C(\nu,\alpha,\beta)$ is a coefficient depending

on rupture velocity, ν, P-wave and S-wave velocity, α and β, respectively (*Richards*, 1976). σ_e is effective stress, μ is rigidity and H is the Heaviside step function. In Figure 5-14, we compare the dynamic slip-velocity functions with this quasi-dynamic slip-time function, and wobserve that the dynamic SVF's are considerably smoother, in particular at the onset, and that the quasi-dynamic approximation cannot reproduce the variability of slip-rate at later times. The smoothness of the dynamic SVF's and their variability with time and position also affect the rise time estimates. Nevertheless, the overall agreement between true dynamic slip functions and the quasi-dynamic approximation suggests that the Kostrov-type slip function is a viable choice for strong motion prediction.

In order to implement the Kostrov-like slip-velocity function into strong-motion simulation codes, a well-behaved frequency-domain representation of the quasi-dynamic slip function is needed. Based on superimposed exponential functions, *O'Connell and Ake* [1995] define a representation of (5.4) as follows

$$\dot{s}(r,t) \approx C(\nu,\alpha,\beta) \cdot \frac{\sigma_e}{\mu} \cdot \beta \cdot t \cdot H(t - r/\nu) \cdot H(-t - t_h)$$

$$\left[0.7e^{-\frac{t}{0.9a}} + 0.15e^{-\frac{t}{0.4b}} + 0.15e^{-\frac{t}{0.8b}} \right]$$

(5.5)

where a and b are the times from the onset of (5.4) until it reaches 0.5 and 0.1 of the difference between the peak-slip amplitude and the steady slip amplitudes, respectively, and t_h is the time when healing occurs. Implementation of (5.5) in the frequency domain can be done analytically (due to the exponentials), but strongly depends on the maximum frequency and the frequency discretization. The approximation shown in Figure 5-14 (gray lines) are computed for the frequency range of our strong-motion simulations ($f = 0-2.3$ Hz, $df \approx 0.015$ Hz, $Nf \approx 150$). The numerical noise due the limited frequency bandwidth is evident in the Kostrov-like approximations, but its effect on the resulting ground motions is negligible.

5.6 Strong Motion Simulation for Pseudo-Dynamic Source Models

Using the *pseudo-dynamic* source characterization, we calculate strong ground motions for the six source models A-C, D1-D3, at the locations in Figure 5-4. In these simulations,
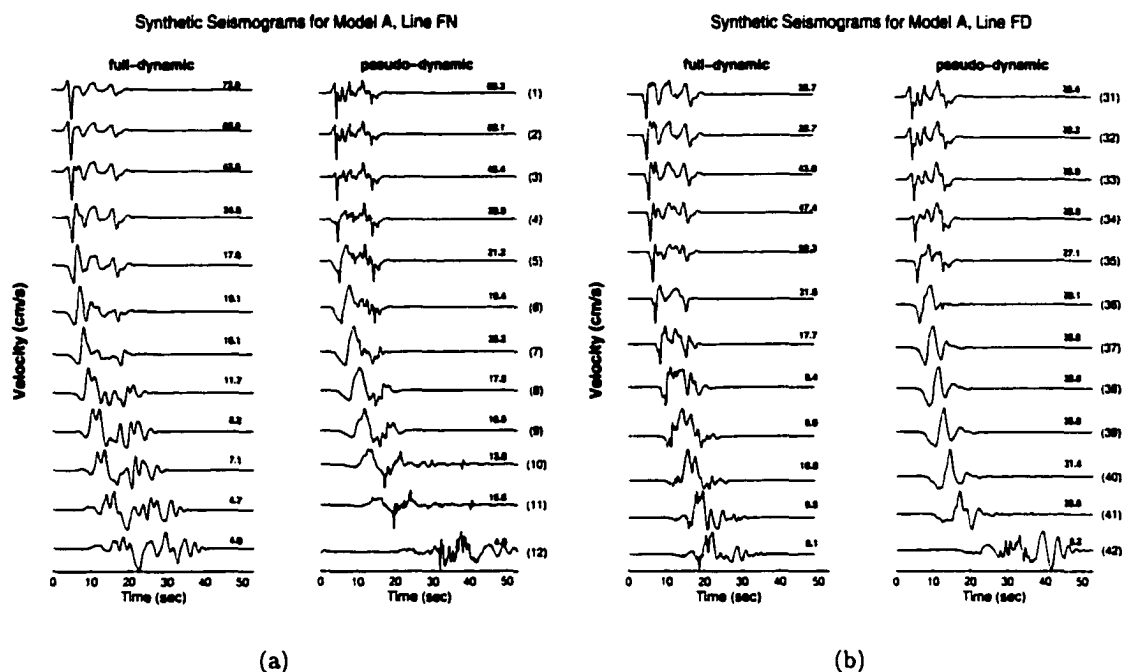
Figure 5-15: Velocity seismograms for the full-dynamic and the *pseudo-dynamic* source characterization of model A. Numbers on each time series denote the peak ground velocity (*PGV*), numbers
in brackets refer to the observer distribution (Figure 5-4). (a) Fault-normal line, observers 1–12;
(b) Fault-diagonal line, observers 31–42.

rupture velocity and rise time fluctuate on the fault plane, and we deploy the approximate Kostrov-like spectral representation of the slip-velocity function. Figure 5-15 shows
full-dynamic and *pseudo-dynamic* velocity seismograms (in cm/sec) for the fault-normal
(FN) stations (1-12) and for the fault-diagonal (FD) stations (31-42). The waveforms are
similar in the extreme near-source region ($R \leq 5\,\mathrm{km}$), but the *pseudo-dynamic* simulations
appear to be richer in high-frequency seismic energy. At larger distances ($R \geq 10\,\mathrm{km}$), the
waveform similarities decrease as the *pseudo-dynamic* seismograms become rather simple
two-sided velocity pulses while the full-dynamic seismograms exhibit a considerable seismic-
coda. Nevertheless, we find rather good agreement among the *PGA*-values. It is important
to note that we have made no attempt to "match" the *pseudo-dynamic* seismograms with
the full-dynamic ones by optimizing the *pseudo-dynamic* source model. Particularly the
details of the dynamic slip-velocity (e.g. gradual onset, multiple slip episodes, slip at later
times, gradual tapering to zero) cannot be reproduced by our SVF-approximation, and
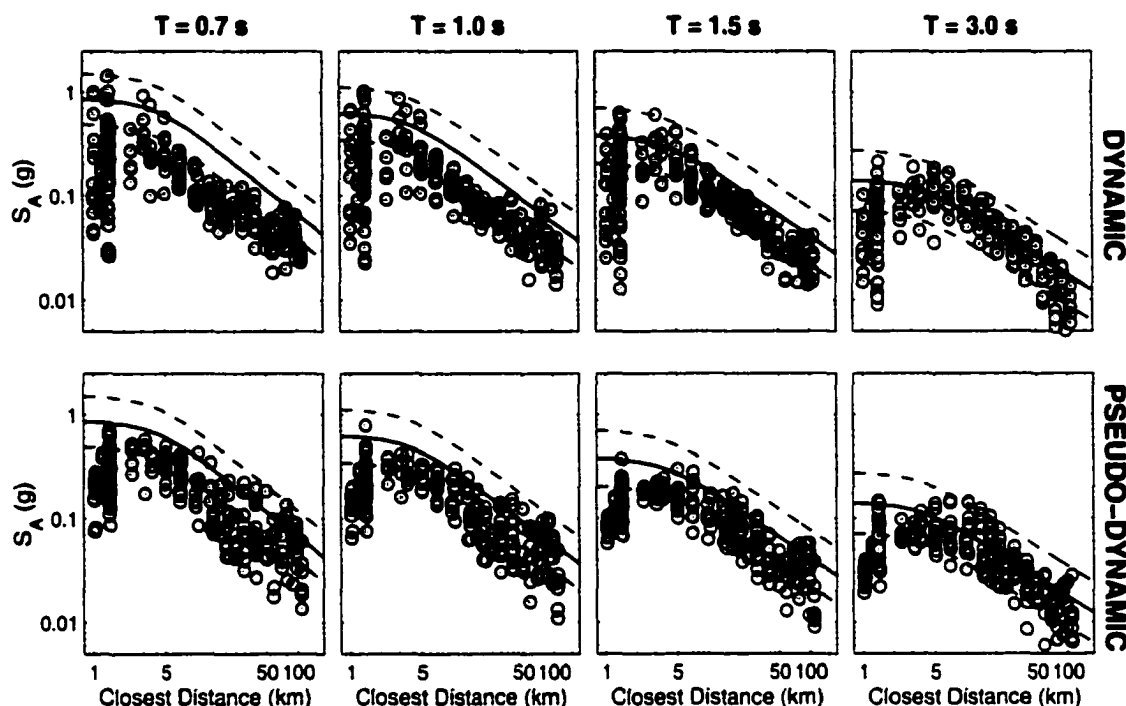
Figure 5-16: Simulated and empirical average-horizontal spectral acceleration (*Abrahamson and Silva*, [1997], solid line; dashed line indicates standard deviation) for $M = 7$ strike-slip earthquakes. The simulated values were obtained for source models A-C, D1-D3, for both the *dynamic* and *pseudo-dynamic* approach. Only non-nodal stations are shown (see text).

hence differences in the seismograms are expected.

To further explore the capabilities of the *pseudo-dynamic* source model for strong motion prediction, we calculate response spectra (5 % damped), displayed in Figure 5-16. The top row shows again the full-dynamic spectral responses (Figure 5-6). The *pseudo-dynamic* simulations (bottom row) reproduce the dynamic reponse-spectral amplitudes well, and show a distance-decay which is comparable to both the dynamic simulations as well as the empirical attenuation model. Comparing the *kinematic* and *pseudo-dynamic* spectral responses in Figures 5-16 and 5-6, respectively, illustrates the performance difference of the *pseudo-dynamic* and the *kinematic* source characterization for strong motion prediction. The *kinematic* simulations exhibit large discrepancies to both the dynamic and the empirical spectral responses. In contrast, the *pseudo-dynamic* simulations appear to be able to reproduce the spectral decay and amplitudes, indicating that an improved *pseudo-dynamic* source characterization may be able to reproduce full-dynamic seismograms.
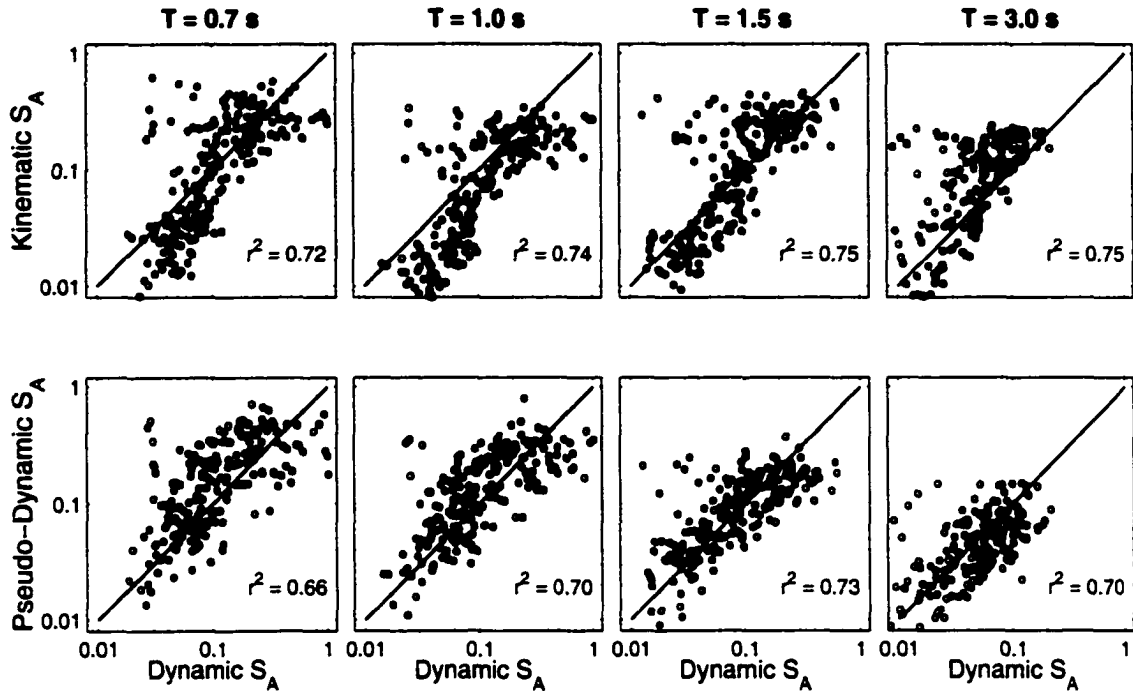
Figure 5-17: Scatter plots of spectral acceleration S_A, showing the relation between the *kinematic* and the dynamic simulations (top) as well as the relation between the *pseudo-dynamic* and the dynamic simulations (bottom).

It is interesting to note, however, that there is not necessarily a one-to-one correspondence between the full-dynamic and *pseudo-dynamic* seismograms, and hence response spectra. Figure 5-17 displays scatter plots that show the relations between the *kinematic* and dynamic spectral responses (top), as well as the relation between the *pseudo-dynamic* and the dynamic S_A. The correlation coefficients are very similar in all cases, and there is no clear indication that the *pseudo-dynamic* simulations correlate better statistically with the dynamic simulations than with the *kinematic* simulations. The data for the *kinematic* simulation, however, suggest a linear trend with slope larger than 1, indicating a bias of the *kinematic* spectral values, which is not present for the *pseudo-dynamic* simulations. Apparently, the good agreement between the *pseudo-dynamic* and the full-dynamic spectral responses in Figure 5-16 does not follow from individual seismograms, but rather from the statistical properties of the simulations. As pointed out already, the differences in the dynamic and *pseudo-dynamic* source characterization are still significant, and hence likewise for the calculated seismograms.
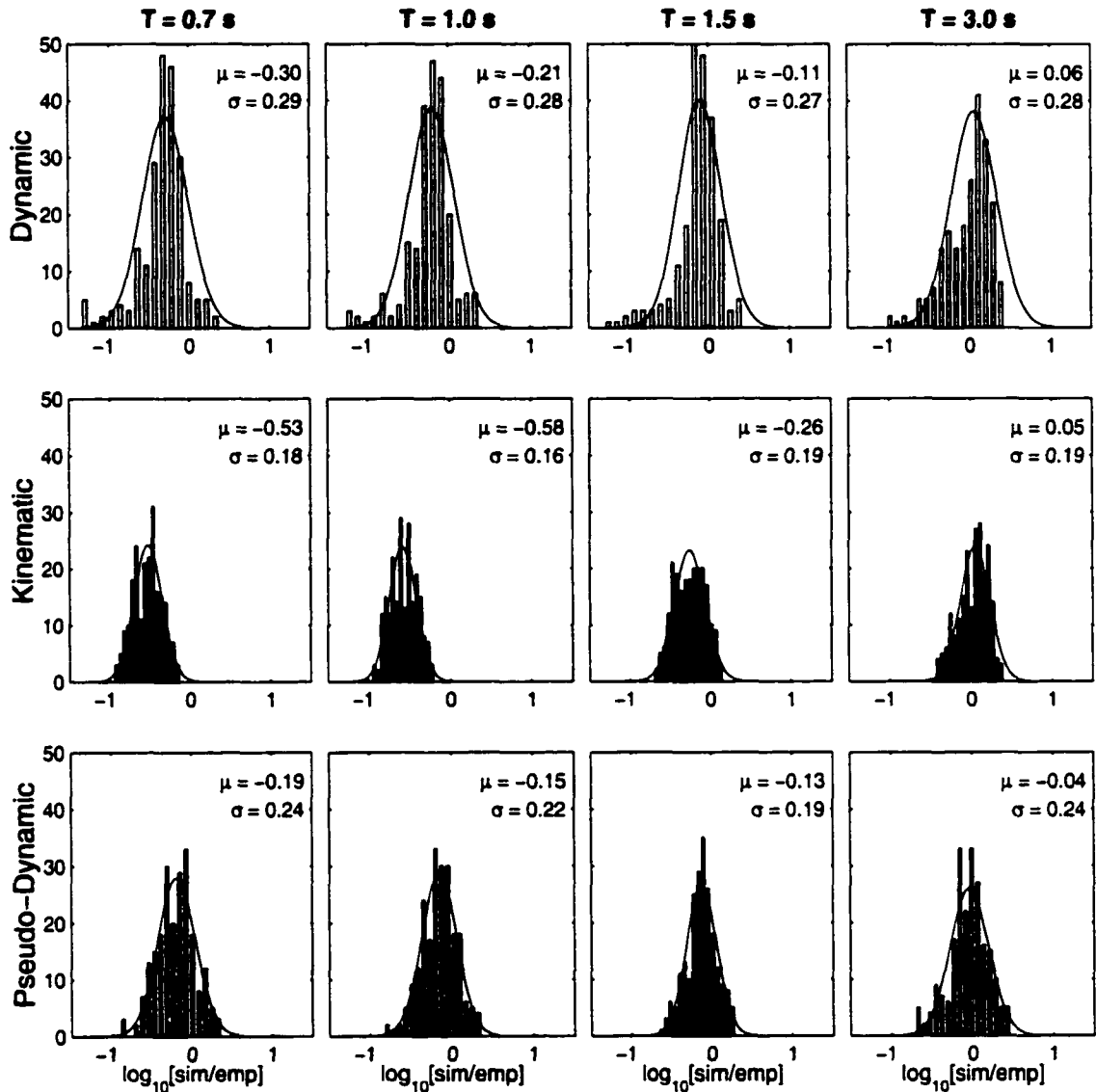
Figure 5-18: Bias of spectral acceleration S_A at different periods T for the three source characterizations. A zero-mean distribution with small standard deviation, $N(\mu = 0, \sigma)$, would indicate that the simulations are unbiased with respect to the empirical attenuation relation [*Abrahamson and Silva*, 1997].

Figure 5-18 summarizes the performance in strong motion prediction of the three earthquake source models with respect to the empirical attenuation models. Since the empirical relationships are based on strong motion recordings, though sparse at short distances, any procedure to simulate ground motion intensity must be validated against these observations.

We chose to calculate the bias of the simulated spectral values with respect to the predicted (empirical) S_A [*Abrahamson and Silva*, 1997], by computing

$$bias = \log_{10}\left(\frac{S_A^{sim}}{S_A^{emp}}\right),$$

(5.6)

where S_A^{sim} denotes spectral acceleration for the simulated ground motions, and S_A^{emp} indicates spectral acceleration from empirical relationships. In (5.6), larger-than-empirical spectral values have a positive bias, while smaller-than-empirical spectral values are negatively biased. The histograms displayed in Figure 5-18 reveal that the biases are normally distributed, with mean μ and standard deviation σ indicated in each panel. The *kinematic* simulations (center row) are clearly negatively biased (exception for $T = 3\,\text{s}$), showing that the *kinematic* source model results in too low ground motion estimates. The dynamic (top row) and the *pseudo-dynamic* source models (bottom row) are similarly biased in that spectral level are somewhat underpredicted for shorter periods ($\mu \approx -0.25$ for $T = 0.7, 1.0\,\text{s}$), but that the bias decreases for longer periods. Note, however, that the distributions of spectral values for the dynamic simulations are left-tailed, i.e. a considerable amount of spectral values are severely underestimated with respect to the empirical model. Figure 5-16 indicates that this is the case for the very short distances. It remains unclear whether this is an artifact of our simulations, but there is evidence from recent large earthquakes (Chi-Chi (Taiwan), Izmit (Turkey)) that ground motions in the extreme near-field are not as large as predicted from empirical relations.

5.7 Discussion

The comparison of the kinematic and dynamic strong motion simulation approaches allows us to infer how specific source characteristics affect the predicted response at various periods. The systematic large spectral amplitudes of kinematic simulated responses at long periods reflect the strong coherency of energy release as the rupture propagates along the fault. The kinematic source models have high coherency due to homogeneous rupture velocity and a uniform slip-velocity function, while the variability in both these parameters in the dynamic models diminishes the coherent energy release during rupture.

Introducing spatial and temporal heterogeneity tends to increase peak ground motion amplitudes at short periods ($T < 2\,\text{s}$), visible in the larger spectral amplitudes obtained

from dynamic models with respect to those calculated from kinematic models. Including variability in all the relevant source parameters, such as slip, rupture velocity and slip-velocity function, reduces the occurrence of systematic differences between the simulated ground motions and the observed values. Obtaining the spatially variable source parameters through dynamic modeling, however, is costly and time consuming, and hence is not a viable approach to generate many realizations of a scenario earthquake. We have therefore developed a pseudo-dynamic characterization of the earthquake source that approximates the dynamic calculations.

In our pseudo-dynamic earthquake source model, we compute distributions of variable rupture velocity based on (5.3), relating stress drop, fracture energy and crack length [*Andrews*, 1976a]. Strictly speaking, this expression is only valid in simple anti-plane strain with uniform stress drop and frictional properties, but it appears to be useful also for 3D complex rupture. The resulting rupture times show comparable behavior as in the dynamic models, i.e. fast rupture propagation over regions of high stress drop and slow rupture propagation in areas of low stress. We also find good agreement between the the *pseudo-dynamic* rupture times and the *dynamic* ones on a point-by-point basis. We want to emphasize, however, that each distribution of rupture velocity is non-unique (depending on the assumed fracture energy), and should be treated as a possible realization of the rupture propagation that does not directly consider other impediments to rupture such as geometric irregularities (fault curvature, jogs, bends).

Likewise, the distribution of rise times calculated in our pseudo-dynamic earthquake source model only represents one realization out of many possibilities for a given stress drop. Nevertheless, defining local rise time through the propagation of a healing front over the rupture plane is a useful approach to generate realistic rise time distributions. Comparing the rise time on a point-by-point basis, we note that the *full-dynamic* rise times tend to be larger, in particular, in the range $\tau_r > 3\,\text{sec}$. We attribute this discrepancy to our simplified model for calculating rise time, and to the nature of the *full-dynamic* slip-velocity functions which are smooth and may show multiple slip episodes or significant slip at later times. It is important to note that we have made no attempt to optimize the *pseudo-dynamic* rupture velocities or rise times based on the dynamic model. Our *pseudo-dynamic* characterization is meant only to capture the gross features of the dynamic rupture, and future research may address this issue in more detail.

The implementation of the Kostrov-like, quasi-dynamic slip-velocity function marks perhaps the most significant advancement in the *pseudo-dynamic* source model. Informal sensitivity tests indicate that using a box-car or exponential slip-velocity function, together with variable rise time and rupture velocity, is not able to reproduce the *dynamic* ground motion intensity, and that only the introduction of the quasi-dynamic slip-velocity function remedies this discrepancy. The sharp initial increase to large peak slip-velocities, the subsequent $\frac{1}{t}$-decay, and the sharp stopping phase (generating high-frequency seismic energy [*Madariaga*, 1983]) of the quasi-dynamic slip-velocity function contributes to the qualitative and quantitative good correspondence between the full-dynamic and *pseudo-dynamic* ground motions. As seen in Figure 5-15, the *pseudo-dynamic* source model model tends to generate more high-frequency energy than the full-dynamic source model, mostly due to the particular choice of the slip-velocity function. Initial tests of tapering the high-frequency contributions of the slip-velocity function (due to the sharp initial onset and the rather abrupt healing) had only minor effects. A more significant improvement of the *pseudo-dynamic* slip-velocity function is perhaps achieved by adding a more gradual initial onset and a smoother stopping behavior, as for instance suggested in the time-domain slip-function of *Nakamura and Miyatake* [2000].

In contrast to the *kinematic* simulation, the strong ground motion simulations for the *pseudo-dynamic* source characterization are able to reproduce the response-spectral values and distance-decay of both the full-dynamic calculations as well as the empirical predictions. The missing one-to-one correspondence between response-spectral values for the *full-dynamic* and the *pseudo-dynamic* approach (Figure 5-17) is attributable to the approximate nature of the *pseudo-dynamic* model, but Figure 5-18 shows that the statistical properties and the bias (with respect to the empirical predictions) of ground motions based on the *pseudo-dynamic* model are comparable to those using the full-dynamic source model, while the *kinematic* ground motions are clearly inadequate.

Both the full-dynamic as well as the *pseudo-dynamic* simulations show lower-than-empirically-predicted spectral amplitudes for the very near-source sites. Recent large earthquakes (Chi-Chi (Taiwan), Izmit (Turkey)) do exhibit a similar effect in that ground motions in the extreme near-field were lower than predicted by empirical relations. As already discussed, these observations can only partly be attributed to the radiation pattern. A more likely explanation is that the details of the dynamic rupture process generate such low ground motions, for instance low peak-slip velocities in shallow parts of the fault, associated

with low rupture velocities. Moreover, for large earthquakes with large source dimensions, the center of high moment-release may be far away from a given observer, while the surface projection of the fault plane may still indicate a near-field site. Ground motions for such a location may be small (due to large "effective" distance, $R_{centroid}$), but empirical ground motion estimates would not be able to predict such behavior. Further research will address this issue by focusing on strong motion simulation in the extreme near-field ($R \leq 5$ km), using a dense observer distribution and many realizations of scenario earthquakes for a range of magnitudes.

5.8 Conclusions

The *pseudo-dynamic* source characterization represents a significant advancement over the standard *kinematic* source models for strong motion prediction. In this model, rupture velocity, rise time and the slip-velocity function are allowed to vary both spatially and temporal. Despite some deficiencies in the current characterization of the rise time, and a spiked, high-frequency generating slip-velocity function, the resulting ground motions are comparable to full-dynamic simulations. Since response-spectral levels are in general agreement with empirical predictions, the *pseudo-dynamic* source characterization may be used to efficiently generate realistic, *dynamically-consistent* strong ground motion seismograms, even for many realizations of scenario earthquakes. These simulated strong motion time histories can then be used in performance-based engineering and Probabilistic Seismic Demand Analysis (PSDA) in which entire time series are needed to model dynamic, non-linear multi-degree-of-freedom structures [*Luco*, 2001a]. Further research will attempt to improve the parametrization of spatially variable rise time, and will address a better characterization of the slip-velocity function.

5.9 Acknowledgments

The dynamic rupture modeling in this chapter was carried out by Patti Guatteri, and I have greatly benefitted from her enthusiasm for this study, her ideas and comments. J. Boatwright helped initialze this project and to define its goals. Kinematic and pseudo-dynamic seismograms were calculated using the COMPSYN-package [*Spudich and Xu.*, 2002].

Chapter 6

Strong Motion Simulation for Earthquake Scenarios on the Hayward-Rodgers Creek Fault System

6.1 Abstract

In this chapter I use the previously described earthquake source models to perform strong motion simulations for earthquake scenarios on the Hayward-Rodgers-Creek fault system. Ground motions are calculated at six prominent sites using both the *kinematic* and the *pseudo-dynamic* source characterization, thus enabling me to compare both sets of simulations with predictions from empirical attenuation relations. The strong motion time series can not only be used to characterize the variability of source effects in the near-field of large earthquakes, but also in performance-based engineering in which structures are modeled as dynamic multi-degree-of-freedom systems[1].

6.2 Introduction

The previous chapters have introduced earthquake source models with increasing complexity. In Chapter 2 I discussed scaling relations among the fundamental source parameters, length, width, mean slip and seismic moment, before I turned to characterize the variability of slip on the fault plane (Chapter 3). While proper scaling relations are important in the application of empirical attenuation models, simulating realistic slip complexity is essential in defining an appropriate *kinematic* source model for strong motion calculations.

---

[1] Luco, N., P.M. Mai, G.C Beroza, and C.A. Cornell, *7th U.S. National Conference on Earthquake Engineering*, Boston (July 2002), in review.

Site Locations and Bay Area Faults
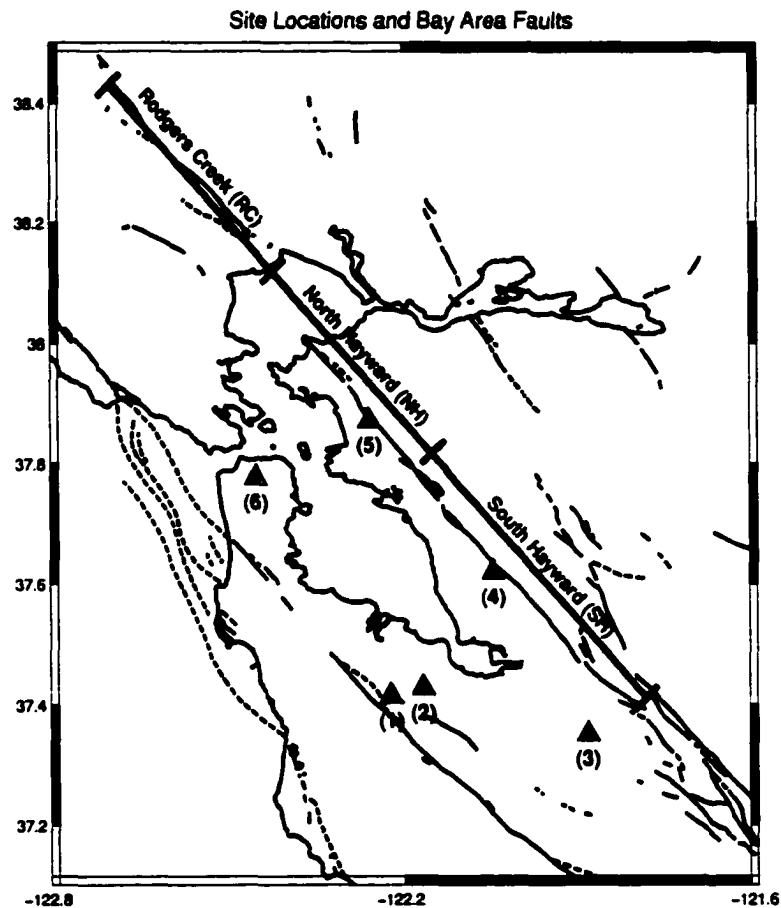
Figure 6-1: Fault map of the San Francisco Bay Area (California). Site locations for strong motion simulation are indicated by triangles. The straight-line fault-trace approximation for the Hayward-Rodgers Creek fault system is shown by the thick line, separated into three distinct segments.

Using *kinematic* source models I computed ground motions for two scenarios of **past** earthquakes, first for model validation, and second to develop a hybrid method for calculating near-source broadband seismograms (Chapter 4). Chapter 5 introduces a *pseudo-dynamic* source characterization that allows for spatially variable rupture velocity, rise time and a more realistic slip-velocity function. Applying the *pseudo-dynamic* approach for a "generic" scenario earthquake of $M_w = 7.0$, I find that it yields more realistic ground motions than the *kinematic* model. In this chapter I turn my attention to ground motion simulation for scenarios of **future** earthquakes.

The scenario earthquakes occur on the Hayward-Rodgers Creek fault system, east of

Table 6.1: Site locations for strong ground motion simulations in the San Francisco Bay Area for scenario earthquakes on the Hayward-Rodgers Creek fault system (Figure 6-1).

No.	Longitude	Latitude	Closest Distance [in km]			Location
			SH	NH	RC	
1	122.2221° W	37.4145° N	33.06	48.95	78.42	SLAC, Stanford
2	122.1669° W	37.4275° N	27.67	47.39	78.51	Hoover Tower, Stanford
3	121.8889° W	37.3517° N	16.72	66.15	100.89	Downtown San Jose
4	122.0481° W	37.6194° N	4.31	31.07	65.91	BART station, Union City
5	122.2578° W	37.8722° N	7.11	3.56	29.07	Campanile, Berkeley
6	122.4494° W	37.7769° N	29.58	26.90	35.20	USF, Main Campus

the San Francisco Bay, California, and I calculate ground motion at six prominent sites (Figure 6-1), listed in Table 6.1, each with the same one-dimensional velocity structure (Table 6.2) which does not contain anelastic attenuation. The complex faulting pattern of the three segments, comprising bends, step-overs and short branching faults, is approximated with a single continuous fault trace. The magnitude and source dimensions of each segment, or combination of segments, is adopted from the *WorkingGroup99* report on earthquake probabilities in the San Franciso Bay [*WorkingGroup99*, 2000]. Table 6.3 lists the source characteristics as well as the median rise time for each scenario, calculated following *Somerville et al.* [1999]. For each of the six possible combinations of fault segments, I generate 30 realizations of spatially variable slip [*Mai and Beroza*, 2001a], where the magnitude and rise time are randomized (using a normal distribution) with the given standard deviation (Table 6.3). This set of 180 simulated earthquakes spans a length range from 35 km to 150 km, and magnitudes range $6.38 \leq M \leq 7.61$, about two orders of magnitude in terms of seismic moment, M_o.

The results of the *kinematic* and *pseudo-dynamic* strong ground motion simulations indicate that ground motion amplitudes and their variability is well represented for the *pseudo-dynamic* simulations,but occasionally, *PGV*- and *PGA*-values are extremely large. In contrast, the *kinematic* simulation exhibit less variability, and also lower ground motion levels. The Fourier amplitude spectra of the *pseudo-dynamic* and *kinematic* simulations exhibit considerable differences in terms of spectral decay and the presence of spectral

Table 6.2: Simplified one-dimensional velocity-density structure in the Bay Area (modified after *Boore and Joyner* [1997]) used for the Hayward-Rodgers Creek simulations.

Depth [km]	v_p [km/s]	v_s [km/s]	Density [g/cm^3]
0.00	3.00	1.60	2.36
1.25	3.50	1.90	2.36
4.75	5.20	2.75	2.47
5.75	5.70	3.10	2.62
6.60	6.30	3.65	2.80
16.80	6.65	3.80	2.85
18.40	7.00	4.10	3.00
22.80	7.05	4.12	3.00
24.10	8.00	4.50	3.20
80.00	8.10	4.68	3.30

holes, indicating that the *pseudo-dynamic* simulations provide a more realistic spectral behavior of the strong ground motion. Comparing response spectra for both simulation approaches to empirical attenuation relations [*Abrahamson and Silva*, 1997], I find that the *pseudo-dynamic* simulations roughly agree with the empirical predictions over the limited frequency band of our calculations ($0 \le f \le 1.8$ Hz) whereas the *kinematic* simulations are clearly inadequate in reproducing empirical attenuation relationships. The *pseudo-dynamic* ground motions have larger response-spectral variability than the empirical predictions, with spectral accelerations at $T = 1$ sec of up to 3 g! For some of the source realizations, I also observe unrealistically large *PGV*-values, indicating some deficiencies in our simulation approach, perhaps due to not-accounted for anelastic attenuation and Earth structure, but more likely due the *pseudo-dynamic* source characterization. I conclude by discussing possible ways for improving the *pseudo-dynamic* model.

6.3 Earthquake Source Models

In this study, we base the source dimensions and the magnitude of each event on the recent report of earthquake probabilities in the Bay Area [*WorkingGroup99*, 2000]. Table 6.3 lists the median magnitude and its standard deviation, the length and width of each segment

Table 6.3: Mean annual rates, rupture areas, mean moment magnitude, and median *average* rise time [*Somerville et al.,* 1999] for six potential rupture sources on the Hayward-Rodgers Creek fault system (Figure 6-1).

Rupture Source	Mean Rate [1/yr]	Area $W \times L$ [km^2]	Mean M_w	S.Dv. M_w	Median τ_r [sec]	S.Dv. τ_r [sec]
SH	2.69×10^{-3}	12×52	6.88	0.16	1.11	0.41
NH	2.58×10^{-3}	12×35	6.63	0.12	1.01	0.36
RC	3.49×10^{-3}	12×64	7.06	0.13	1.36	0.42
SH + NH	1.91×10^{-3}	12×87	7.08	0.14	1.51	0.34
NH + RC	0.51×10^{-3}	12×98	7.21	0.12	1.72	0.45
SH + NH + RC	0.22×10^{-3}	12×150	7.37	0.13	2.19	0.67

(or combinations thereof) as well as the median rise time as calculated following *Somerville et al.* [1999]. Figure 6-2 illustrates the distribution of magnitudes and mean slip for all realization; the distributions of maximum displacement are computed from the actual slip realization, showing peak slip values of up to 10 m for the largest magnitudes.

Slip distributions for each scenario earthquake are generated following *Mai and Beroza* [2001a] (Chapter 3), using the *von Karman* auto-correlation function and correlation lengths that increase with increasing seismic moment. For the cases where multiple segments are assumed to rupture in a single earthquake, we generate the slip distribution for the entire rupture length (i.e. combined segments). Alternatively, one could simulate slip distributions for each segment only, and than combine those individual smaller earthquakes to multi-segment ruptures. This approach implies that segment boundaries are strong barriers in which no slip occurs, yet rupture does not stop at the barriers, but instead propagates across. Large stress changes would occur at these barriers, while the peak-slip amplitudes within each segment would have to be rather large in order to accommodate the seismic moment. Though this approach is perfectly valid, we have chosen to treat multi-segment ruptures as an entity in order to have better control over the slip simulations and to avoid arbitrary "patching" of segment-based slip distributions.

It remains to specify the hypocenter locations for each rupture realization. Since we generally do not know *a priori* where the hypocenter in a future earthquake will be, we randomize hypocentral position. Moreover, a given fault segment may start rupturing from either side, i.e. there is no reason to assume that any direction is preferred. There are,
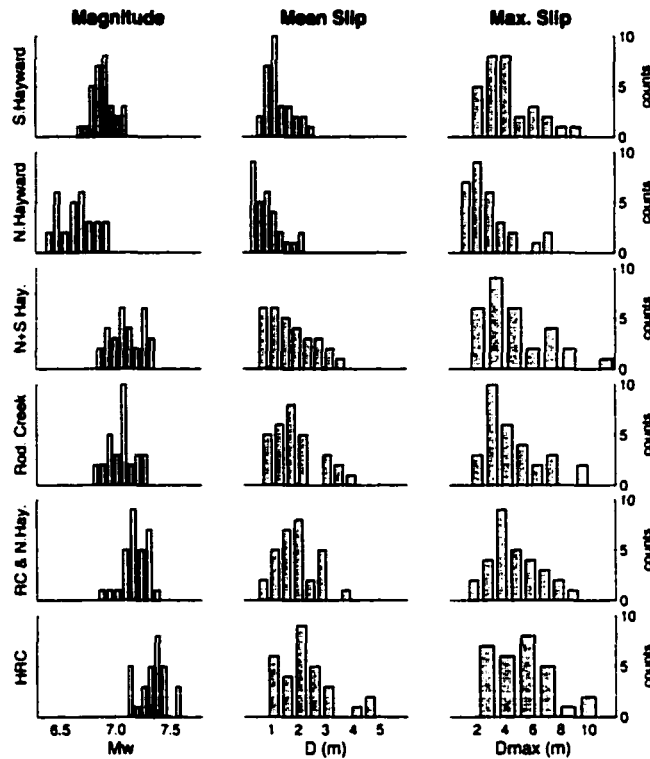
Figure 6-2: Distributions of magnitude (left column), mean slip (center) and maximum slip (right column) for 30 earthquake realization on each fault segment. The median and standard deviation of the magnitude distributions are constrained by *WorkingGroup99* [2000].

however, two important observations that we use to constrain the hypocentral location. First, it has been noted that earthquakes tend to nucleate in the deeper portions of the seismogenic zone, and that only very few earthquakes started rupturing at shallow depth (famous example is Landers where the hypocenter was at 4-5 km depth). Based on this and results shown by *Somerville et al.* [1999], we use a truncated log-normal distribution for the depth-distributions of hypocenters (Figure 6-3, right column). Secondly, we constrain the along-strike position based on the observed predominance of unilateral rupture [*McGuire et al.*, 2001], i.e. it is more likely that the rupture nucleates close to either end of the fault. We therefore randomize the horizontal hypocenter location based on a bimodal distribution whose density changes gradualy from low at the fault edges, to high at about $L/4$, decreasing again towards the fault center, and then increasing again at roughly $3L/W$. Figure 6-3 (left) illustrates the randomized horizonal hypocenter positions.
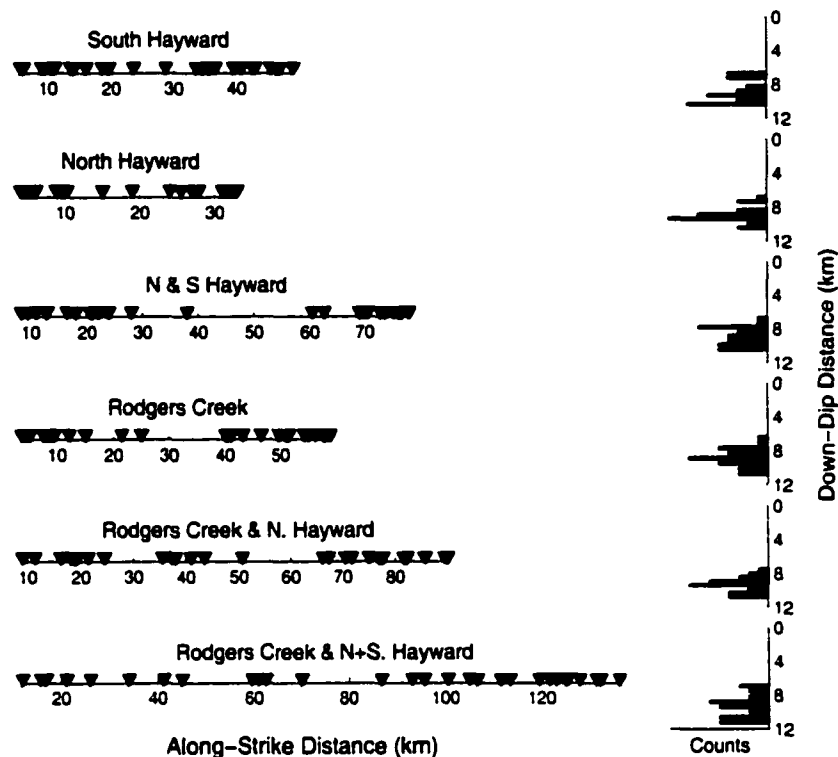
Figure 6-3: Distribution of hypocenters on each fault segment, in along-strike (left, as scatter plot) and down-dip direction (right, as histogram). See text for details.

6.4 Ground motion simulation

In order to compute ground motions for these scenario earthquakes, at the locations displayed in Figure 6-1, I use both the *kinematic* approach and the *pseudo-dynamic* source characterization. Based on a vertically layered Earth model (Table 6.2), but not accounting for anelastic attenuation, velocity seismograms for both types of source models are calculated using the COMPSYN-package by *Spudich and Xu* [2002]. Their passband is limited to $0 \leq f \leq 1.8$ Hz. We can thus compare the resulting ground motion intensities, waveform characteristics, and spectral properties of the simulations to evaluate the suitability of the simulated ground motions for strong motion prediction, and eventually subsequent Probabilistic Seismic Demand Analysis (PSDA).

6.4.1 Kinematic Source Models

In the kinematic models, rupture velocity ν is constant over the rupture plane, with values of about 85 % of the shear-wave velocity. In fact, ν for each realization is drawn as a random sample from a normal distribution, centered at $\nu = 0.85$, with a standard deviation $\sigma_\nu = 0.1$. A similar approach is taken to determine the rise time τ_r, uniform for over the fault for source realization. We compute the median rise time (Table 6.3) based on the relations by *Somerville et al.*, [1999]. An informal regression on their data shows that the standard deviation of the rise time is about 40 % in log-units [*Luco, personal communication*]. We then find the rise time for each realization again as a random sample from a normal distribution around the median τ_r with a standard deviation of 40 %. The slip-velocity function on each point is a box-car function of length (duration) τ_r. The motivation for randomizing rupture velocity and rise time in this manner is that we cannot estimate their exact values *a priori*, but we can put some physical bounds on their values. Moreover, this kind of randomization of source parameters could potentially be included in Probabilistic Seismic Hazard Analysis (PSHA), simply by adding another term to the hazard integral.

6.4.2 Pseudo-Dynamic Source Models

We use the methodology outlined in Chapter 5 to generate the corresponding *pseudo-dynamic* source characterization for each *kinematic* source model. In this approach, spatially variable rupture velocity is computed using (5.3), and the rise time is determined by a propagating healing front which initiates close to the hypocenter. It is important to note that we use the algorithms as described in Chapter 5, and that we made no attempt to modify or optimize the *pseudo-dynamic* approach for the present application. Particularly for the longest ruptures, we obtain rather short rise times (compared to more common estimates) and rupture times that reflect a very complicated rupture propagation. Future research may address the issue of magnitude dependence and/or aspect-ratio dependence of the *pseudo-dynamic* source model.

6.4.3 Waveform and Fourier-spectral characteristics

Figure 6-4 compares velocity seismograms (black) for the *pseudo-dynamic* (left) and the *kinematic* (right) source models at six observer locations for a scenario earthquake on the South Hayward fault. Acceleration time series are shown in gray (on reduced amplitude

Source SH-19, M = 6.83 (fault-normal)
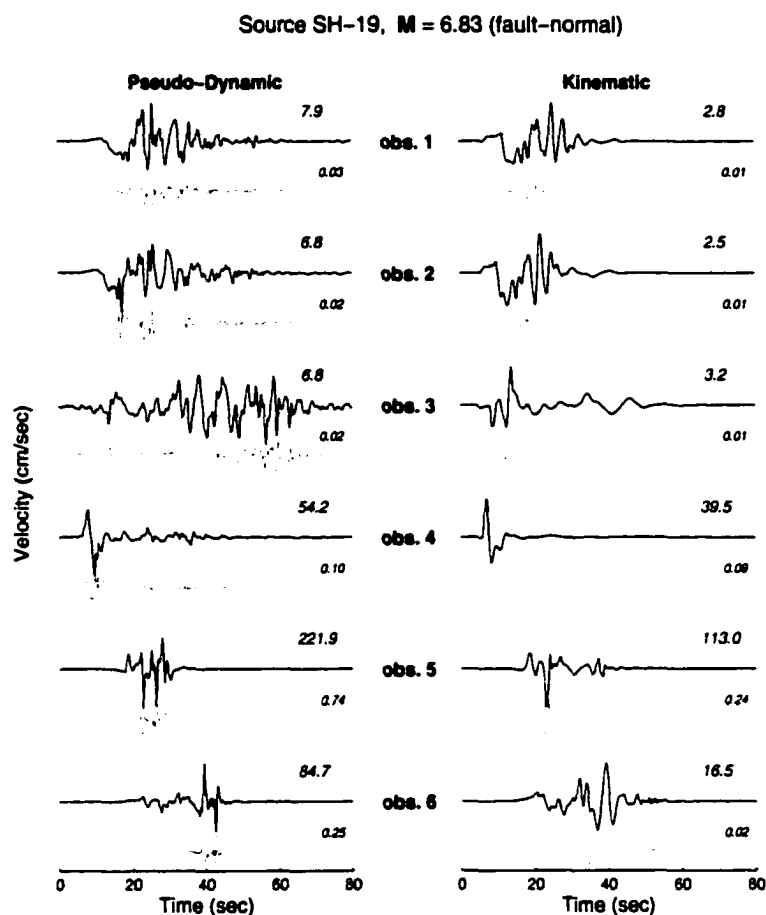
Figure 6-4: Synthetic seismograms at six observer locations for a simulated M = 6.83 earthquake on the South Hayward segment. The left column displays the *pseudo-dynamic* simulations, the right column the corresponding *kinematic* seismograms. Velocity seismograms are shown in black, with *PGV* indicated by the larger number. Accelerograms (gray lines) are displayed on a reduced amplitude scale, with *PGA* (in g) denoted by the smaller number.

scale). Note the similarity among the *pseudo-dynamic* and *kinematic* velocity waveform at each site. The *pseudo-dynamic* ground motions, however, have larger peak amplitudes (denoted by the numbers at each trace), and contain significantly more high-frequency energy (see also Figure 6-5). Particularly intruiging are the ground motions at site 3 for this earthquake realization. While *kinematic* synthetics show insignificant later arrivals, the later phases in the *pseudo-dynamic* seismograms are actually dominant, both in terms of amplitude and duration, indicating that the directivity effects in the backward direction of rupture propagation are enhanced for the *pseudo-dynamic* source models.

Source SH-19, M = 6.83 (fault-normal)
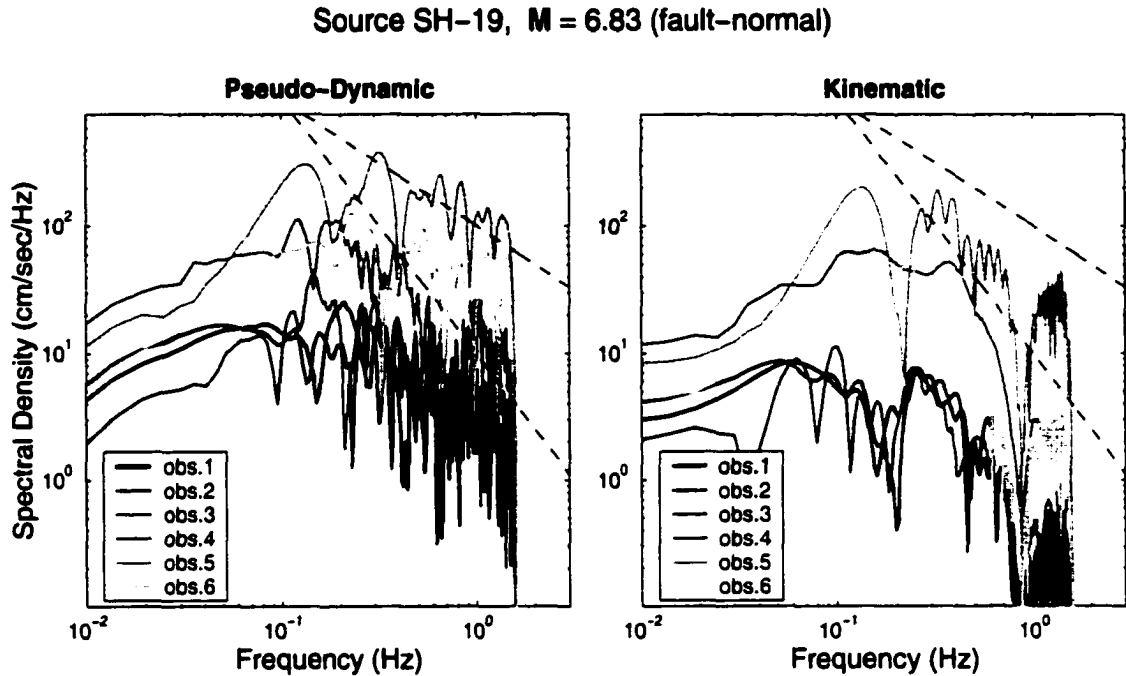
Figure 6-5: Fourier amplitude spectra for the velocity seismograms displayed in Figure 6-4. The broken lines indicate an ω^{-1}- and ω^{-2}-decay, respectively.

The Fourier amplitude spectra depicted in Figure 6-5 show two important differences among the *pseudo-dynamic* and *kinematic* simulations. First, we observe that the *pseudo-dynamic* velocity seismograms decay roughly as ω^{-1} (indicated by the upper broken line), while the *kinematic* seismograms appear to decay faster, and hence may not be consistent with the generally observed ω^{-2}-model for far-field displacement spectra. The amplitude spectra for the *kinematic* synthetics also display a distinct notch at $f \approx \frac{1}{T_r} = 0.9\,\mathrm{Hz}$, i.e. the spectral hole is related to the (constant) rise time and the coherent rupture propagation. Such spectral holes may affect the response of a structure to the ground motion if its eigenperiod is at the frequency of these holes. The *pseudo-dynamic* simulations, on the other hand, do not contain these large spectral holes, and hence the structural response to such ground motions is reliable over the entire frequency bandwith of the simulation.

Figure 6-6 and 6-7 display seismograms (velocity and acceleration) and amplitude spectra, respectively, for a scenario in which the entire Hayward- Rodgers Creek fault system ruptures in a single M = 7.44 earthquake. As before, the phase arrivals for the *pseudo-dynamic* and *kinematic* simulations are very similar, while the amplitudes are very different,

Source HR-21, M = 7.44 (fault-normal)
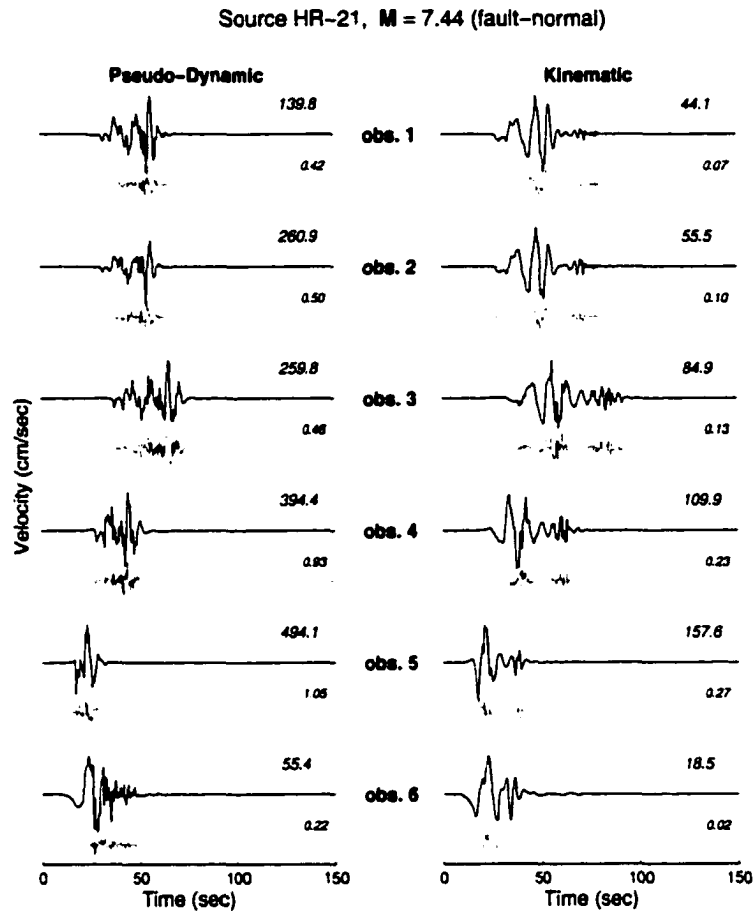
Figure 6-6: Synthetic seismograms at six observer locations for a simulated M = 7.44 earthquake, rupturing the entire Hayward-Rodgers Creek fault system. See Figure 6-4 for further explanation.

and the *kinematic* amplitude spectra again show the spectral holes. The interesting fact of this scenario is that even at relatively far distances (sites 1 and 2, located $\approx$ 30 km away from the rupture), large ground velocities (PGV = 140 cm/s; PGV = 260 cm/sec) and accelerations of up to 0.5 g are predicted by the *pseudo-dynamic* model. The very near-fault sites even experience peak ground accelerations of $\approx$ 1 g. While these PGA seem extremely large, they may not be unrealistic. *Heaton et al.*, [1995] list maximum observed PGA and PGV-values in earthquakes since 1971, and accelerations larger than 1 g are not uncommon. Though PGV-values of up to 180 cm/sec have been reported (Rinaldi-record of the 1994 Northridge earthquake [*Heaton et al*, 1995]), peak-velocities of more than 200 cm/sec seem unrealistically large. The *kinematic* simulations, on the other hand, have rather small

Source HR-21, M = 7.44 (fault-normal)
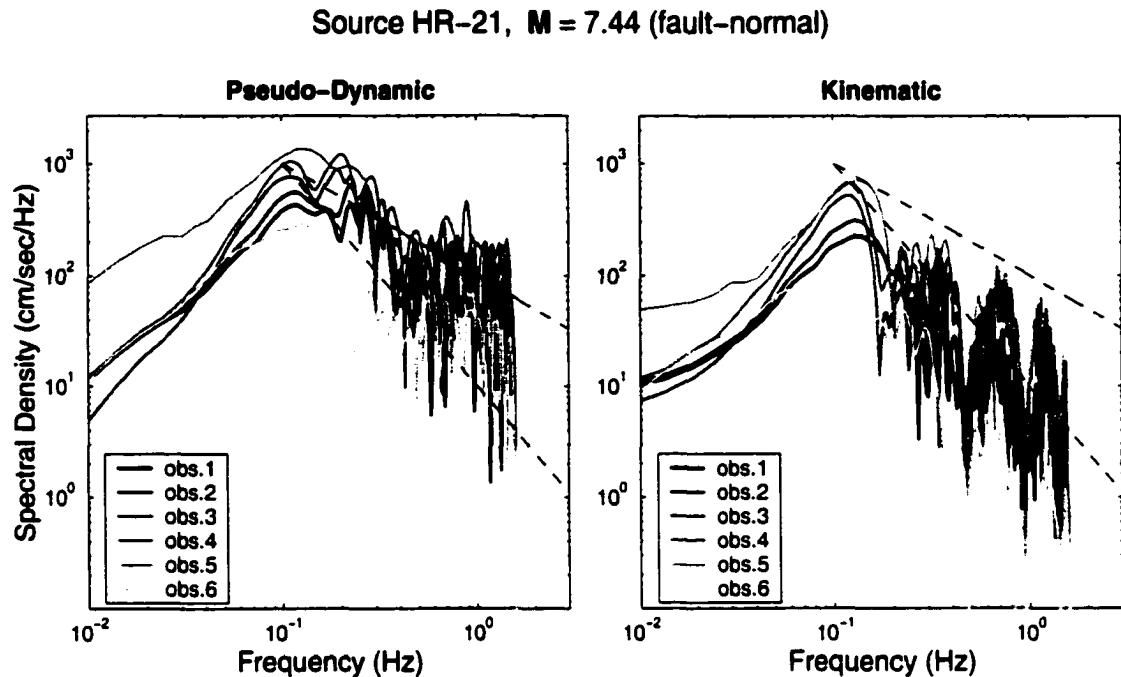
Figure 6-7: Fourier amplitude spectra for the velocity seismograms displayed in Figure 6-6. The broken lines indicate an ω^{-1}- and ω^{-2}-decay, respectively.

amplitudes (PGV and PGA) considering the magnitude of this scenario, indicating that the *kinematic* seismograms are not adequate.

Figure 6-8 displays velocity waveform (left) and acceleration time histories (right) for 30 rupture realization (median magnitude $M_w = 6.88$) on the South Hayward fault, calculated at observer 5 (closest distance, $R_{rup} = 7.1\,\text{km}$). PGV and PGA values are indicated above each record, the magnitude of each realization is printed between the seismogram sections. The location of site 5 with respect to scenario earthquakes on the South Hayward segment is such that directivity effects are minimized (i.e. backward directivity only) for ruptures that nucleate in the north and propagate southwards. Conversely, directivity should be very strong for northward propagating ruptures. The ground motions in Figure 6-8 in some sense reflect this expectation, showing PGV-values of 200 cm/sec and larger in case of forward-directivity. However, the velocity pulses are not as clean and distinct as one would expect, and occasionally the PGV-values are unrealistically large, indicating some deficiencies in the *pseudo-dynamic* source model. Seismograms in the backward directivity direction, on

Site 5 - Segment SH (pseudo-dynamic, fault-normal)
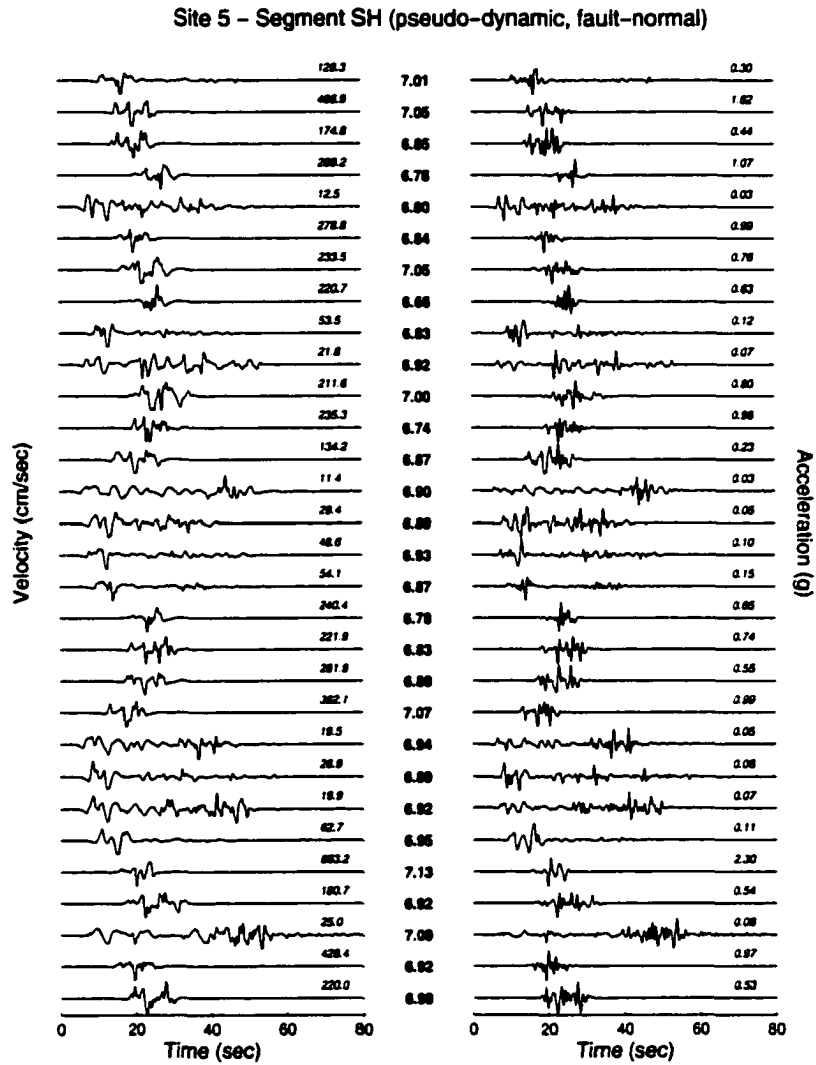
Figure 6-8: Velocity (left, in cm/sec) and acceleration (right, in g) synthetic seismograms at observer location 5 ($R_{rup} = 7.1$ km) for 30 scenario earthquakes (median magnitude $M_w = 6.88$) on the South Hayward segment. Small numbers (*italics*) denote *PGV* and *PGA*, respectively, larger numbers (**bold**) list the magnitude of each event.

the other hand, are characterized by long, low-amplitude wavetrains. Note that *PGA*-values frequently reach ≈ 1 g, and in two cases is even significantly larger ($PGA = 1.62$ g for realization 2, $PGA = 2.30$ g for realization 26).

Figure 6-9 shows the velocity and acceleration time series at observer 2 (closest distance, $R_{rup} = 27.7$ km) for 30 rupture realizations (median magnitude $M_w = 7.37$) on the entire

Site 2 - Segment HR (pseudo-dynamic, fault-normal)
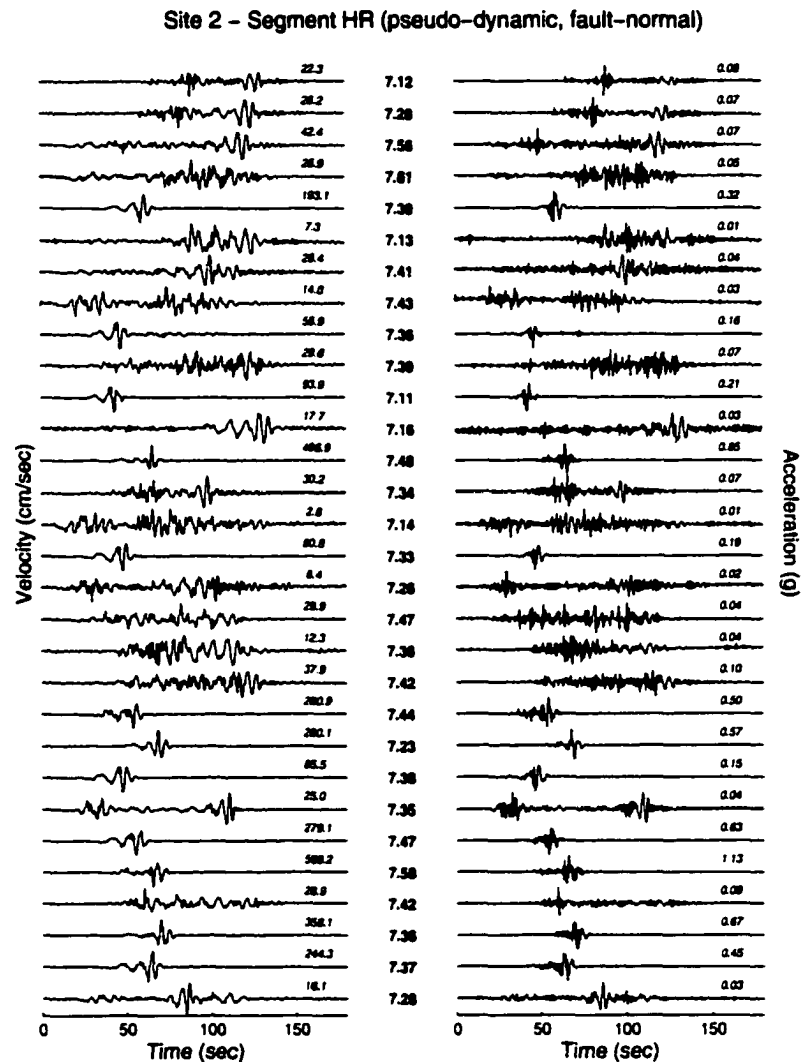
Figure 6-9: Same as Figure 6-8 for observer location 2 (R_{rup} = 27.7 km) for 30 scenario earthquakes (median magnitude M_w = 7.37) which rupture the entire length of the Hayward-Rodgers Creek fault system.

Hayward-Rodgers Creek fault system. The increased complexity of the waveforms is immediately evident, however, in many cases the ground motion levels (both, *PGA* and *PGV*) are considerably lower than for the South-Hayward-scenarios for observer 5 (Figure 6-8), although the magnitude of the South-Hayward-scenario earthquakes is significantly smaller. Obviously, directivity effects govern the distribution of ground motion intensity among the various scenario earthquakes and observer locations. For some of the scenarios shown in

Figure 6-9 we get extremely large peak-ground velocities, exceeding 300 cm/sec, which is clearly inappropriate. We attribute these very large *PGV*-values (and also *PGA*-vlaues) to the *pseudo-dynamic* source model which may generate rupture realizations that are physically unrealistic (see later discussion).

Summarizing the waveform and amplitude characteristics of the *kinematic* and *pseudo-dynamic* simulations, we find that the *pseudo-dynamic* source characterization provides more realistic *PGV*- and *PGA*-values than the *kinematic* model, occasionally generating extremely large values. The spectral characteristics of the *pseudo-dynamic* simulations appear to be more appropriate than *kinematic* simulations which display pronounced spectral holes and a spectral decay which may not be compatible with the observed ω^{-2}-decay of far-field pulse shapes.

6.4.4 Response-spectral characteristics

To conclude the comparison of *pseudo-dynamic* and *kinematic* ground motion simulations for scenario earthquakes on the Hayward-Rodgers Creek fault system, we analyse the response-spectral characteristics. Figure 6-10 and Figure 6-11 display average-horizontal (i.e. the geometric mean of the two horizontal components) response spectra for the *pseudo-dynamic* (left) and *kinematic* (right) simulations at sites 3 and 5, respectively, each with the median (thick line) and its standard deviation (thick broken line) for the individual response spectra (thin gray lines) for scenario earthquakes that rupture both the North and South Hayward fault. For comparison we also show the empirical ground motion predictions (thin black lines). These response spectral clearly demonstrate the difficiency of the *kinematic* simulations with respect to the empirical relationships, in particular for shorter periods ($T \leq 2\,\mathrm{Hz}$). The *pseudo-dynamic* simulations, on the other hand, generally agree with the empirical relations, but with a tendency to over-estimate spectral accelerations. Note that our simulations are valid only up the maximum frequency of $f_{max} = 1.8\,\mathrm{Hz}$, and response spectral values below periods $T = 0.625\,\mathrm{Hz}$ (indicated by the vertical line) are not accurate. It is important to note that the standard deviation of the *kinematic* response spectra roughly corresponds to the empirical standard deviation, while the variability of the *pseudo-dynamic* $S_A(T)$ is significantly larger. The large standard deviation in $S_A(T)$ of the *pseudo-dynamic* simulations can be attributed to the increased variability in the rupture process, allowing for variable rupture velocity, rise time and slip-velocity function. In particular, in some rupture realizations, the rupture propagates fast over areas of large slip, occasionally at

Observer 3 - Segment NS (R_{rup} = 16.7 km)
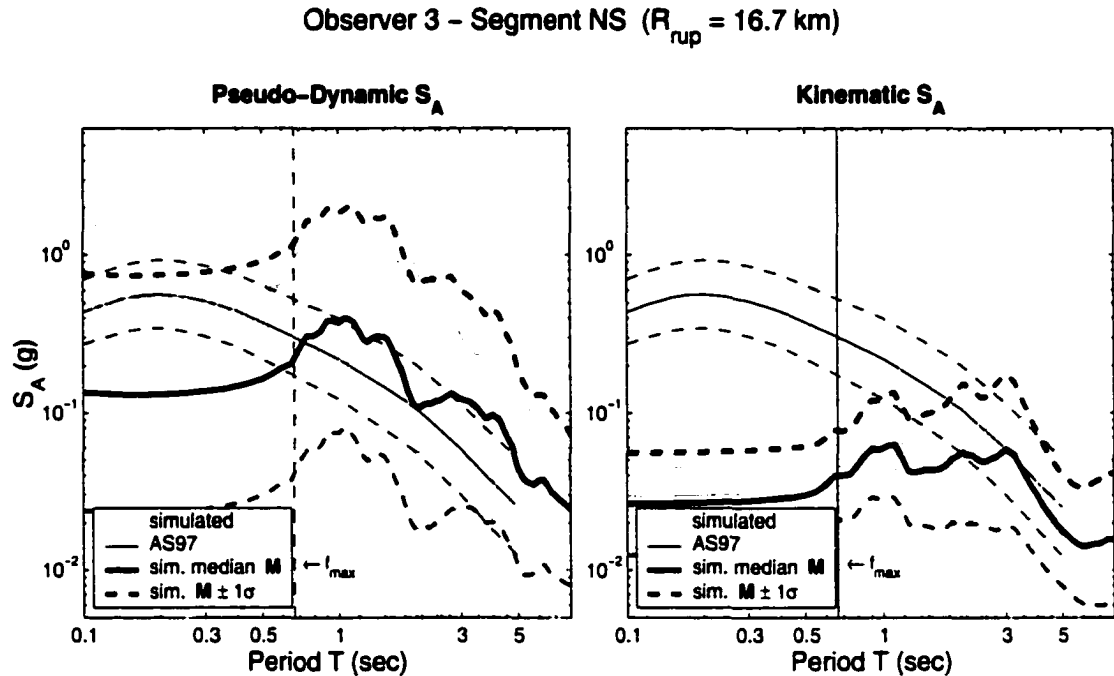
Figure 6-10: Spectral acceleration for *pseudo-dynamic* (left) and *kinematic* (right) simulations for 30 scenario earthquakes on the entire Hayward fault (median magnitude M_w = 7.08), calculated at observer 3 (R_{rup} = 16.7 km). Individual (thin gray lines) and median (thick black lines) average-horizontal response spectra are shown, as well as the empirical prediction for the median-magnitude event (thin black line) [*Abrahamson and Silva*, 1997]. The broken vertical lines indicates the shortest period included in our simulation (f = 1.8 Hz).

shallow depth, and hence generates unrealistically large peak ground motions.

6.5 Discussion

The ground motion simulations for scenario earthquakes on the Hayward-Rodgers Creek fault system clearly indicate that the simple *kinematic* source characterization results in ground motion intensities that are too small in amplitude (in the time domain as well as in the response-spectral domain). Moreover, the Fourier-spectral properties as well as the response spectra exhibit diffiencies with respect to observed ground motions and their spectral behavior. In contrast, the *pseudo-dynamic* simulations generally lead to adequate strong motion estimates, both in time and response-spectral domain, and the spectral behavior resembles closely what we know from observed ground motions. The big caveat

Observer 5 - Segment NS (R$_{rup}$ = 3.6 km)
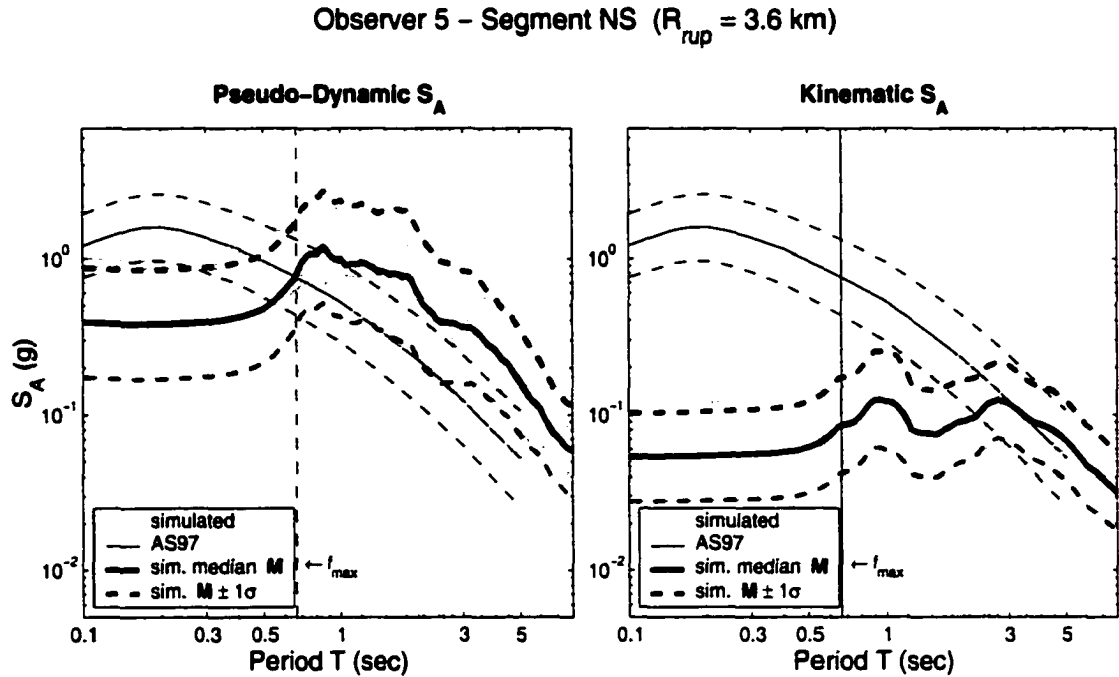
Figure 6-11: Same as Figure 6-10, but for observer 5 (R_{rup} = 3.6 km).

for the *pseudo-dynamic* simulations is that occasionally extremely large *PGV*-values (and hence *PGA*-values) are observed; we also note that the variability (standard deviation) of the ground motion intensities for the *pseudo-dynamic* simulation exceeds the empirically observed variability.

The increased standard variation in $S_A(T)$ as well as the large peak-ground velocities (and accelerations) are related to the current *pseudo-dynamic* source model, and we need to modify and optimize the *pseudo-dynamic* model to better reproduce the observed strong motion characteristics. Analyzing the source models for the 180 earthquake realizations, we find that the extreme values in *PGV* and *PGA* are generated by rupture models with large slip at shallow depth. Since we have not yet included a depth-dependence of stress drop in our model (i.e. low stress drop at shallow depth), such slip distributions are associated with large stress drop, and hence fast rupture velocity, occuring close to the surface. This kind of rupture behavior generates very large ground motions, however, it has not yet been observed, and perhaps is physically unrealistic. In some case, the rise times are also short in these regions of fast rupture propagation, aggravating the problem of large peak-ground

velocities even more. One possible solution to avoid large stress drop at shallow depth is to impose an additional depth-taper to the stress distribution on the fault plane. Initial tests were promising, but time-permitting we only could study a few cases. Future research will address this problem in more detail in order improve the *pseudo-dynamic* source model.

There are two more points worth mentioning pertaining to the *pseudo-dynamic* source characterization. In the simulations for the Hayward-Rodger Creek fault system, we have chosen to scale the *average* rise time over the rupture plane to be consistent with the median rise time estimate for that magnitude, following *Somerville et al.* [1999]. However, the *Somerville et al.* [1999] characterization of rise time is based on a different slip-velocity function (i.e. triangle), and hence their model predicts rise times that are too short when used in conjunction with a Kostrov-like quasi-dynamic slip velocity function. We will account for this problem in future research. Moreover, as already discusssed in Chapter 5, the current implementation of the quasi-dynamic slip-velocity function is apt to generate high-frequency seismic energy (and hence large peak-ground velocities), because of its sharp initial rise and the rather abrupt stopping. We applied a taper-function to the frequency-domain representation of the slip function to diminish the generation of these high-frequencies, but the effect was only minor, decreasing PGV-values by $\sim 10 - 15\%$ only. Perhaps a better approach to improve the slip-velocity function is to incorporate a more gradual initial onset, smooting the peak slip, and applying a more gradual taper function when rupture stops. *Nakamura and Miyatake* [2000] have proposed such an approximate expression for the slip-velocity function in the time domain. The challenge is to develop an accurate representation of this slip-velocity function in the frequency domain.

Another test to assess the performance of the *pseudo-dynamic* source model, besides comparing ground motion simulations with empirical predictions, would be to reproduce ground motion recordings from past earthquakes for which finite-source studies have been carried out. Possible candidate earthquakes for such an approach would be for instance the 1979 Imperial Valley, the 1984 Morgan Hill, the 1992 Landers, the 1995 Kobe or the 1999 Turkey events, for which high-quality near-source recordings as well as detailed source studies exist. Using the published slip distribution, we can apply the *pseudo-dynamic* source model, and then modify and improve it until the ground motion recordings are matched within some given prediction confidence level.

Despite the current shortcomings of the *pseudo-dynamic* source characterization, we believe that this model represents a significant advancement in characterizing the complexity

of the earthquake source for strong motion prediction. Eventually, our model may be capable to efficiently generate realistic, *dynamically-consistent* near-source strong ground motions. Time series of near-field strong ground motion are for instances needed in Performance-based engineering and Probabilistic Seismic Demand Analysis (PSDA) in which structures are modeled as dynamic, non-linear multi-degree-of-freedom systems. As noted earlier, data bases of strong motion recordings lack the very-near-source records for earthquakes of magnitude 7 and greater. Realistic ground motion simulations are therefore necessary to augment the sparse near-source recordings. The *pseudo-dynamic* source model provides a method to calculate such near-source strong motions for a wide range scenario earthquakes, which then can be used for engineering applications.

Luco et al. [2001b] have used the *kinematic* simulations for the scenario earthquakes on the Hayward-Rodgers Creek fault system for Probabilistic Seismic Demand Analysis (PSDA) at one of the near-fault sites (observer 5, Figure 6-1). Using their alternative ground motion intensity measure (IM) [*Luco*, 2001a], which incorporates an inelastic spectral displacement, they had to scale up the *kinematic* simulations by a factor two in order to drive the structure (9-story, steel moment-resisting frame building) into the non-linear range. The regressions of their IM's for simulated and observed ground motions also showed a smaller standard deviation of the (scaled up) simulations, indicating that at this point the *kinematic* simulations may not be appropriate for PSDA. In contrast, the preliminary results for the *pseudo-dynamic* simulation suggest that those may be more adequate for PSDA, but future research in this direction is needed.

6.6 Acknowledgements

Appendix A

M − log(A) Scaling Using an Expanded Dataset

The scaling relations developed in Chapter 2 are based on a subset only of the data presented in Table 2.1, because for some of the earthquakes slip models were either not available, or not reliable at that time. In this Appendix, I present updated scaling relations for the entire data set in Table 2.1, based on the *effective* source dimensions, followed by a short discussion on the implications of the modified scaling laws. The second part of this appendix focuses on the M−log(A)[1] scaling (not discussed in Chapter2), in particular on the implications for seismic hazard analysis.

The question of how seismic moment, M_w, scales with fault area, A, for large strike-slip earthquakes has recently received increased attention [*WorkingGroup99*, 2000; *Hanks and Bakun*, 2001]. This problem is important for two reasons: first, for our understanding of the rupture dynamics of strike-slip earthquakes, and second for seismic hazard studies. In particular, the relation between M_w and A might help resolve the hotly debated issue whether large strike-slip earthquakes are governed by "L-model" or "W-model" behavior. On the other hand, M−log(A) scaling relationships are widely used in seimic hazard analysis, and small variations in the particular relation between M and log(A) have a large impact on hazard calculations.

A.1 Modified Scaling Relations

Table A.1 lists the updated scaling coefficients using all slip models (Table 2.1), which can be compared to the initial coefficients in Table 2.3. Generally, the differences are moderate; most notably, the standard deviation σ_y decreases slightly, as well as the errors in slope and

---

[1]We use M and M_w interchangably; seismologists generally prefer M_w to indicate moment magnitude while the earthquake engineering community uses M to denote a more general earthquake magnitude. Only recently it was defined that $M = M_w$

Table A.1: Scaling coefficients between the source parameters as given by the *effective* source dimensions for **all** slip models listed in Table 2.1. In case of multiple slip models for a single earthquake, average source dimensions were used.

Equation	slope (error) b_1 (σ_{b_1})	intercept (error) b_0 (σ_{b_0})	standard deviation σ_y	correlation coefficient r^2
All Events				
$\log(L) = b_0 + b_1 M_o$	0.38 (0.03)	-5.98 (0.64)	0.15	0.86
$\log(W) = b_0 + b_1 M_o$	0.30 (0.04)	-4.63 (0.71)	0.17	0.75
$\log(A) = b_0 + b_1 M_o$	0.68 (0.05)	-10.61 (1.05)	0.25	0.88
$\log(D) = b_0 + b_1 M_o$	0.33 (0.05)	-4.21 (1.05)	0.25	0.62
$\log(D) = b_0 + b_1 \log(L)$	0.58 (0.18)	1.35 (0.25)	0.33	0.33
Strike-Slip Earthquakes				
$\log(L) = b_0 + b_1 M_o$	0.42 (0.05)	-6.69 (1.05)	0.13	0.89
$\log(W) = b_0 + b_1 M_o$	0.18 (0.05)	-2.40 (0.88)	0.10	0.68
$\log(A) = b_0 + b_1 M_o$	0.60 (0.08)	-9.09 (1.57)	0.19	0.88
$\log(D) = b_0 + b_1 M_o$	0.45 (0.07)	-6.48 (1.40)	0.17	0.84
$\log(D) = b_0 + b_1 \log(L)$	0.87 (0.25)	0.93 (0.35)	0.26	0.63
Dip-Slip Earthquakes				
$\log(L) = b_0 + b_1 M_o$	0.38 (0.04)	-6.01 (0.81)	0.16	0.86
$\log(W) = b_0 + b_1 M_o$	0.32 (0.04)	-5.02 (0.82)	0.16	0.82
$\log(A) = b_0 + b_1 M_o$	0.71 (0.07)	-11.03 (1.43)	0.28	0.87
$\log(D) = b_0 + b_1 M_o$	0.29 (0.07)	-3.51 (1.45)	0.28	0.54
$\log(D) = b_0 + b_1 \log(L)$	0.46 (0.24)	1.55 (0.34)	0.37	0.22

intercept, σ_{b_1} and σ_{b_0}, respectively. While the slope, b_1 has changed in most cases only by ±0.04, corresponding to an average change of 6 %, the intercept values are occasionally ±0.5 units higher or lower (an average change of 9.5 %). Estimating the source dimensions, given moment, with this set of scaling relations will therefore give different results than using the relations developed in Chapter 2. Because of the larger dataset, and hence smaller standard deviations, we recommend using the scaling coefficients in Table A.1 for that purpose.

It is interesting to note that the modified scaling coefficients for *all events* indicate self-similarity of the source dimensions, even more so than previously (Table 2.3), i.e. the slope for the length-scaling, width-scaling and slip-scaling are all close to $\frac{1}{3}$. Likewise for dip-slip earthquakes for which fault length, fault width and average displacement scale as $M_o \propto L^{1/3}$, $M_o \propto W^{1/3}$, $M_o \propto D^{1/3}$, respectively. In contrast, the length-coefficient and the slip-coefficient for strike-slip earthquakes have "pushed" their scaling behavior even farther from self-similarity. Interestingly, the modified area-scaling ($M_o \propto A^{0.6}$) is closer to self-similarity than before ($M_o \propto A^{0.57}$).

While we made no attempt in Chapter 2 to interpret the scaling between mean slip and fault length for strike-slip earthquakes (due to large error and small correlation coefficient), the updated relation between these two parameters is more meaningful. In fact, we find that $\log(D) \propto 0.87\,(\pm 0.25)\,\log(L)$, which is statistically indistinguishable from $\log(D) \propto \log(L)$, meaning that average displacement is proportional to fault length for strike-slip earthquakes. Such a relation may be indicative of "L-model" behavior in which mean slip continues to grow with increasing fault length, but does not saturate at a certain value related to the thickness of the seismogenic zone ("W-model"). This observation has been put forward by *Scholz* [1982], was rejected by *Romanowicz* [1992], but was again advocated recently by *Hanks and Bakun* [2001].

In a recent study, *Shaw and Scholz* [2001] address exactly this problem: how can we reconcile the observations of slip increasing proportionally with fault length in terms of the stress-drop invariance of small-earthquake scaling? Combining measurements and 3-D dynamic earthquake simulations, they find that for a constant stress drop assumption, slip increases with fault length up to a roll-over point at fault aspect ratios of $L/W \approx 10$. Beyond that, slip essentially saturates with fault width. The finite-source measurements presented here are based on a very limited data set, where the largest strike-slip earthquake (Izmit (Turkey), 1999) has moment magnitude $M_w = 7.4$, and an aspect ratio of about 6, and hence the roll-over to "W-model"-scaling may not have occured yet [*Bodin and Brune,* 1996; *Shaw and Scholz,* 2001]. *Shaw and Scholz* [2001] attribute these surprisingly large length-scales in the scaling of strike-slip earthquakes to dynamic effects in which propagating slip pulses, carrying potential and kinetic energy concentrations, take very long distances to evolve, but also to decay away. These long slip-transients also suggest that for very long ruptures the peak slip amplitude is reached far away from the epicenter.
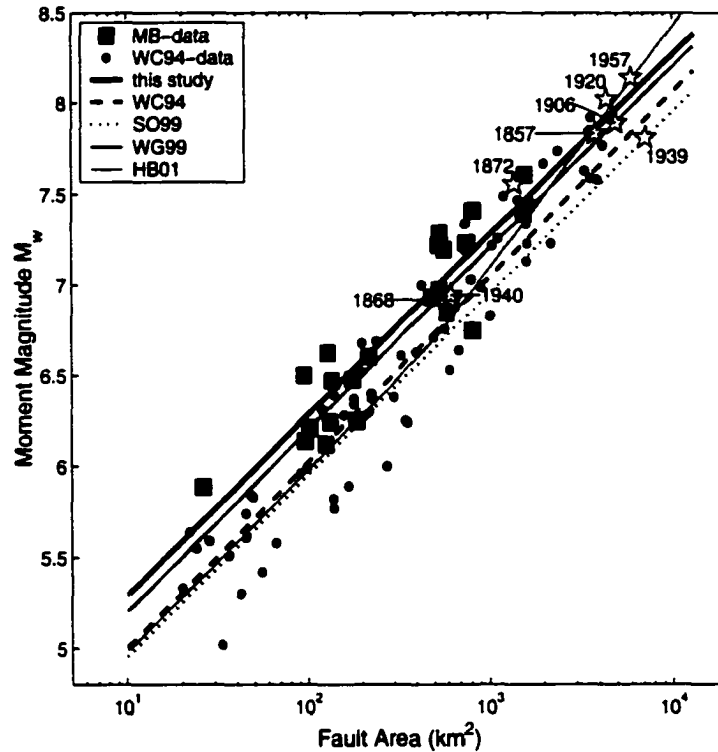
Figure A-1: Comparison of recent M_w − log(A)-scaling relations, and their consistency with the data presented in this study and the WC94 data [*Wells and Coppersmith, 1994*]. Stars indicate major historic strike-slip earthquakes that have not been used in developing these scaling laws. See text for details.

A.2 Implications for Seismic Hazard Analysis

Based on finite-source inversions for 22 strike-slip earthquakes (Table 2.1), we develop a relation between moment magnitude and fault area, and compare the resulting M−log(A)-scaling with recent models. Figure A-1 displays the finite-source data (large squares), the WC94-data (small circles) and eight historic strike-slip earthquakes (stars) that haven't been used in developing any of the proposed scaling models (various lines).

The most-widely used M − log(A)-relation for strike-slip earthquakes is given by *Wells and Coppersmith* [1994]

$$M = 3.98 + 1.02 \cdot \log(A), \tag{A.1}$$

shown with a thick broken line in Figure A-1 (denoted WC94). The fact that the slope is essentially indistinguishable from unity indicates self-similar scaling of fault area with

seismic moment. It has been argued, however, that this magnitude-area relationship performs poorly for very large strike-slip earthquakes, particularly in California [Dolan et al., 1995]. Alternatively, Somerville et al. [1999] found an unconstrained (i.e. slope not fixed) relationship of

$$M = 4.39 + 0.84 \cdot \log(A), \tag{A.2}$$

which they constrain to self-similar scaling as (dotted line in Figure A-1, denoted SO99)

$$M = 3.95 + \log(A). \tag{A.3}$$

The agreement between (A.1) and (A.3) is remarkable, but the problem for the largest strike-slip earthquakes remains in that these relationships both overpredict the fault area, and hence underpredict the slip. The WorkingGroup99 [2000] has put forward a model specifically for California (dark gray line in Figure A-1, denoted WG99),

$$M = 4.2 + \log(A), \tag{A.4}$$

whereas Hanks and Bakun [2001] advocate a bilinear model (light gray line in Figure A-1, denoted HB01),in which the scaling changes for large strike-slip earthquakes (M $\geq\sim$6.6, area $\geq\sim$500 km^2)

$$M = 3.98 + \log(A) \qquad A \leq 468km^2$$

$$\tag{A.5}$$

$$M = 3.07 + \tfrac{4}{3} \cdot \log(A) \quad A > 468km^2.$$

The thick black line in Figure A-1 depicts the scaling found for the finite-source strike-slip earthquakes (using averaged source parameters in case of multiple slip models),

$$M = 4.33 + 0.97 \cdot \log(A), \tag{A.6}$$

which agrees closely with the WorkingGroup99 [2000] model (A.4).

The additional data shown by stars in Figure A-1 are the M=7.8 1858 Ft. Tejon, M=6.9 1868 Hayward, M=7.6 1872 Lone Pine, M=7.9 1906 San Francisco, M=8.0 1920 Gansu (China), M=7.8 1939 Erzincan (Turkey), M=6.9 1940 Imperial Valley and M=8.1 1957 Gobi-Altay (Mongolia) earthquakes. For most of these earthquakes, the source dimensions

contain large uncertainties, and we have used averaged source dimensions if multiple estimates exists. Note that neither the *Wells and Coppersmith* [1994] nor the *Somerville et al.* [1999] relation passes through these data while the remaining models provide an adequate fit. It is apparent from these models that the WC94-relation (A.1) and the *Somerville et al.* [1999] relation (A.3) can be expected to systematically underestimate the magnitude of future M ≥ 7 strike-slip earthquakes.

The scaling relations given in (A.4) and (A.6) imply self-similar scaling, even out to the largest strike-slip earthquakes. This is counter-intuitive since it is expected that the width of the seismogenic zone affects the earthquake scaling in that self-similarity breaks down once the rupture length has grown to several fault widths. *Hanks and Bakun* [2001] incorporate this concept by assuming "L-model" behavior for large strike-slip earthquakes, finding the cut-off magnitude to be M ≈ 6.6. This "break" in the magnitude-area relation reflects the crossover from self-similar scaling for strike-slip earthquake to "L-model"-scaling, but doesn't consider the effect of slip saturation for very long ruptures ($L/W \geq 10$) [*Shaw and Scholz*, 2001]. For these large aspect-ratio earthquakes, "W-model"-scaling would predict a relation of the form M $\propto \frac{2}{3} \cdot \log(A)$. Neither the finite-source data, nor the *Wells and Coppersmith* [1994] or the historic events, however, require the proposed transitions, but rather suggest a simple linear relationship between magnitude and fault area. To settle the issue of "L-model" or "W-model" behavior and the "correct" magnitude-area relationship, we have to await more large strike-slip earthquakes (M ≥ 7.5). However, the use of the "correct" or at least an appropriate relationship between magnitude and fault area is critical in seismic hazard analysis.

Underestimating the magnitude of future earthquakes not only has an impact of the estimated ground motions, but also on the long-term recurrence rate of earthquakes. In seismic hazard analysis, the long-term slip rate on faults, accumulated through plate motion and released in earthquakes, is balanced with seismic moment; a low estimate of seismic moment results in more numerous, smaller- magnitude earthquakes. Correspondingly, this will lead to higher mean annual probabilities of occurence of large earthquakes, and hence the resulting seismic hazard analysis can be strongly biased. Without attempting to find the "best" or "correct" relationship between magnitude and area, given the limited data, the data and models presented in Figure A-1 strongly favor a model like (A.4) or (A.6) to be used in seismic hazard analysis, or perhaps (A.5) if further evidence for "L-model" behavior can be found for future strike-slip earthquakes.

Appendix B

Finite Strain Energy

The wavenumber spectrum for heterogeneous source models cannot be arbitrarily flat because the stresses associated with the resulting slip distribution will become infinite. *Andrews* [1981] points out that individual grains of rock may support shear stress of several kilobars, and that stress fluctuations of that order may occur on short scales as individual grains fracture or slide over each other. Yet, average stress drops of earthquakes are observed to be on the order of 100 bars or less. Hence, stress fluctuations at the kilometer scale are much smaller than 2 kbars. This conditions can be reconciled in terms of the static self-energy, E_s, that has to remain finite for any slip distribution characterized by the correlation functions given in Equation (3.1).

The change in static elastic energy during an earthquake is given as [*Aki and Richards*, 1980]

$$E = - \int \int [\tau^0(\xi) + \frac{1}{2}\tau(\xi)] \, D(\xi) \, d\xi \qquad (B.1)$$

where $\tau^0(\xi)$ is the initial shear stress on the fault plane (generally unknown), $\tau(\xi)$ and $D(\xi)$ are the stress change and slip during the earthquake, respectively; ξ denotes the position on the fault plane. The static self-energy is given by the second term in (B.1)

$$E_s = -\frac{1}{2} \int \int \tau(\xi) \, D(\xi) \, d\xi. \qquad (B.2)$$

which can be expressed in the Fourier domain as [*Andrews*, 1980a]

$$E_s(k) = -\frac{1}{2} \int \int \tau(k) \, D(k)^* \, dk_x \, dk_z \qquad (B.3)$$

where * denotes complex conjugate. In the wavenumber domain, slip $D(k)$ and stress $\tau(k)$

133

are related by a static stiffness function, $K(\mathbf{k})$, as [Andrews, 1980a]

$$\tau(\mathbf{k}) = -K(\mathbf{k}) D(\mathbf{k})$$ (B.4)

where

$$K(\mathbf{k}) = -\frac{\mu}{2k}\left[\frac{2(\lambda + \mu)}{\lambda + 2\mu}k_x^2 + k_z^2\right]$$ (B.5)

with $k = \sqrt{k_x^2 + k_z^2}$. For typical crustal rocks, $\lambda \approx \mu$, and (B.5) simplifies to $K(\mathbf{k}) = -\frac{\mu}{2k}\left[\frac{4}{3}k_x^2 + k_z^2\right] \approx -\frac{1}{2}\mu k$. Using (B.3) and (B.4) yields

$$E_s(\mathbf{k}) = \frac{1}{2}\int\int K(\mathbf{k}) D(\mathbf{k}) D(\mathbf{k})^* \, dk_x \, dk_z$$ (B.6)

which can be restated as

$$E_s(\mathbf{k}) = \frac{1}{2}\int\int K(\mathbf{k}) P_d(\mathbf{k}) \, dk_x \, dk_z,$$ (B.7)

with $P_d(\mathbf{k})$ being the two-dimensional power spectrum of the slip distribution $D(\boldsymbol{\xi})$.

The condition of finite static self-energy constrains the spectral decay of the slip spectrum at high wavenumber. To examine this condition for the spatial random field models in (3.1), we use the approximation that $K(\mathbf{k}) \approx -\frac{1}{2}\mu k$, and assume that $a_x^2 k_x^2 + a_z^2 k_z^2 \gg 1$, reflecting the fact that the stresses are likely to become infinite only at small scales. Without loss of generality, we assume isotropy $(a_x \approx a_z = a)$. The following discussion can be further simplified by using polar coordinates in k-space, for which Equation (B.7) becomes

$$E_s(k_r) = \frac{1}{2}\int K(k_r) P_d(k_r) 2\pi \, k_r \, dk_r,$$ (B.8)

Static strain energy will remain finite if the integral in (B.8) converges for all k_r.

Gaussian auto-correlation function

The power spectral density for the Gaussian model is given in (3.1); using polar coordinates and assuming isotropy, this becomes

$$P_d(k_r) = \frac{a^2}{2}e^{-\frac{1}{4}a^2 k_r^2}.$$ (B.9)

Inserting this expression into (B.8) yields

$$E_s(k_r) \approx -\frac{\pi\mu a^2}{4} \int k_r^2 e^{-\frac{1}{4}a^2 k_r^2} dk_r$$

$$\approx -\frac{\pi\mu}{2} \left[k_r e^{-\frac{1}{4}a^2 k_r^2} + \frac{c}{a} Erfc(\frac{1}{2}ak_r) \right]$$

(B.10)

with $c \approx 3.54$. This expression converges for all k_r, and the condition of finite static strain energy is satisfied.

Von Karman auto-correlation function

Assuming isotropy and using polar coordinates, the power spectral density for the von Karman correlation function in Equation (3.1) becomes

$$P_d(k_r) = \frac{a^2}{(1 + a^2 k_r^2)^{H+1}}.$$

(B.11)

Inserting this expression into (B.8) we find that

$$E_s(k_r) \approx -c_H \int \frac{1}{k_r^{2H}} dk_r.$$

(B.12)

where $c_H = \frac{2\pi^2 \mu H}{K_H(0)} \frac{1}{a^{2H}}$. This integral expression for the static strain energy depends on the Hurst exponent, H, and three cases are of particular interest: (1) $H > 0.5$; (2) $H = 0.5$; (3) $H < 0.5$. In the first case $(H > \frac{1}{2})$, the integral converges for all k_r, and strain energy remains finite. The second case $(H = \frac{1}{2})$ corresponds to the exponential ACF, and the static strain energy can be re-written as

$$E_s(k_r) \approx -\frac{\pi\mu}{2a} \int \frac{1}{k_r} dk_r.$$

(B.13)

This integral diverges as the logarithm of the wavenumber at the upper limit of k_r. For case (3) with $H < \frac{1}{2}$, the integral in (B.12) diverges as a power law. There is infinite strain energy in the short wavelength for $H \leq \frac{1}{2}$, and hence Hurst exponents $H \leq 0.5$ are not admissable to simulate heterogeneous slip distributions.

Fractal model

We rewrite the power spectral density $P_d(k)$ for the fractal model in Equation (3.1) using polar coordinates as

$$P_d(k_r) \propto \frac{1}{(k_r^2)^{4-D}}.$$
(B.14)

Using (B.8), the static self-energy is given as

$$E_s(k_r) \propto \frac{\pi\mu}{2} \int \frac{1}{(k_r)^{6-2D}} \, dk_r.$$
(B.15)

This integral expression is unbounded for slip distributions with fractal dimension $D \geq 2.5$; for $D = 2.5$, the integral diverges as the logarithm of the wavenumber at the upper limit of k_r, for $D > 2.5$, it diverges as a power law. Fractal dimensions of $D < 2.5$ (as found in the analysis of finite-source models) or $D = 2$ (as in the "k-square" model [*Herrero and Bernard*, 1994]) are admissable to simulate slip distributions.

Appendix C

Bibliography

Aargard, B.T., J.F. Hall, and T.H. Heaton (2001). Characterization of near-source ground motions with earthquake simulations, *Earthquake Spectra*, **17**, 177-207.

Abrahamson, N. A., and W. J. Silva (1997). Empirical response spectral attenuation relations for shallow crustal earthquakes, *Seism. Res. Lett.*, **68**, 94-128.

Akaike H. (1980). Likelihood and the Bayes procedure, in *Bayesian Statistics*, J.M. Bernardo, M.H. DeGroot, D.V. Lindley, and A.F.M. Smith (Editors), University Press, Valencia (Spain), 143-166.

Aki, K. (1972). Earthquake mechanism, *Tectonophysics*, **13**, 423-446.

Aki, K. (1979). Characterization of barriers on an earthquake fault, *J. Geophys. Res.*, **73**, 5,359-5,376.

Aki, K., and P.G. Richards (1980). *Quantitative Seismology, Theory and Methods*, W.H. Freeman and Company, New York.

Andrews, D.J. (1976a). Rupture propagation with finite stress in antiplane strain *J. Geophys. Res.*, **81**, 3,575-3,582.

Andrews, D.J. (1976b). Rupture velocity of plain strain shear cracks *J. Geophys. Res.*, **81**, 5,679-5,687.

Andrews, D.J. (1980a). Fault impedance and earthquake energy in the Fourier transform domain, *Bull. Seismol. Soc. Am.*, **70**, 1,683-1,698.

Andrews, D.J. (1980b). A stochastic fault model, I. Static case, *J. Geophys. Res.*, **85**, 3,867-3,877.

Andrews, D.J. (1981). A stochastic fault model, II. Time-dependent case, *J. Geophys. Res.*, **86**, 10,821-10,834.

Andrews, D.J. (1985). Dynamic plane-strain shear rupture with a slip-weakening friction law calculated by a boundary integral method, *Bull. Seismol. Soc. Am.*, **75**, 1-21.

137

Anguiano, E., M. Pancorbo, and M. Aguilar (1994). Pitfalls in the fractal characterization of real microscopic surfaces by frequency analysis and proposal of a new method, *Fractals in the Natural and Applied Sciences*, M.M. Novak (Editor), Elseviewer Science, 37-46.

Archuleta, R.J., and S. Hartzell (1981). Effect of fault finiteness on near-source ground motion, *Bull. Seismol. Soc. Am.*, **71**, 939-957.

Archuleta, R.J. (1984). A faulting model for the 1979 Imperial Valley earthquake, *J. Geophys. Res.*, **89**, 4,559-4,585.

Aviles, C.A., C.H. Scholz, and J. Boatwright (1987). Fractal analysis applied to characteristic segments of the San Andreas Fault, *J. Geophys. Res.*, **82**, 331-344.

Bennett, R.A., R.E. Reilinger, W.L. Rodi, Y. Li, M.N. Toksoz, and K.W. Hudnut (1995). Coseismic fault slip associated with the 1992 $M_w = 6.1$ Joshua Tree, California, earthquake; implications for the Joshua Tree-Landers earthquake sequence, *J. Geophys. Res.*, **100**, 6,443-6,461.

Beresenv, I., and G. Atkinson (2001). Subevent structure of large earthquakes - A ground motion perspective, *Geophys. Res. Lett.*, **28**, 53-56.

Berge, C, J.-C. Gariel, and P. Bernard (1998). A very broad-band stochastic source model used for near source strong motion prediction, *Geophys. Res. Lett.*, **25**, 1,063-1,066.

Bernard, P., A. Herrero, and C. Berge (1996). Modeling directivity of heterogeneous earthquake ruptures, *Bull. Seismol. Soc. Am.*, **86**, 1,149-1,160.

Beroza, G.C. (1991). Near-source modeling of the Loma Prieta earthquake; evidence for heterogeneous slip and implications for earthquake hazard, *Bull. Seismol. Soc. Am.*, **81**, 1,603-1,621.

Beroza, G.C., and P. Spudich (1988). Linearized inversion for fault rupture behavior; application to the 1984 Morgan Hill, California, earthquake, *J. Geophys. Res.*, **93**, 6,275-6,296.

Beroza, G.C., and W.L. Ellsworth (1996). Properties of the seismic nucleation phase, *Tectonophysics* **261**, 209-227.

Beroza, G.C., and T. Mikumo (1996). Short slip duration in dynamic rupture in the presence of heterogeneous fault properties, *J. Geophys. Res.*, **101**, 22,449-22,460.

Boatwright, J., and H. Quin (1986). The seismic radiation from a 3-D dynamic model of a complex rupture process, Part 1. Confined rupture, *Earthquake Source Mechanics*, S. Das (Editor), *Geophysical Monograph, Am. Geophys. Union* **37**, 97-109, 1986.

Bodin, P., and J.N. Brune (1996). On the scaling of slip with rupture length for shallow

strike-slip earthquakes; quasi-static models and dynamic rupture propagation, *Bull. Seismol. Soc. Am.*, **86**, 1,292-1,299.

Boore, D. M., and W. B. Joyner (1981). Peak horizontal acceleration and velocity from strong-motion records including records from the 1979 Imperial Valley, California, earthquake, *Bull. Seismol. Soc. Am.*, **71**, 2,011-2,038.

Boore, D. M., and W. B. Joyner (1982). The empirical prediction of ground motion, *Bull. Seismol. Soc. Am.*, **72**, S269-S286.

Boore, D. M., and W. B. Joyner (1989). The effect of directivity on the stress parameter determined from ground motion observations, *Bull. Seismol. Soc. Am.*, **79**, 1,984-1,988.

Boore, D. M., and W. B. Joyner (1997). Site amplifications for generic rock sites. *Bull. Seismol. Soc. Am.*, **87**, 327-341.

Boore, D.M., W.B. Joyner, and T.E. Fumal (1997). Equations for estimating horizontal response spectra and peak acceleration from western North American earthquakes; a summary of recent work, *Seis. Res. Lett.*, **68**, 128-153.

Bouchon, M., M. Campillo, and F. Cotton (1996). Stress field associated with the rupture of the 1992 Landers, California, earthquake and its implications concerning the fault strength at the onset of the earthquake, *J. Geophys. Res.*, **103**, 21,091-21,097.

Bouchon, M. (1997). The state of stress on some faults of the San Andreas system as inferred from near-field strong motion data, *J. Geophys. Res.*, **102**, 11,731-11,744.

Bouchon, M., N.M. Toksoz, H. Karabulut, M.-P. Bouin, M. Dietrich, M. Aktar, and M. Edie (2000). Seismic imaging of the 1999 Izmit (Turkey) rupture inferred from near-fault recordings, *Geophys. Res. Lett.*, **27**, 3,013-3,016.

Bracewell, R.N. (1986). The Fourier Transform and its Applications, *McGraw-Hill*, New York.

Brune, J.N., J.B. Fletcher, F.L. Vernon, L.C. Haar, T.C. Hanks, J. Berger, J. Boatwright, and C.H. Scholz (1986). Low stress-drop earthquakes in the light of new data from the Anza, California telemetered digital array, *Earthquake Source Mechanics*, S. Das (Editor), *Geophysical Monograph, Am. Geophys. Union* **37**, 237-245.

Choy, G.L., and J. Boatwright (1981). The rupture characteristics of two deep earthquakes inferred from broadband GDSN data, *Bull. Seismol. Soc. Am.*, **71**, 691-711.

Choy, G.L., and J. Boatwright (1995). Global patterns of radiated seismic energy and apparent stress, *J. Geophys. Res.*, **100**, 18,205-18,226.

Cohee, B.P., and G.C. Beroza (1994). Slip distribution of the 1992 Landers earthquake and its implications for earthquake source mechanics, *Bull. Seismol. Soc. Am.*, **84**, 693-712.

Cornell, C.A (1968). Engineering seismic risk analysis, *Bull. Seismol. Soc. Am.*, **58**, 1,583-1,606.

Cotton, F., and M. Campillo (1995). Frequency domain inversion of strong motions; application to the 1992 Landers earthquake, *J. Geophys. Res.*, **100**, 3,961-3,975.

Darragh, R.B., and B.A. Bolt (1987). A comment on the statistical regression relation between earthquake magnitude and fault rupture length, *Bull. Seismol. Soc. Am.*, **77**, 1,479-1,484.

Das S., and K. Aki (1977). Fault planes with barriers: a versatile earthquake model, *J. Geophys. Res.*, , **82**, 5,648-5,670.

Das S., and B.V. Kostrov (1987). On the numerical boundary integral equation method for three-dimensional dynamic shear crack problems, *Jour. Appl. Mech.*, **54**, 99-104.

Day, S.M. (1982). Three-dimensional simulation of spontaneous rupture: the effect of nonuniform prestress, *Bull. Seismol. Soc. Am.*, **72**, 1,881-1,902.

Day, S.M., G. Yu, and D. Wald (1998). Dynamic stress changes during earthquake rupture, *Bull. Seismol. Soc. Am.*, **88**, 512-522.

Dreger, D.S. (1994). Empirical Green's function study of the January 17, 1994 Northridge, California earthquake, *Geophys. Res. Lett.*, **21**, 2,633-2,636.

Dolan, J. F., K. Sieh, T. Rockwell, R. S. Yeats, J. Shaw, J. Suppe, G.J. Huftile, and E. Gath (1995). Prospects for larger or more frequent earthquakes in the Los Angeles metropolitan region, *Science*, **267**, 199-205.

Ellsworth, W.L., and G.C. Beroza (1995). Seismic evidence for a seismic nucleation phase, *Science*, **268**, 851-855.

Frankel, A. (1991). High-frequency spectral fall-off of earthquakes, fractal dimension of complex rupture, *b* value, and the scaling of strength on faults, *J. Geophys. Res.*, **96**, 6,291-6,302.

Freund, L. (1979). The mechanics of dynamic shear crack propagation, *J. Geophys. Res.*, **84**, 2,199-2,209.

Fujii, Y., and M. Matsu'ura (1999). Regional differences in scaling laws for large earthquakes and its tectonic implications *EOS, Transaction, Am. Geophys. Union*, **80**, 934.

Goff, J.A., and T.H. Jordan (1988). Stochastic Modeling of seafloor morphology: inversion of sea beam data for second-order statistics, *J. Geophys. Res.*, **93**, 13,589-13,608.

Graves, R.W. (1998). Three-dimensional finite-difference modeling of the San Andreas fault: Source parameterization and ground-motion levels, *Bull. Seismol. Soc. Am.*, **88**, 881-897.

Guatteri, M., and P. Spudich (1998). Coseismic changes of slip direction: The effect of absolute stress on dynamic rupture, *Bull. Seismol. Soc. Am.*, **88**, 777-789.

Guatteri, M., and P. Spudich (2000a). What can strong motion data tell us about slip-weakening fault-friction laws? *Bull. Seismol. Soc. Am.*, **90**, 98-116.

Guatteri, M. (2000b). Inferring fault rupture dynamics from strong motion data *Ph.D. Thesis*, Stanford University.

Guatteri, M., P.M. Mai, G.C. Beroza, and J. Boatwright (2000). Strong ground motion simulation with stochastic- dynamic rupture models, *EOS, Transaction, Am. Geophys. Union*, **81**, 866.

Guatteri, M., P. Spudich, and G.C. Beroza (2001). Inferring rate and state friction parameters from a rupture model of the 1995 Hyogo-ken Nanbu (Kobe) earthquake, *J. Geophys. Res.*, in press.

Guatteri, M., P.M. Mai, G.C. Beroza, and J. Boatwright (2000). Strong ground motion prediction from stochastic-dynamic source models, *Bull. Seismol. Soc. Am.*, in review.

Hall, J.F., and T.H. Heaton (1995). Near-source ground motion and its effects on flexible buildings, *Earthquake Spectra*, **11**, 569-605.

Hanks, T.C., and H. Kanamori (1979). A moment magnitude scale, *J. Geophys. Res.*, **84**, 2,348-2,350.

Hanks, T.C., and W.H. Bakun (2001) Source-scaling models for A $M - \log(A)$ observations of continental earthquakes, *Bull. Seismol. Soc. Am.*, in review.

Hartzell, S. (1980). Faulting process of the May 17, 1976 Gazli, USSR, earthquake, *Bull. Seismol. Soc. Am.*, **70**, 1,715-1,736.

Hartzell, S.H. (1989). Comparison of seismic waveform inversion results for the rupture history of a finite fault; application to the 1986 North Palm Springs, California, earthquake, *J. Geophys. Res.*, **94**, 7,515-7,534.

Hartzell, S.H., and T.H. Heaton (1983). Inversion of strong ground motion and teleseismic waveform data for the fault rupture history of the 1979 Imperial Valley, California, earthquake, *Bull. Seismol. Soc. Am.*, **73**, 1,553-1,583.

Hartzell, S.H and T.H. Heaton (1986). Rupture history of the 1984 Morgan Hill, California, earthquake from the inversion of strong motion records, *Bull. Seismol. Soc. Am.*, **76**, 649-674.

Hartzell, S.H., and M. Iida (1990). Source complexity of the 1987 Whittier Narrows, California, earthquake from the inversion of strong motion records, *J. Geophys. Res.*, **95**, 12,475-12,485.

Hartzell, S.H., and C. Mendoza (1991). Application of an iterative least-squares waveform inversion of strong motion and teleseismic records to the 1978 Tabas, Iran, earthquake, *Bull. Seismol. Soc. Am.*, **81**, 305-331.

Heaton, T.H. (1982). The 1971 San Fernando earthquake; a double event?, *Bull. Seismol. Soc. Am.*, **72**, 2,037-2,062.

Heaton, T.H. (1990). Evidence for and implications of self-healing pulses of slip in earthquake rupture, *Phys. Earth Planet. Interiors*, **64**, 1-20.

Heaton, T.H., J.F. Hall, D.J Wald, and M.W. Halling (1995). Response of high-rise and base-isolated buildings to a hypothetical $M_w = 7$ blind thrust earthquake, *Science*, **267**, 206-211.

Harvey D., and G.L. Choy (1982). Broad-band deconvolution of GDSN data, *Geophys. J. R. Astr. Soc.*, **69**, 659-668.

Herrero, A., and P. Bernard (1994). A kinematic self-similar rupture process for earthquakes, *Bull. Seismol. Soc. Am.*, **84**, 1,216-1,228.

Hisada, Y. (2000). A theoretical omega-square model considering the spatial variation in slip and rupture velocity, *Bull. Seismol. Soc. Am.*, **90**, 387-400.

Hisada, Y. (2001). A theoretical omega-square model considering the spatial variation in slip and rupture velocity, Part 2: Case for a two-dimensional source model *Bull. Seismol. Soc. Am.*, **91**, 651-666.

Holliger, K., and A.R. Levander (1992). A stochastiv view of lower crustal fabric based on evidence from the Ivrea zone, *Geophys. Res. Lett.*, **11** 1,153-1,156.

Hough, S.E., and D.S. Dreger (1995). Source parameters of the 23 April 1992 M 6.1 Joshua Tree, California, earthquake and its aftershocks; empirical Green's function analysis of GEOS and TERRAscope data, *Bull. Seismol. Soc. Am.*, **85**, 1,576-1,590.

Hough, S.E., and Scientists from the U.S. Geological Survey, Southern California Earthquake Center, and California Division of Mines and Geology, Preliminary report on the 16 October 1999 M 7.1 Hector Mine, California, earthquake, *Seis. Res. Lett.*, **71**, 11-23, 2000.

Hudnut, K.W., Z. Shen, M. Murray, S. McClusky, R. King, T. Herring, B. Hager, Y. Feng, P. Fang, A. Donnellan, and Y. Block (1996). Co-seismic displacements of the 1994 Northridge, California, earthquake, *Bull. Seismol. Soc. Am.*, **86**, 19-36.

Ichinose, G.A., P. Goldstein, and A.J. Rodgers (2000). Relative importance of near-, intermediate and far-field displacement terms in layered Earth synthetic seismograms. *Bull. Seismol. Soc. Am.*, **90**, 531-536.

Inoue, T., and T. Miyatake (1998). 3-D simulation of near-field strong ground motion based on dynamic modeling, *Bull. Seismol. Soc. Am.*, **88**, 1,445-1,456.

Irikura, K., and K. Kamae (1994). Estimation of strong ground motion in broad-frequency band based on a seismic source scaling model and an empirical Green's function technique, *Annali di Geophysica*, **37**, 1,721-1,743.

Kamae, K., and K. Irikura (1998). Source model of the 1995 Hyogo-ken Nanbu earthquake and simulation of near-source ground motion, *Bull. Seismol. Soc. Am.*, **88**, 400-412.

Kanamori, H., and D.L. Anderson (1975). Theoretical basis of some empirical relations in seismology, *Bull. Seismol. Soc. Am.*, **65**, 1,073-1,095.

Kanamori, H., and C. R. Allen (1986). Earthquake repeat times and average stress drop, *Earthquake Source Mechanics*, S. Das (Editor), *Geophysical Monograph, Am. Geophys. Union* **37**, 227-236, 1986.

Larsen, S., R. Reilinger, H. Neugebauer, and W. Strange (1992). Global Positioning System measurements of deformations associated with the 1987 Superstition Hills earthquake; evidence for conjugate faulting, *J. Geophys. Res.*, **97**, 4,885-4,902.

Liu, H., and D.V. Helmberger (1983). The near-source ground motion of the 6 August 1979 Coyote Lake, California, earthquake, *Bull. Seismol. Soc. Am.*, **73**, 201-218.

Luco, N. (2001a). Probabilistic seismic demand analysis, SMRF connection fractures, and near-source effects *Ph.D. Thesis*, Dept. of Civil and Environmental Engineering, Stanford University, California.

Luco, N., P.M. Mai, C.A. Cornell, and G.C. Beroza (2001b). Probabilistic seismic demand analysis at a near-fault site using ground motion simulations based on a stochastic-kinematic earthquake source model, 7th *U.S. National Conference on Earthquake Engineering*, Boston (July 2002), in review.

Madariaga, R. (1976). Dynamics of an expanding circular fault, *Bull. Seismol. Soc. Am.*, **66**, 639-666.

Madariaga, R. (1983). High frequency radiation from dynamic earthquake fault models, *Annales Geophysicae*, 1, 17-23.

Mai, P.M., G.C. Beroza, and P. Segall (1998). Generalized description of finite-source rupture models, *EOS, Transaction, Am. Geophys. Union*, **79**, 632.

Mai, P.M., and G.C. Beroza (1999). Characterization of complex earthquake slip as as spatial random field, *EOS, Transaction, Am. Geophys. Union*, **80**, 707.

Mai, P.M., and G.C. Beroza (2000). Source scaling properties from finite-fault rupture models, *Bull. Seismol. Soc. Am.*, **90**, 605-614.

Mai, P.M., M. Guatteri, G.C. Beroza, and J. Boatwright (2001). Toward a more physical basis for strong-motion simulation, *Seism. Res. Lett.*, **72**, 273.

Mai, P.M., and G.C Beroza (2001a). A spatial random-field model to characterize complexity in earthquake slip, *J. Geophys. Res.*, in review.

Mai, P.M., and G.C. Beroza (2001b). A hybrid method for calculating near-source, broadband seismograms: Application to strong motion prediction, *Phys. Earth Planet Inter.*, in review.

Mai, P.M, M. Guatteri, and G.C. Beroza (2001c) A stochastic-dynamic earthquake source model for strong motion prediction, 7th *U.S. National Conference on Earthquake Engineering*, Boston (July 2002), in review.

Matsu'ura, M., and T. Sato (1997). Loading mechanism and scaling relations of large intraplate earthquakes, *Tectonophysics*, **277**, 189-198.

McGuire, J., L. Zhao, and T. Jordan (2001). Predominance of unilateral rupture for a global catalog of large earthquakes, *Bull. Seismol. Soc. Am.*, in review.

Mendoza, C., and S.H. Hartzell (1988). Inversion for slip distribution using teleseismic P waveforms; North Palm Springs, Borah Peak, and Michoacan earthquakes, *Bull. Seismol. Soc. Am.*, **78**, 1,092-1,111.

Mikumo, T., and T. Miyatake (1993). Dynamic rupture process on a dipping fault, and estimates of stress drop and strength excess from the results of waveform inversion, *Geophys. J. Int.*, **112**, 481-496.

Mikumo, T., and T. Miyatake (1995). Heterogeneous distribution of dynamic stress drop and relative fault strength recovered from the results of waveform inversion; the 1984 Morgan Hill, California earthquake, *Bull. Seismol. Soc. Am.*, **85**, 178-193.

Nakamura, H., and T. Miyatake (2000). An approximate expression of slip velocity time functions for simulation of near-field strong ground motion, *Zishin (Journal of the Seismological Society of Japan)*, **53**, 1-9, (in Japanese).

O'Connell, D.R., and J.P. Ake (1995). Ground motion analysis for Hoover Dam, *Seismotectonic Report*, **94-1**, Bureau of Reclamation, Denver, Colorado.

Oglesby, D.D., R. Archuleta, and S.B.Nielsen (1998). Earthquakes on dipping faults: The effect of broken symmetry, *Science*, **280**, 1,055-1,059.

Oglesby, D.D., R. Archuleta, and S.B.Nielsen (2000a). The three-dimensional dynamics of dipping faults, *Bull. Seismol. Soc. Am.*, **90**, 616-628.

Oglesby, D.D., R. Archuleta, and S.B.Nielsen (2000b). Dynamics of dip-slip faulting; explorations in two dimensions *J. Geophys. Res.*, **105**, 13,643-13,653.

Okubo, P.G, and K. Aki, Fractal geometry in the San Andreas Fault system, *J. Geophys. Res.*, *92*, 345-355, 1987.

Olsen, K.B., R.J. Archuleta, and J.R. Matarese (1995). Magnitude 7.75 earthquake on the San Andreas Fault: three-dimensional ground motion in the Los Angeles, *Science*, **270**, 1,628-1,632.

Olsen, K.B., and R.J. Archuleta (1996). Three-dimensional simulation of earthquakes on the Los Angeles fault systems, *Bull. Seismol. Soc. Am.*, **86**, 575-596.

Olsen, K.B., R. Madariaga, and R.J. Archuleta (1997). Three-dimensional dynamic simulation of the 1992 Landers earthquake, *Science*, **278**, 834-838.

Olson A.H., J.A. Orcutt, and G.A. Frazier (1984). The discrete wavenumber/finite element method for synthetic seismograms, *Geophys. J. R. Astr. Soc.*, **77**, 421-460.

Pacheco, J.F., C.H. Scholz, and L.R. Sykes (1992). Changes in frequency-size relationship from small to large earthquakes, *Nature*, **355**, 71-73.

Papageorgiou, A.S., and K. Aki (1983). A specific barrier model for the quantitative description of inhomogeneous faulting and the prediction of strong ground motion, I, Description of the model, *Bull. Seismol. Soc. Am.*, **73**, 693-722.

Pardo-Igúzquiza, E. and M. Chica-Olmo (1993). The Fourier integral method: an efficient spectral method for simulation of random fields, *Mathem. Geology*, **25**, 177-217.

Pérez-Campos, X., and G.C. Beroza (2001). Mechanism dependent scaling of radiated seismic energy, *J. Geophys. Res.*, **106**, 11,127-11,136.

Pitarka, A., K. Irikura, T. Iwata, and H. Sekiguchi (1998). Three-dimensional simulation of near-fault strong ground motion for the 1996 Hyogo-ken Nanbu (Kobe), Japan, earthquake, *Bull. Seismol. Soc. Am.*, **88**, 428-440.

Pitarka, A., P.G. Somerville, Y. Fukushima, T. Uetake, and K. Irikura (2000). Simulation of near-fault strong ground motion using hybrid Green's functions, *Bull. Seismol. Soc. Am.*, **90**, 556-586.

Quin, H. (1990). Dynamic stress drop and rupture dynamics of the October 15, 1979 Imperial Valley, California, earthquake, *Tectonophysics*, **175**, 93-117.

Quin, H., and S. Das (1989). A hybrid boundary integral equation method for the computation of source time functions for 3D rupture propagation, *Geophys. J. R. Astr. Soc.*, **96**, 163-177.

Richards (1976). Dynamic motions near an earthquake fault: a three-dimensional solution *Bull. Seismol. Soc. Am.*, **66**, 1-32.

Romanowicz, B. (1992). Strike-slip earthquakes on quasi-vertical transcurrent faults; inferences for general scaling relations, *Geophys. Res. Lett.*, **19**, 481-484.

Sadigh, K., C.Y. Chang, J.A. Egan, F. Makdisi, and R.R. Youngs (1997). Attenuation relationships for shallow crustal earthquakes based on California strong motion data, *Seis. Res. Lett*, **68**, 180-189.

Saikia, C.K. (1993). Estimated ground motions in Los Angeles due to a $M_w = 7$ earthquake on the Elysian thrust fault, *Bull. Seismol. Soc. Am.*, **83**, 780-810.

Saikia, C.K., and P.G. Somerville (1997). Simulated hard-rock motions in Saint Louis, Missouri, from large New Madrid earthquakes ($M_w \geq 6.5$), *Bull. Seismol. Soc. Am.*, **87**, 123-139.

Sammis, C. G., R.M. Nadeau, and L.R. Johnson (1999). How strong is an asperity?, *J. Geophys. Res.*, **104**, 10,609-10,619.

Scholz, C.H. (1982). Scaling laws for large earthquakes; consequences for physical models, *Bull. Seismol. Soc. Am.*, **72**, 1-14.

Scholz, C.H. (1990). The Mechanics of Earthquakes and Faulting, *Cambridge University Press*, New York.

Scholz, C.H. (1994). A reappraisal of large earthquake scaling, *Bull. Seismol. Soc. Am.*, **84**, 215-218.

Sekiguchi, H., K. Irikura, T. Iwata, Y. Kakehi, and M. Hoshiba (1996). Determination of the location of faulting beneath Kobe during the 1995 Hyogo-ken Nanbu, Japan, earthquake from near-source particle motion, *Geophys. Res. Lett.*, **23**, 387-390.

Sekiguchi, H., K. Irikura, and T. Iwata (2000). Fault geometry at the rupture termination of the 1995 Hyogo-ken Nanbu earthquake, *Bull. Seismol. Soc. Am.*, **90**, 117-133.

Shaw, B.E., and C.H. Scholz (1996). Slip-length scaling in large earthquakes: Observations and theory and implications for earthquake physics, *Geophys. Res. Lett.*, **28**, 2,6233-2,636.

Somerville, P.G., N.F. Smith, R.W. Graves, and N.A. Abrahmson (1997). Modification of empirical strong ground motion attenuation relations to include the amplitude and duration effects of rupture directivity, *Seis. Res. Lett.*, **68**, 199-222.

Somerville, P.G., K. Irikura, R.W. Graves, S. Sawada, D.J. Wald, N.A. Abrahmson, Y. Iwasaki, T. Kagawa, N.F. Smith, and A. Kowada (1999). Characterizing crustal earthquake slip models for the prediction of strong ground motion, *Seis. Res. Lett.*, **70**, 59-80.

Spudich, P., and N. Frazer (1984). Use of ray theory to calculate high-frequency radiation

from earthquake sources having spatially variable rupture velocity and stress drop, *Bull. Seismol. Soc. Am.*, **74**, 2,061-2,082.

Spudich, P., and R.J. Archuleta (1987). Techniques for earthquake ground-motion calculation with applications to source parameterization of finite faults *some book edited by B.A. Bolt*, 205-265.

Spudich, P. (1992). On the inference of absolute stress levels from seismic radiation, *Tectonophysics*, **211**, 99-106.

Spudich, P., J.B. Fletcher, M. Hellweg, J. Boatwright, C. Sullivan, W.B. Joyner, T.C. Hanks, D.M. Boore, A.F. McGarr, L.M. Baker, and A.G. Lindh, (1997). SEA96; new predictive relation for earthquake ground motions in extensional tectonic regimes, *Seis. Res. Lett.*, **68**, 190-198.

Spudich, P., M. Guatteri, K.Otsuki, and J. Minagawa (1998). Use of fault striations and dislocation models to infer tectonic shear stress during the 1995 Hyogo-ken Nanbu (Kobe) earthquake, *Bull. Seismol. Soc. Am.*, **88**, 413-427.

Spudich, P., W.B. Joyner, A.G. Lindh, D.M. Boore, B.M Margaris, and J.B. Fletcher (1999). SEA99; a revised ground motion prediction relation for use in extensional tectonic regimes, *Bull. Seismol. Soc. Am.*, **89**, 1,156-1,170.

Spudich, P., and L. Xu (2002). Software for Calculating Earthquake Ground Motions from Finite Faults in Vertically Varying Media, *in International Handbook of Earthquake & Engineering Seismology*, Volume 2, W.H.K. Lee, H. Kanamori, P. Jennings, and C. Kisslinger (eds.), Academic Press ,Orlando, *in press*.

Steidl, J.H., and R.J. Archuleta (1991). Rupture history of the 1989 Loma Prieta, California, earthquake, *Bull. Seismol. Soc. Am.*, **81**, 1,573-1,602.

Su, Y., J.G. Anderson, and Y. Zeng (1996). Comparison of strong and weak motion site amplifications from Northridge earthquake sequence, *EOS, Transaction, Am. Geophys. Union*, **77**, 494.

Thatcher, W., G. Marshall, and M. Lisowski (1997). Resolution of fault slip along the 470-km-long rupture of the great 1906 San Francisco earthquake and its implications, *J. Geophys. Res.*, **102**, 5,353-5,367.

Turcotte, D.L. (1989). Fractals in Geology and Geophysics, *Pure Appl. Geophys.*, **131**, 171-196.

Voss, R.F. (1988). Fractals in nature: from characterization to simulation, *The Science of Fractal Images*, H.-O. Peitgen and D. Saupe (Editors), *Springer*, 21-70.

Wald, D.J., D.V. Helmberger, and S.H. Hartzell (1990). Rupture process of the 1987 Superstition Hills earthquake from the inversion of strong-motion data, *Bull. Seismol. Soc. Am.*, **80**, 1,079-1,098.

Wald, D.J., D.V. Helmberger, and T.H. Heaton (1991). Rupture model of the 1989 Loma Prieta earthquake from the inversion of strong-motion and broadband teleseismic data, *Bull. Seismol. Soc. Am.*, **81**, 1,540-1,572.

Wald, D.J. (1992). Strong motion and broadband teleseismic analysis of the 1991 Sierra Madre, California, earthquake, *J. Geophys. Res.*, **97**, 11,033-11,046.

Wald, D.J., H. Kanamori, D.V. Helmberger, and T.H. Heaton (1993). Rupture model of the 1989 Loma Prieta earthquake from the inversion of strong-motion and broadband teleseismic data, *Bull. Seismol. Soc. Am.*, **83**, 981-1,019.

Wald, D.J., and T.H. Heaton (1994). Spatial and temporal distribution of slip for the 1992 Landers, California, earthquake, *Bull. Seismol. Soc. Am.*, **84**, 668-691.

Wald, D.J., and P.G. Somerville (1995). Variable-slip rupture model of the great 1923 Kanto, Japan earthquake; geodetic and body-waveform analysis, *Bull. Seismol. Soc. Am.*, **85**, 159-177.

Wald, D.J. (1996a). A dislocation model of the 1995 Kobe, Japan earthquake determined from strong motion, teleseismic, and geodetic data, *J. Phys. Earth*, **44**, 489-503.

Wald, D.J., T.H. Heaton, and K.W. Hudnut (1996b). The slip history of the 1994 Northridge, California, earthquake determined from strong-motion, teleseismic, GPS, and leveling data, *Bull. Seismol. Soc. Am.*, **86**, 49-70.

Wang, J.-H., and S.-S. Ou (1998). On scaling of earthquake faults, *Bull. Seismol. Soc. Am.*, **88**, 758-766.

Warner, M., M. Spaargaren, R. Jones, D. Watts, and J. Doody (1994). High-resolution images of the lower crust; deep seismic reflections from 15 to 180 Hz, *Tectonophysics*, **232**, 225-237.

Wells, D.L., and K.J. Coppersmith (1994). New empirical relationships among magnitude, rupture length, rupture width, rupture area, and surface displacement, *Bull. Seismol. Soc. Am.*, **84**, 974-1,002.

Wiemer, S., and K. Katsumata, Spatial variability of seismic parameters in aftershock zones, *J. Geophys. Res.*, *104*, 13,135-13,152, 1999.

Working Group on California Earthquake Probabilities (2000). Earthquake Probabilities in the San Francisco Bay Region: 2000 to 2030 - A summary of findings, *USGS Open File Report*, 99-517.

Wyss, M. (1979). Estimating maximum expectable magnitude of earthquakes from fault
dimensions, *Geology*, **7**, 336-340.

Yoshida, S., K. Koketsu, T. Kato, B. Shibazaki, T. Sagiya, and Y. Yoshida (1996). Joint
inversion of near- and far-field waveforms and geodetic data for the rupture process of
the 1995 Kobe earthquake, *J. Phys. Earth*, **44**, 437-454.

Youngs, R.R., N. Abrahamson, F. Makdisi, and K. Sadigh (1995). Magnitude-dependent
variance of peak ground acceleration, *Bull. Seismol. Soc. Am.*, **85**, 1,161-1,176.

Zeng, Y., J.G. Anderson, and Y. Guang (1994). A composite source model for computing
realistic synthetic strong ground motions, *Geophys. Res. Lett.*, **21**, 725-728.

Zeng, Y., and J.G. Anderson (2000). Earthquake source and near-field directivity modeling
of several large earthquakes, *EERI 6th International Conference on Seismic Zonation*,
Palm Springs.